NASA Contractor Report 204154

# Effects of Neutral Density on Energetic Ions Produced Near High-Current Hollow Cathodes

Ikuya Kameyama
*Colorado State University*
*Fort Collins, Colorado*

October 1997

Prepared for
Lewis Research Center
Under Grant NAG3–1801

National Aeronautics and
Space Administration

# REPORT DOCUMENTATION PAGE

Form Approved
OMB No. 0704-0188



| 1. AGENCY USE ONLY (*Leave blank*) | 2. REPORT DATE | 3. REPORT TYPE AND DATES COVERED |
|---|---|---|
| | October 1997 | Final Contractor Report |

**4. TITLE AND SUBTITLE**

Effects of Neutral Density on Energetic Ions Produced Near High-Current Hollow Cathodes

**5. FUNDING NUMBERS**

WU–632–1B–1B–00
G–NAG3–1801

**6. AUTHOR(S)**

Ikuya Kameyama

**7. PERFORMING ORGANIZATION NAME(S) AND ADDRESS(ES)**

Colorado State University
Fort Collins, Colorado 80523

**8. PERFORMING ORGANIZATION REPORT NUMBER**

E–10945

**9. SPONSORING/MONITORING AGENCY NAME(S) AND ADDRESS(ES)**

National Aeronautics and Space Administration
Lewis Research Center
Cleveland, Ohio 44135–3191

**10. SPONSORING/MONITORING AGENCY REPORT NUMBER**

NASA CR–204154

**11. SUPPLEMENTARY NOTES**

Project Manager, Vincent K. Rawlin, Power and On-Board Propulsion Technology Division, NASA Lewis Research Center, organization code 5430, (216) 977–7462.

**12a. DISTRIBUTION/AVAILABILITY STATEMENT**

Unclassified - Unlimited
Subject Category 20

This publication is available from the NASA Center for AeroSpace Information, (301) 621–0390.

**12b. DISTRIBUTION CODE**

**13. ABSTRACT** ***(Maximum 200 words)***

Energy distributions of ion current from high-current, xenon hollow cathodes, which are essential information to understand erosion phenomena observed in high-power ion thrusters, were obtained using an electrostatic energy analyzer (ESA). The effects of ambient pressure and external flow rate introduced immediately downstream of hollow cathode on ion currents with energies greater than that associated with the cathode-to-anode potential difference were investigated. The results were analyzed to determine the changes in the magnitudes of ion currents to the ESA at various energies. Either increasing the ambient pressure or adding external flow induces an increase in the distribution of ion currents with moderate energies ($\varepsilon < 25$ to 35 eV) and a decrease in the distribution for high energies ($\varepsilon > 25$ to 35 eV). The magnitude of the current distribution increase in the moderate energy range is greater for a cathode equipped with a toroidal keeper than for one without a keeper, but the distribution in the high energy range does not seem to be affected by a keeper. An MHD model, which has been proposed to describe energetic-ion production mechanism in hollow cathode at high discharge currents, was developed to describe these effects. The results show, however, that this model involves no mechanism by which a significant increase of ion current could occur at any energy. It was found, on the other hand, that the potential-hill model of energetic ion production, which assumes existence of a local maximum of plasma potential, could explain combined increases in the currents of ions with moderate energies and decreases in high energy ions due to increased neutral atom density using a charge-exchange mechanism. The existing, simplified version of the potential-hill model, however, shows poor quantitative agreement with measured ion-current-energy-distribution changes induced by neutral density changes.

| 14. SUBJECT TERMS | 15. NUMBER OF PAGES |
|---|---|
| Xenon ions; Ion thruster; Hollow cathode | 110 |
| | 16. PRICE CODE A06 |

| 17. SECURITY CLASSIFICATION OF REPORT | 18. SECURITY CLASSIFICATION OF THIS PAGE | 19. SECURITY CLASSIFICATION OF ABSTRACT | 20. LIMITATION OF ABSTRACT |
|---|---|---|---|
| Unclassified | Unclassified | Unclassified | |

## Table of Contents

## List of Tables

## List of Figures

## Nomenclature

| | |
|---|---|
| $A$ | Area |
| $B$ | Magnetic induction |
| $e$ | Electron charge |
| $\dot{h}_t$ | Target erosion rate |
| $J$ | Current |
| $J_{CD}$ | Discharge current |
| $J_e$ | Cathode electron emission current |
| $J_H$ | Heater current |
| $J_i$ | Measured ion current |
| $J_K$ | Keeper current |
| $j$ | Current density |
| $j_i$ | Measured ion current density |
| $k_B$ | Boltzmann constant |
| $m_e$ | Electron mass |
| $m_i$ | Ion mass |
| $m_t$ | Atomic mass of target material |
| $\dot{m}_c$ | Cathode flow rate |
| $\dot{m}_{ext}$ | External flow rate |
| $n$ | Plasma density |
| $n_0$ | Neutral density |
| $n_+$ | Xenon ion density |
| $n_e$ | Electron density |
| $n_{ea}$ | Ambient electron density |
| $n_{em}$, $n_m$ | Maxwellian electron density |
| $n_{ep}$, $n_p$ | Primary electron density |
| $P$ | Local pressure |
| $P_0$ | Ambient pressure |
| $T_e$ | Electron temperature |
| $T_{ea}$ | Ambient electron temperature |
| $V_a$ | Ambient plasma potential* |
| $V_C$ | Cathode-to-ground potential difference |
| $V_{CD}$ | Discharge voltage |
| $V_K$ | Keeper potential* |
| $V_p$ | Peak plasma potential* |
| $V_t$ | Target potential* |
| $v_B$ | Bohm velocity |

| | |
|---|---|
| $v_{ep}$ | Speed of primary electrons at the potential hill crest |
| $v_{iu}$ | Upstream ion escape velocity from the potential hill |
| $v_{id}$ | Downstream ion escape velocity from the potential hill |
| $z$, $z_1$, $z_2$ | Distance from the cathode orifice |
| $z_c$ | Distance to cathode plasma boundary† |
| $z_u$ | Distance to upstream edge of potential hill† |
| $z_d$ | Distance to downstream edge of potential hill† |
| $z_a$ | Distance to ambient plasma boundary† |
| $\delta$ | Function defined on pg. 69 |
| $\varepsilon$ | Ion energy at cathode potential |
| $\varepsilon_p$ | Primary electron energy |
| $\eta_t$ | Sputtering yield of target material |
| $\mu_0$ | Permeability of free space |
| $\rho_t$ | Density of target material |
| $\sigma$ | Total collision cross-section |
| $\sigma_{ce}$ | Charge-exchange cross-section |
| $\sigma_i$ | Ionization cross-section |
| $\underline{\Omega}$ | Solid angle |
| $\underline{\ }$ | Vector quantity |

* Measured with respect to cathode potential
† Measured from orifice plate

# I. Introduction

The mass of any spacecraft can be broken up into two essential portions: the payload mass, which is needed to achieve mission-specific goals, and the propulsion system mass, which is needed to deliver the payload to a designated location. The fraction of an initial spacecraft mass that will be delivered as payload depends on the ratio of the total impulse required for the mission, or $\Delta V$, to the propellant exhaust velocity. In order to maximize this payload mass fraction so that the initial mass of spacecraft is used effectively, high exhaust velocity is essential. This is especially true for planetary expeditions and other deep space missions, which are characterized by very large $\Delta V$ values (of the order of hundreds of km/sec). When conventional chemical rockets, which have propellant exhaust velocities between 2,000 and 4,400 m/sec, are used for missions with a $\Delta V$ of 10 km/sec, the fractions of initial spacecraft mass that can be delivered to the destination will be less than 10%. On the other hand, electric propulsion systems, which accelerate the propellants to very high velocities using electromagnetic or electrostatic body forces, can deliver much larger fractions. For example, an ion propulsion system, which uses electrostatic forces and can readily produce exhaust velocities as great as 100,000 m/sec, can deliver a 90% payload mass fraction on a 10 km/sec mission. This advantage is significant not only for planetary exploration and deep space missions but also for station keeping of near-

earth satellites over long operating periods (years).

There are other significant differences between ion- and conventional-propulsion systems that must be considered. For example, ion-propulsion systems must operate at thrust levels that are low compared to those of conventional chemical rocket systems because the electrical power needed to sustain their operation is not abundant in spacecraft. Operation at higher powers yields greater thrusts and lower total mission times. However, thruster operating times are still very long (of the order of 10,000 hours) even at the most ambitious specific power levels being considered today.

Ion-propulsion-system operation typically involves propellant-ion creation via an impact-ionization process in which energetic electrons strike neutral atoms. Figure 1 shows a schematic diagram of an electrostatic thruster equipped with hollow cathodes as electron sources. Propellant, which is supplied primarily through the propellant feed line, is ionized by electrons produced at a hollow cathode placed on the thruster centerline (the main cathode). In order to provide these electrons, additional propellant is fed into the cathode and the low-work-function insert identified in Fig. 1 is heated to thermionic-electron emission temperatures. The electron current drawn from the insert is then amplified via ionization of the propellant gas within the cathode and extracted through the orifice. The cathode orifice plate serves to facilitate this process by maintaining a relatively high pressure within the cathode. The electrons are extracted through the orifice into the thruster discharge chamber by an electric field established between the cathode and the plasma produced within the chamber. On some occasions, a starter electrode located

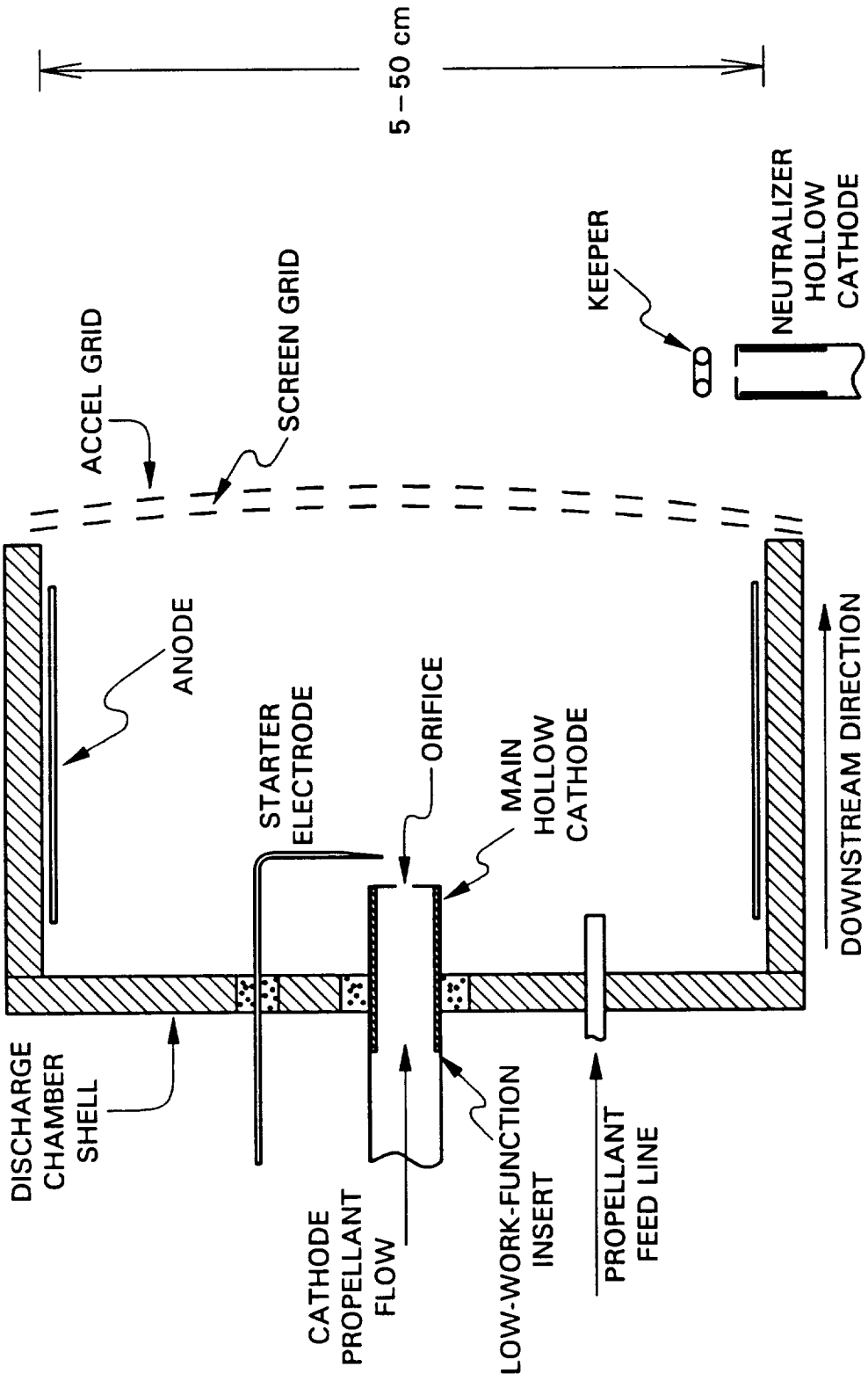


Fig. 1 A Typical Electrostatic Thruster with Hollow Cathodes

downstream of the orifice is used to initiate the discharge within the hollow cathode. Energetic electrons ejected through the cathode orifice collide with neutral atoms fed into the chamber and produce a plasma containing the propellant ions. Ions are then accelerated in an electric field established between apertures of the screen and accelerator (or accel) grids thereby forming an ion beam that is exhausted at high velocity. Another hollow cathode is provided downstream of the thruster grid set to neutralize the ion beam by emitting electrons. The neutralizer hollow cathode shown in Fig. 1 is similar to the one in the thruster chamber except for the fact that it is equipped with a keeper that assures a sustainable electrical discharge from the cathode.

In many ground-based applications the electrons required can be drawn from an inexpensive refractory-metal wire made of a material such as tungsten or tantalum that is heated to a high temperature. Unfortunately, such a wire is subject to life-limiting sputter erosion as a consequence of bombardment by the ions created in the plasma. In addition, the electron current that can be emitted from a wire is limited because ions required to neutralize the electron space charge that otherwise develops between the wire and the ambient plasma are in short supply. A cathode without a high emission-current capability is unsuitable for high-thrust, high-power electric propulsion system operation. On the other hand, a hollow cathode, which involves the production of a plasma in a tube and the extraction of electrons from this plasma, has a demonstrated capability of operating reliably for the required periods of time at the electron currents needed for high power operation.[1]

High-current hollow cathodes are required, for example, in 5-to-10-kW ion

thrusters operating with xenon propellant that can be used for many planetary missions.[2,3,4,5] Wear tests have been conducted at the NASA Lewis Research Center and the Jet Propulsion Laboratory to demonstrate adequate lifetimes associated with high-current hollow-cathode operation in thruster chambers for these missions. In early tests, it was found that severe sputter erosion on various electrodes and structures located near hollow cathodes operating at high emission currents (a few tens of amperes) could limit the lifetime of the ion-propulsion systems.[6,7] It was concluded that the observed erosion occurred because heavy particles such as neutral atoms or ions struck surfaces with high kinetic energies.

In order to identify the source of high-energy, heavy particles which cause the erosion and its behavior at various conditions, the energy distributions of ions emitted from high-current hollow cathodes were investigated. The first work, done by Friedly and Wilbur, revealed high-energy ion "jets" which emanated from high-current hollow cathodes.[8] Their work was accomplished using a retarding potential analyzer (RPA) to sense charged-particle current densities and badges to sense erosion rates downstream of the cathode on its centerline. On the basis of changes in badge erosion rates with axial distance from the cathode they concluded that the "jets" emanate from a point near the cathode orifice. From ion-energy profiles measured using the RPA, they also concluded that increases in discharge current induce greater than linear increases in jet ion current density as well as increases in the spread and mean values of the kinetic energies of these ions. In order to explain these observations, they postulated the existence of a potential hill, located downstream of the cathode orifice, on which ions are created and then accelerated to high velocities

further downstream. It was argued that some electrons emitted from the cathode would have sufficient kinetic energy to excessive ionization of neutral atoms very close to the cathode. The light electrons resulting from this event would be expected to leave the ionization region rapidly but the more massive ions would be expected to leave much more slowly thereby raising the local potential and forming the hill. It was postulated that the hill was located so close to the cathode orifice that it yielded ions that appeared to expand spherically from a point source. The existence of such hills has also been postulated in applications involving metal cathodes in vacuum arc[9] and hollow-cathode-based plasma contactors operating in the electron emission mode.[10]

A second experiment in which the energy distribution profiles for ions originating near a high-current xenon hollow cathode were measured was conducted by Latham et al.[11] These measurements were also made using an RPA to obtain the ion energy distribution and the ion "jets" with energies greater than the potential differences between electrodes were again observed. They also analyzed erosion-rate measurements obtained by other researchers as a function of discharge current and they suggested that a magnetohydrodynamic (MHD) effect could be causing the observed acceleration of ions to energies greater than the applied potential differences.

The next measurement of ion-energy distributions near high-current hollow cathodes was conducted by Kameyama and Wilbur using an electrostatic energy analyzer (ESA).[12] In this study, more detailed energy distributions of ions were obtained and the effect of operating with and without a keeper was examined. Results suggested that the number of ions coming from cathodes along their centerlines

increased when a keeper was used, but no quantitative justification for this behavior was found.

The first experiments designed to determine whether the potential-hill or MHD models was more likely to create high-energy ions was conducted by Kameyama and Wilbur.[13] Their approach, which is described in detail in Appendix A of this dissertation, involved measurement of erosion rate distributions as a function of zenith angle (the angle measured from the cathode centerline toward a direction parallel to the orifice plate plane). These experiments, which employed copper erosion sensors that were exposed to a hollow-cathode discharge plasma, showed no clear evidence of the keeper shadow that should have been visible if the high-energy ions were created at the cathode orifice and expanded spherically. This indicates that the ions are 1) directed primarily along the cathode centerline, 2) produced downstream of the keeper, or 3) produced in a region that is large compared to the keeper size. These experiments also showed that erosion rates were reduced dramatically over the entire range of zenith angles investigated by introducing additional expellant flow into the region immediately downstream of the cathode orifice.

Meanwhile, recent experimental and theoretical work, which has shown that ion thruster systems offer better performance than conventional chemical propulsion systems in many commercial applications, has led to the development of the NASA Solar Electric Propulsion Technology Application Readiness (NSTAR) thruster under the New Millennium program.[14] This program is intended to prove that ion propulsion technology has matured to the point where a state-of-art, variable-power thruster can demonstrate the necessary lifetime. A 2000-hour test was designed to

identify possible problems in the NSTAR system. After the first 867 hours of this initial test, severe erosion on the cathode orifice plate and the cathode heater which protruded downstream of the orifice plate plane were observed.[15] In a subsequent test, the design was improved by installing an enclosed keeper, which encapsulated the cathode everywhere but at an orifice adjacent to the cathode orifice. It was expected that this change would make the neutral density around the cathode higher than it had been in the initial test thereby inducing the beneficial effect of additional flow as described in Ref. 13 and Appendix A. Preliminary results suggest this change has mitigated the NSTAR thruster erosion problem.[16]

In this dissertation, effects of changes in neutral density downstream of high-current xenon hollow cathodes on the energy distributions of ions emitted from the cathodes are presented. These distributions have been correlated with erosion phenomena reported previously[13] and reproduced in Appendix A. Ion-energy distributions were probed using an ESA as ambient neutral density and external flow rate were changed. Theoretical predictions based on simple MHD and potential-hill models, which have been proposed to describe high-energy ion production mechanisms, are presented and the experimental measurements are compared with them.

## II. Proposed Models of High-Energy Ion Production

### 1. MHD Model

Maxwell's equations predict that a direct electric current produces steady magnetic field lines-of-force like those shown in Fig. 2a. When the source current associated with this magnetic field has a finite size, interaction between the magnetic field and the current induces a Lorentz force field that causes the current to be pinched inward. The force per unit volume due to this magnetohyrodynamic (MHD) effect can be expressed as a vector product of the current density, $\vec{j}$, and the self-induced magnetic induction, $\vec{B}$; namely $\vec{j} \times \vec{B}$. Since the magnetic induction is proportional to the magnitude of the current density, the effect is proportional to the square of the current density. When this effect is integrated over the volume of the entire channel through which the electric current flows, the total force becomes proportional to the square of total current and to the reciprocal of the cross-sectional area of the channel.

In a cathode orifice, where a substantial current passes through a small channel ($\lesssim$1 mm diameter), this pinching effect can compress the current significantly (Fig. 2b). In this case, the net current flow is from downstream to upstream, which is opposite to the direction of electron flow, and this yields a counter-clockwise magnetic field as viewed from upstream. Following Ecker,[17] the kinetic energy gain

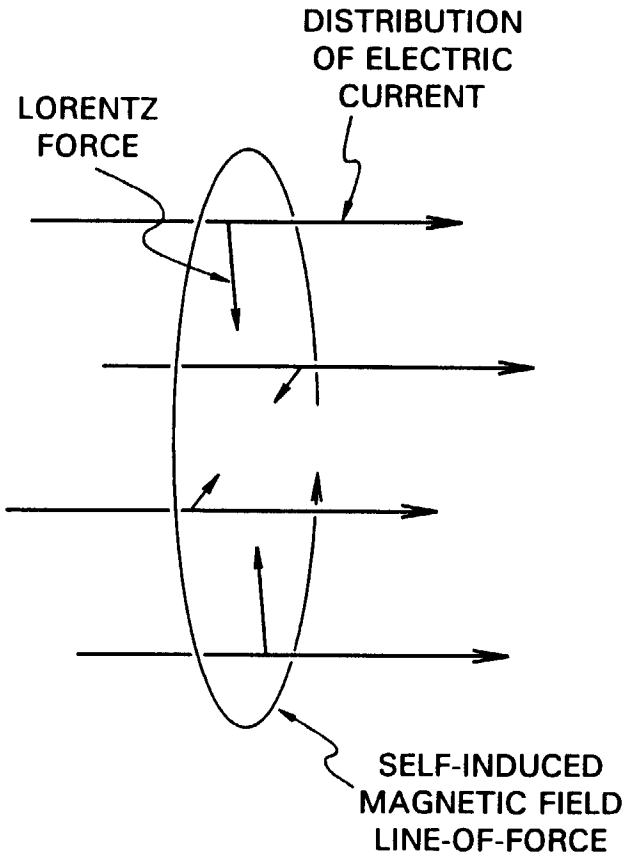


a. In General

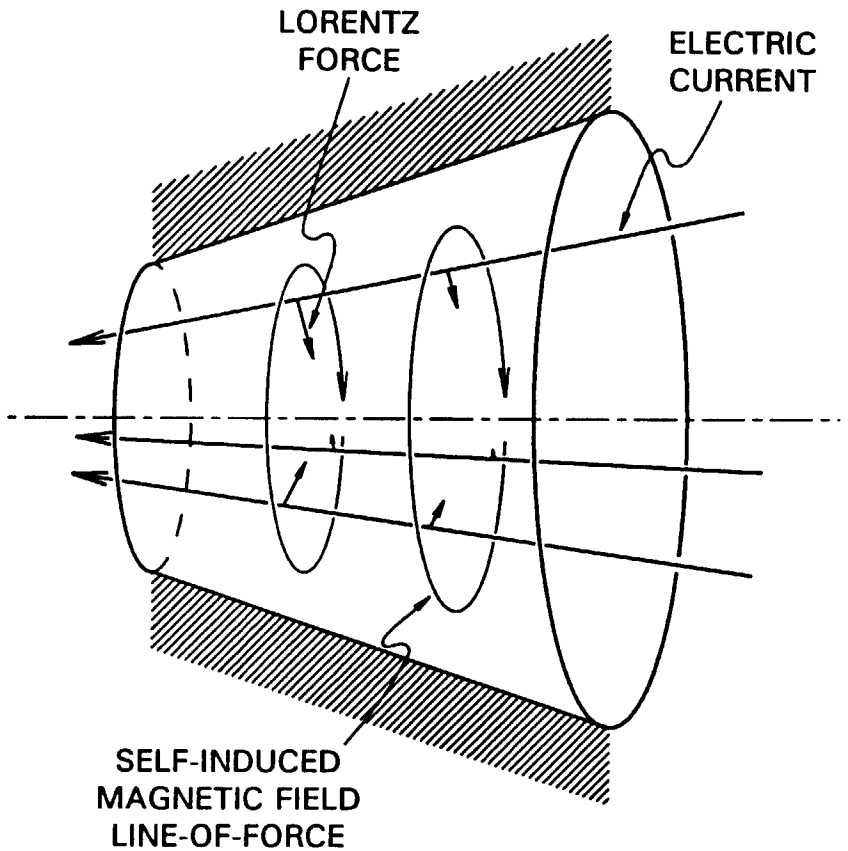


b. In a Chamfered Hollow-Cathode Orifice

Fig. 2 The MHD Effect

of each ion in the plasma can be evaluated as

$$\Delta \varepsilon \sim \frac{\mu_0 J^2}{4 \pi n A} \tag{1}$$

where $\mu_0$ is the permeability of free space, $J$ is the total current, $n$ is plasma density, and $A$ is the area through which the current flows, respectively. For a 20 A current through a 0.81-mm-diameter orifice containing a plasma with a density of $10^{15}$ cm$^{-3}$, this energy gain is computed to be 0.48 eV. This appears to be quite small compared with the energies of ions measured in previous experiments.

Since the total pinching force is proportional to the reciprocal of the area through which the current flows and this area expands rapidly immediately downstream of the orifice, the effect should be significant only near the orifice and dominant within it where this area is least. As Fig. 3 shows, the MHD model involves an abrupt plasma potential increase immediately downstream of the cathode orifice to an ambient plasma value that should be near anode potential. Hence, once the ions have passed through the orifice they experience only deceleration in an adverse electric field and collisions in the ambient plasma.

## 2. Potential-Hill Model

When the electrons are extracted into a region of high neutral density, a potential hill can develop as a consequence of extensive electron-impact ionization. When the process first starts, the potential field is expected to look like the one in Fig. 3b. In this situation, electrons created inside the cathode are drawn out through the orifice and gain kinetic energies that are sufficient to ionize neutral atoms outside

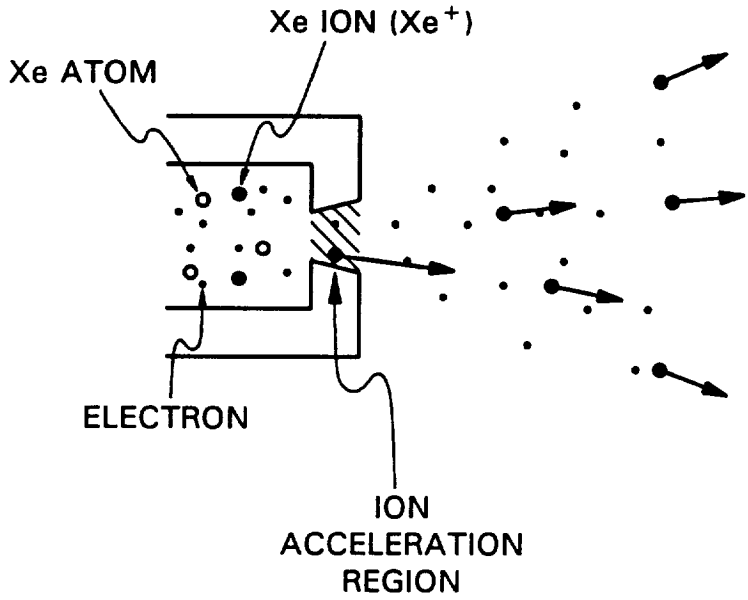


a. Ion Flow

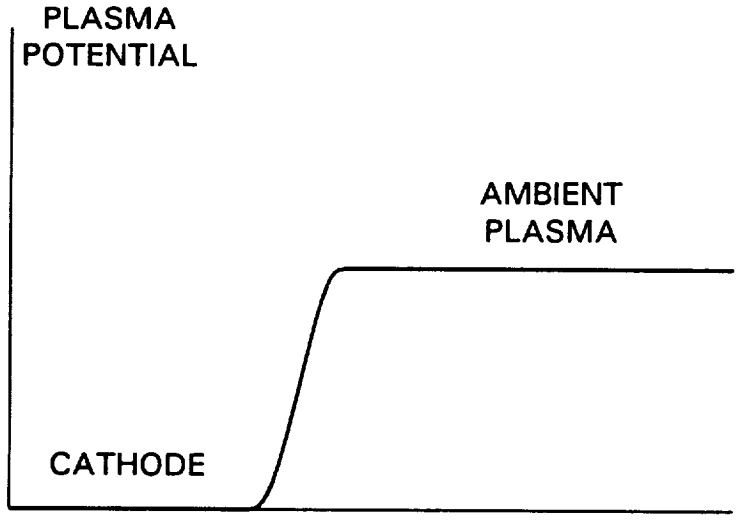


b. Plasma Potential Profile

Fig. 3 Environment near the Cathode Orifice in the MHD Model

the cathode. After such ionization events, secondary electrons readily thermalize and escape this region because of their low mass. On the other hand, the more massive positive ions traveling at much lower speeds tend to accumulate thereby inducing the electric fields around this region that are associated with a potential hill as seen in Fig. 4. Once the potential hill starts to develop, the growth of the potential-hill height continues until the fields are sufficient to eject ions and/or trap the secondary electrons and a steady state is established. The ions created in this potential hill will gain kinetic energies as they fall through the electric fields that develop both upstream and downstream of the hill crest.

The potential hill has also been proposed to explain high energy ions observed coming from hollow-cathode-based plasma contactors. These are devices used to control spacecraft potential in a space-plasma environment by increasing the conductivity through a locally created, high-density plasma. When a hollow cathode is used to supply electrons to the environment, the neutral flow needed to sustain a cathode discharge produces a high-neutral density region immediately downstream of the orifice through which electrons are extracted. In this application, a hump in the potential profile was measured at low electron emission currents (a few amperes).[10]

### 3. Expected Effects of Neutral Densities downstream of the Cathode Orifice

The effects of neutral densities downstream of a cathode orifice on downstream ion flow will differ for the MHD and potential-hill models and these differences are summarized in Table 1. For the MHD model, in which neutral densities inside the orifice are fixed, the only effect will be a loss of high-energy ions

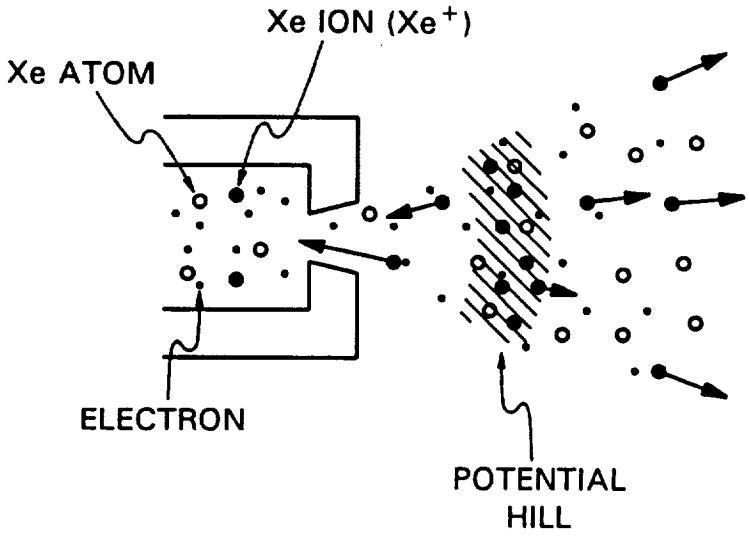


a. Ion Flow

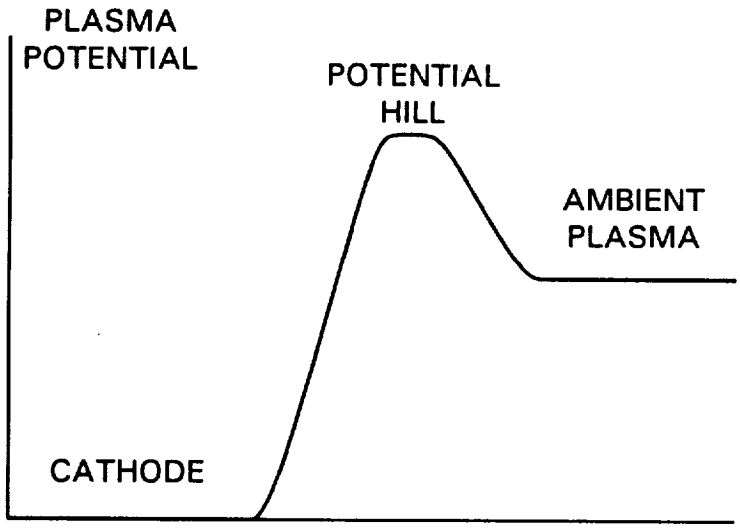


b. Plasma Potential Profile

Fig. 4 Environment near the Cathode Orifice in the Potential-Hill Model

Table 1 Expected Effects of Neutral Densities downstream of the Cathode Orifice

| | Effect on High-Energy-Ion Production | Effect on Non-Ionizing Collisions |
|---|---|---|
| MHD Model | No | Yes |
| Potential-Hill Model | Yes | Yes |

through collisions. For the potential-hill model, on the other hand, neutral atoms introduced downstream of the orifice can affect the flux of high-energy ions in competing ways; first, by scattering the ions thereby reducing the flux and second, by inducing increased ion production thereby increasing the flux. Since the ion scattering losses are part of both models, a simple model to predict this effect will be developed next.

## III. Development of the Scattering Model

The model used to predict the effects of neutral density on the scattering of high-energy ions is illustrated in Fig. 5a. In the model, ions with an energy $\varepsilon$ measured with respect to cathode potential are assumed to be created at a point source located near a cathode orifice. They expand spherically into a downstream ambient plasma that is at a uniform plasma potential, $V_a$, as suggested in the figure. Some of these ions undergo collisions with neutral atoms and are scattered off of initial trajectories that would otherwise carry them to a downstream detector. As the ions enter this ambient plasma, their kinetic energy decreases to $\varepsilon - V_a$ and scattering causes the ion current associated with this energy to decrease from that at a location $z$ to that at another location $z + \Delta z$ by the factor $exp[-\sigma(\varepsilon - V_a)\, n_0\, \Delta z]$ where $\sigma(\varepsilon - V_a)$ and $n_0$ are total collision cross-section and neutral density, respectively. In the kinetic energy range of interest for hollow cathode applications (i.e. tens of eV) only elastic and charge-exchange collisions with neutrals are significant and it is, therefore, assumed that only these events induce significant scattering losses. In this scattering environment, the ion-current energy distributions $dJ_i(\varepsilon)/d\varepsilon$ measured using instruments with the same current-collection area and along the same path but at two different distances from the cathode, $z_1$ and $z_2$, can be related using the equation

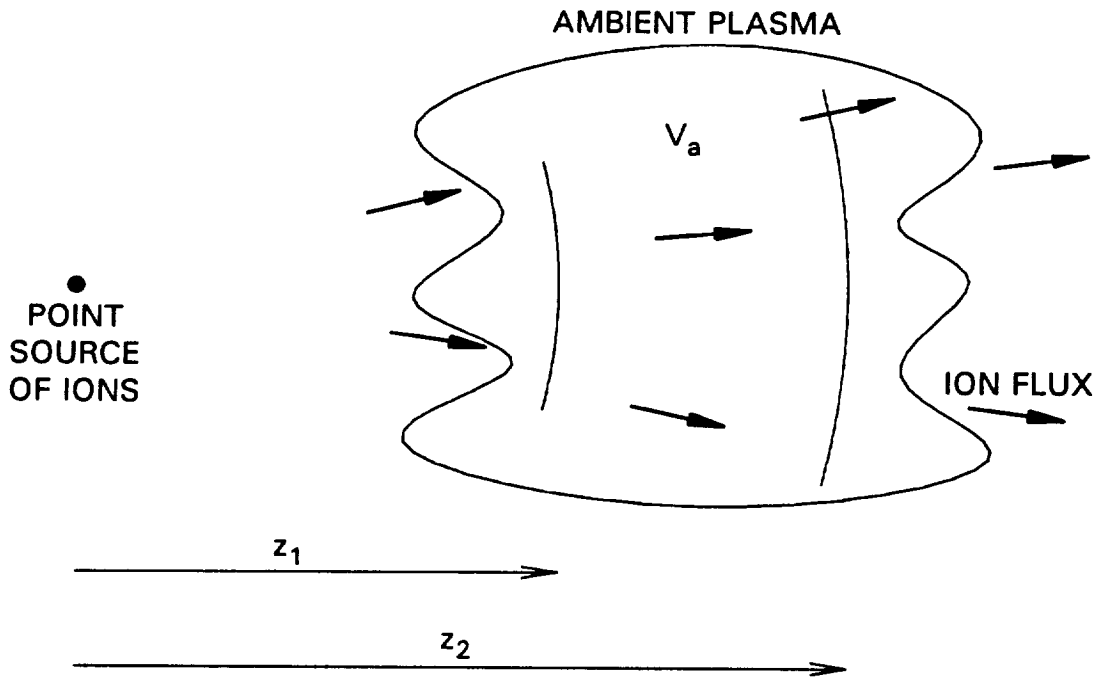


a. Schematic Diagram

$$\left.\frac{dJ_i}{d\varepsilon}(\varepsilon)\right|_{z=z_2} = \left.\frac{dJ_i}{d\varepsilon}(\varepsilon)\right|_{z=z_1}$$

*(Energy Distribution at $z = z_2$)* *(Energy Distribution at $z = z_1$)*

$$\times \frac{z_1^{\,2}}{z_2^{\,2}}$$

*(Geometrical Term)*

$$\times \exp\left[-\int_{z_1}^{z_2} \sigma(\varepsilon - V_a)\, n_0(z)\, dz\right]$$

*(Collisional Loss Term)*

b. Relationship between Distributions Measured at Different Locations

Fig. 5 Scattering Model of Ion Flux Loss due to Collisions downstream of Hollow Cathodes

$$\left.\frac{dJ_i}{d\varepsilon}(\varepsilon)\right|_{z=z_2} = \left.\frac{dJ_i}{d\varepsilon}(\varepsilon)\right|_{z=z_1} \frac{z_1^2}{z_2^2}\, exp\left[-\int_{z_1}^{z_2} \sigma(\varepsilon - V_a)\, n_0(z)\, dz\right]$$

$$= \left.\frac{dJ_i}{d\varepsilon}(\varepsilon)\right|_{z=z_1} \frac{z_1^2}{z_2^2}\, exp\left[-\sigma(\varepsilon - V_a)\int_{z_1}^{z_2} n_0(z)\, dz\right]. \qquad (2)$$

As indicated in Fig. 5b, the second and third terms in the right hand side of the equation are associated with spherical expansion and collisions, respectively.

In this work, Eq. (2) is applied twice to relate ion-current energy distributions at the same location under different neutral density profile conditions assuming that high-energy-ion production rates are independent of the neutral density environment. The resulting ion-current energy distributions $dJ_i'(\varepsilon)/d\varepsilon$ and $dJ_i''(\varepsilon)/d\varepsilon$ both measured at a downstream location $z_2$ for neutral density profiles $n_0'$ and $n_0''$, respectively, can be related to the ion-current energy distribution at a location $z_1$, which is very close to the cathode orifice:

$$\left.\frac{dJ_i'}{d\varepsilon}(\varepsilon)\right|_{z=z_2} = \left.\frac{dJ_i}{d\varepsilon}(\varepsilon)\right|_{z=z_1} \frac{z_1^2}{z_2^2}\, exp\left[-\sigma(\varepsilon - V_a)\int_{z_1}^{z_2} n_0'(z)\, dz\right]$$

$$\left.\frac{dJ_i''}{d\varepsilon}(\varepsilon)\right|_{z=z_2} = \left.\frac{dJ_i}{d\varepsilon}(\varepsilon)\right|_{z=z_1} \frac{z_1^2}{z_2^2}\, exp\left[-\sigma(\varepsilon - V_a)\int_{z_1}^{z_2} n_0''(z)\, dz\right] \qquad (3)$$

When no change is expected in ion production mechanisms, that is, in the ion-current energy distribution at the location $z_1$, these terms along with the geometrical terms cancel out and the ratio of the equations becomes

$$\frac{\left.\frac{dJ_i''}{d\varepsilon}(\varepsilon)\right|_{z=z_2}}{\left.\frac{dJ_i'}{d\varepsilon}(\varepsilon)\right|_{z=z_2}} = exp\left\{-\sigma(\varepsilon - V_a)\int_{z_1 \to 0}^{z_2}\left[n_0''(z) - n_0'(z)\right]dz\right\} . \qquad (4)$$

It should be emphasized that the left-hand side of Eq. (4) is determined from direct ion-current-energy-distribution measurements and the right-hand side is computed using either measured or calculated neutral density profiles. Also, it should be noted that the right-hand side is expressed in terms of the difference in neutral density profiles.

## IV. Experimental Apparatus and Procedures

The physical arrangement of components used in this study is shown in Fig. 6. A hollow cathode was oriented with its axis vertical and an anode was provided so a discharge could be established. The anode-cathode assembly was equipped with either a toroidal keeper like that shown in Fig. 6 or a needle-like starter electrode, which was used to initiate the discharge. This configuration was chosen to simulate typical, hollow-cathode operation within main discharge chambers of ion-propulsion systems. The cathode and plenum were connected as shown in Fig. 6 so their interior pressure could be monitored using a capacitance pressure gauge. The anode was a 1.8-mm-thick copper plate that had been rolled into a 60-mm-inner-diameter-by-115-mm-long hollow cylinder. As shown in Fig. 6, it extended beyond the top end of cathode to about 75 mm downstream and had an approximately 35-mm-wide slit on one side through which the cathode discharge could be observed. This anode was water-cooled during the experiments to assure that it would not melt.

The orificed hollow cathode used in this study was constructed from a 6.4-mm-diameter tantalum tube with a 1.6-mm-thick thoriated-tungsten orifice plate electron-beam-welded on one end as shown in Fig. 7. The orifice had the minimum diameter of 0.81 mm near the upstream end and the maximum diameter of 1.47 mm near the downstream end. The cathode contained an insert (i.e. a low-work-function

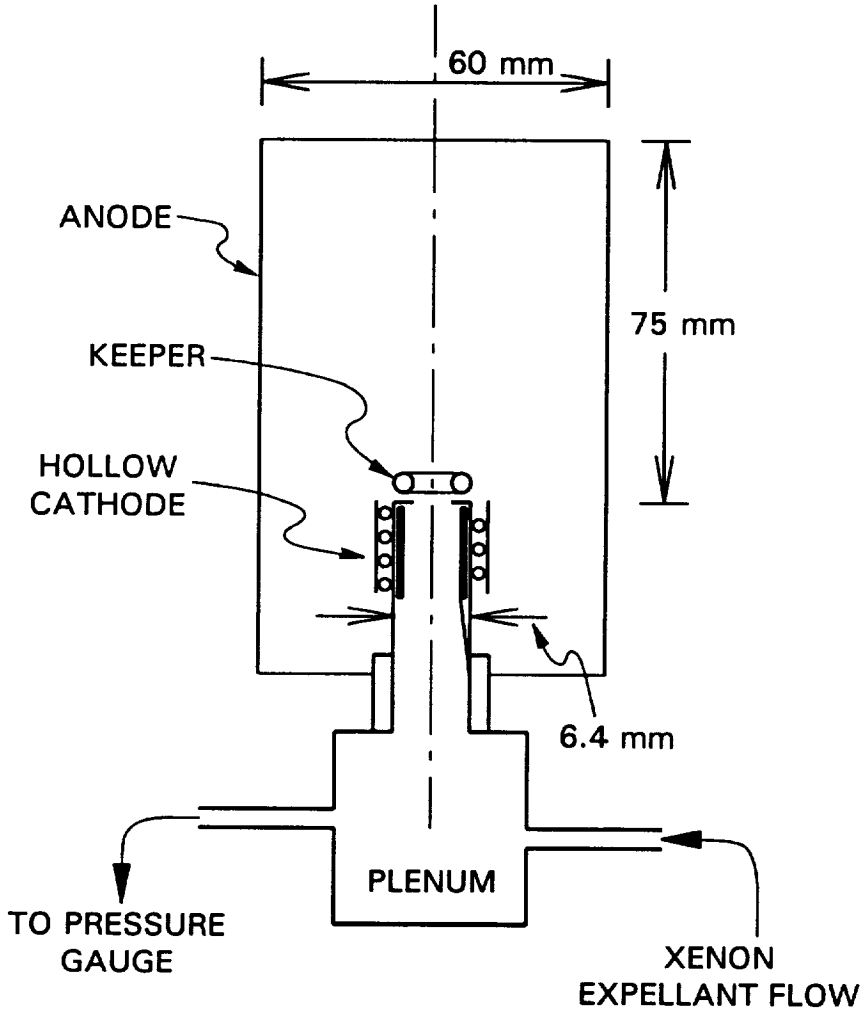


Fig. 6 Schematic Diagram of Hollow-Cathode/Anode Assembly

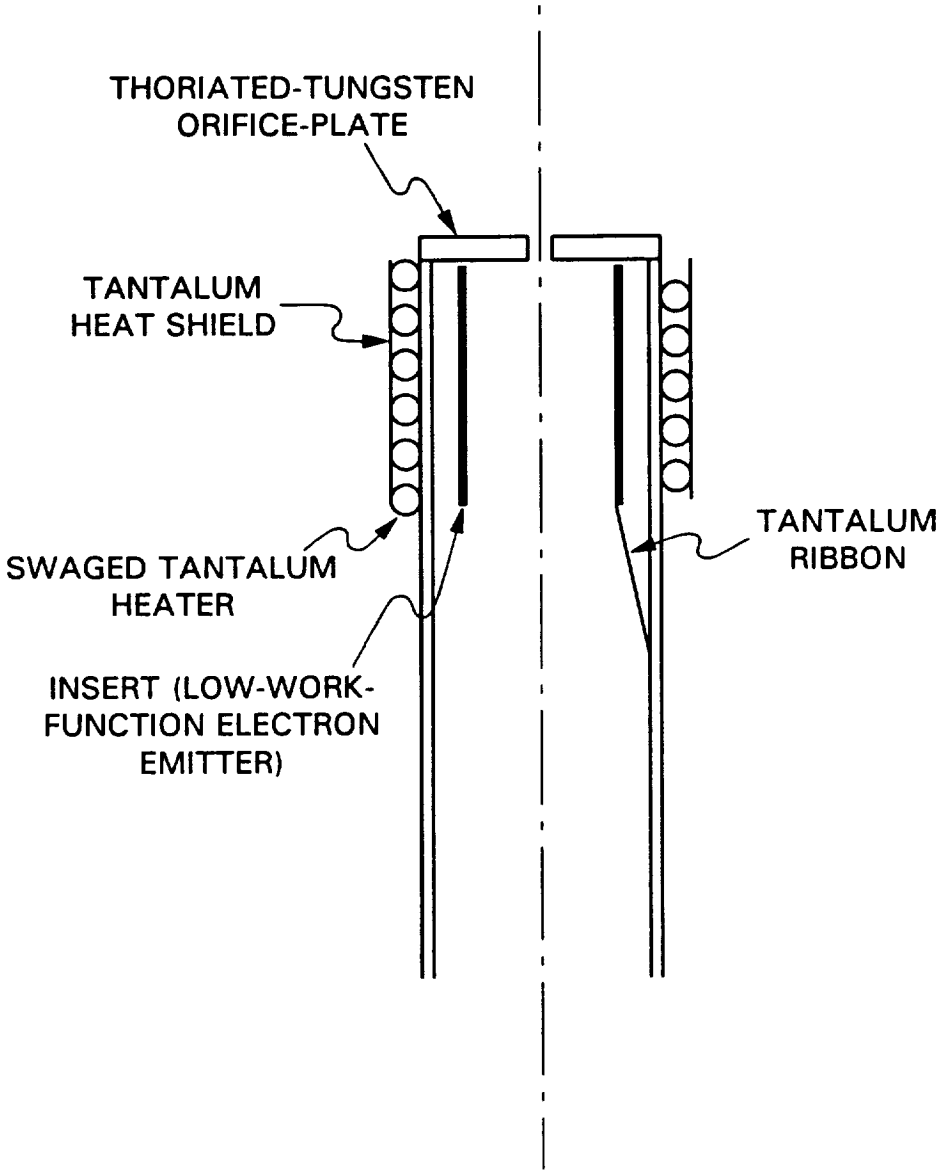


Fig. 7 Schematic Diagram of Hollow Cathode

electron emitter) positioned as shown in Fig. 7. Inserts were made by rolling 75-mm-long, 20-mm-wide, 0.013-mm-thick tantalum foil around a 4-mm-diameter form and then spot-welding this rolled foil to a 3-mm-wide, 45-mm-long, 0.25-mm-thick tantalum ribbon. The rolled foil was then dipped in a solution containing barium carbonates (Chemical R-500) and inserted into the cathode tube. Finally, the ribbon was spot-welded to the inner surface of the cathode tube to assure electrical contact and hold the insert in place. Sintered tungsten inserts, which are generally used in flight-qualified hollow cathodes, were not investigated because previous research had shown insert type did not affect ion-energy distributions significantly.[18] A swaged tantalum heater 15 mm in length was friction fitted to the cathode tube and 0.013-mm-thick tantalum foil heat shields were also used to reduce the radiation heat loss from it.

The keeper electrode shown in Fig. 6 was constructed from a 1.5-mm-diameter tantalum wire that was bent into a 4.0-mm-inner-diameter toroidal ring and positioned 1.0 mm downstream of the cathode orifice. In some tests, it was replaced by a needle-shaped starter electrode in order to investigate the effect of the keeper. The starter was a 0.79-mm-diameter tantalum wire that had been sharpened at one end. It was placed normal to the cathode axis with the sharpened tip positioned 1.0 mm downstream from the downstream orifice perimeter.

Some tests involved xenon flows injected from an external source toward the orifice through flow tubes arranged as shown in Fig. 8. This flow was supplied through the flow tubes rather than via increased xenon flow through the orifice so that the xenon atom density near but outside of the orifice would be changed but plasma

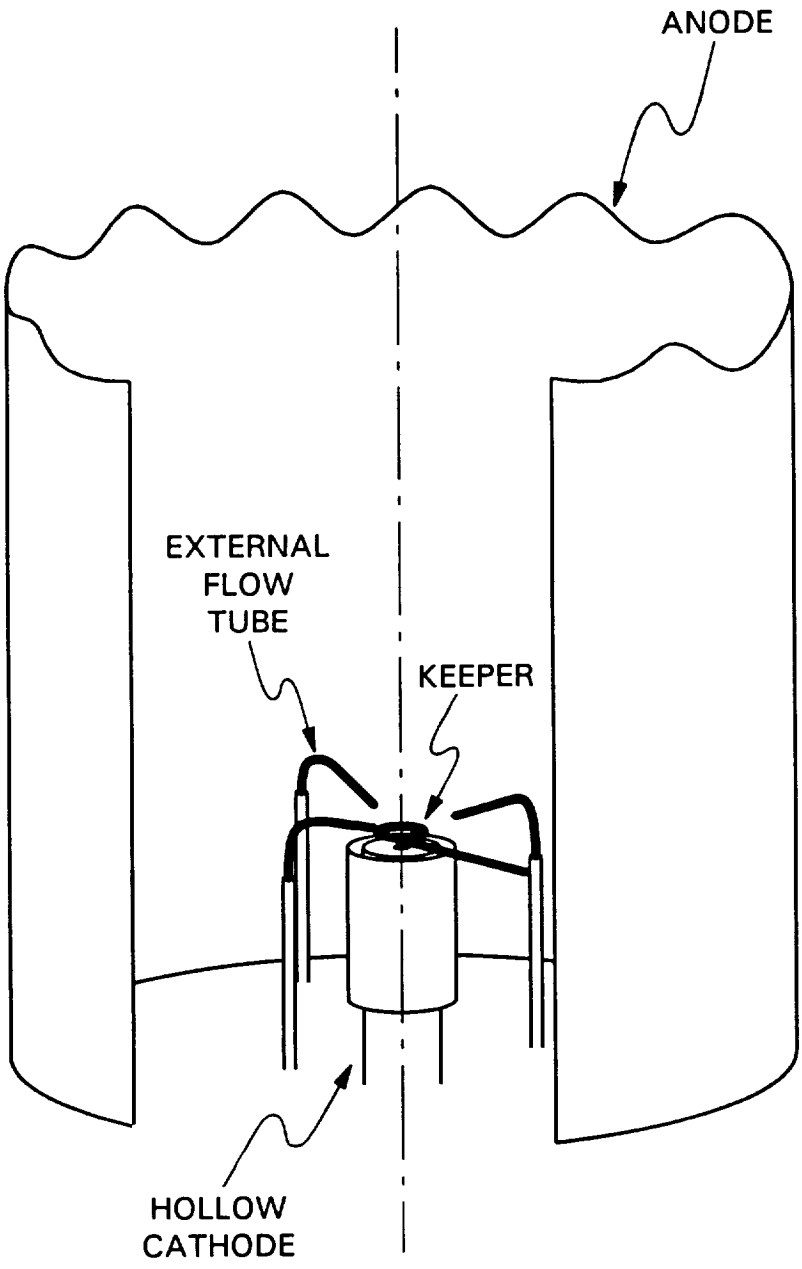


Fig. 8 Setup for External-Expellant-Flow Experiments

properties and neutral densities inside the cathode and cathode orifice would not. The external flow, controlled separately from the cathode orifice flow, was introduced ~5 mm downstream of the orifice through three, nickel capillary tubes with 0.51 and 0.81 mm inner and outer diameters, respectively. The nickel tubes were isolated from adjacent equipment using ceramic tubes so they would float electrically during the tests and their influence on plasma properties in the region would be minimized.

A schematic diagram of the entire vacuum facility used in the experiments is shown in Fig. 9. The hollow-cathode/anode assembly was placed in a 45-cm-diameter-by-70-cm-high cylindrical vacuum chamber connected to a mechanical pump and a cryopump. The mechanical pump was used to evacuate the main chamber to around 80 mTorr (10 Pa) or lower and, also, to regenerate the cryopump through the main chamber periodically (i.e. to remove condensed gases from the cryopump). During actual testing, only the cryopump was used to maintain chamber pressure in the $10^{-4}$ Torr ($10^{-2}$ Pa) range as measured by an ionization gauge connected to the side of the cylindrical vacuum chamber. The minimum ambient pressure achieved at zero xenon flow was of the order of $10^{-7}$ Torr ($10^{-5}$ Pa). In some experiments, the ambient pressure of the chamber, $P_0$, was raised by throttling the flow through a gate valve located between the chamber and the cryopump. Also this was done to hold ambient pressure constant as the external expellant flow through the capillary tubes was varied.

Neutral density profiles were measured along the cathode centerline at various ambient pressure and external flow conditions using an ionization gauge, which had been modified by partially removing its glass casing to expose its active elements to

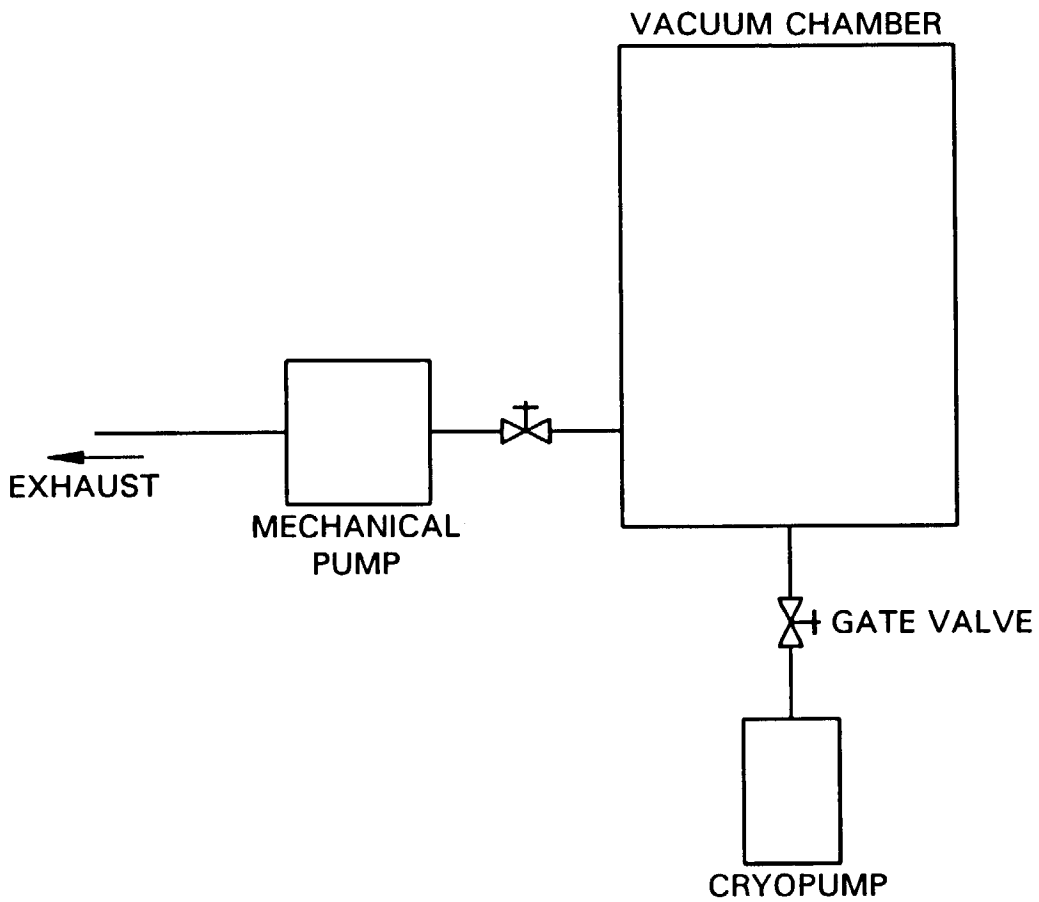


Fig. 9 Schematic Diagram of Vacuum Facility

the environment. After calibration in a room-temperature, xenon atmosphere using a McLeod (high-vacuum, mercury) manometer and applying the ideal gas law with a temperature of 300 K, the gauge was installed in the vacuum chamber on a fixture that was used to move it axially along the cathode centerline. Measurements were made under no-electrical-discharge conditions so that the discharge plasma would not affect the readings.

The power supplies used to sustain steady-state cathode operation for most tests are shown schematically in Fig. 10. The 60-Hz, 10-A AC heater power supply was used to raise the cathode temperature prior to start-up. The keeper supply was used to apply 160 V at a low current level for start-up and to sustain the low-voltage, high-current ($\sim < 2$ A) keeper discharge during normal operation. Meters installed on this supply were used to measure the keeper current, $J_K$, and potential, $V_K$. A 2-kV, 10-mA high-voltage power supply (not shown in Fig. 10) was used to apply a voltage to a starter electrode that was used to initiate cathode operation when the keeper was removed. Once the discharge started, this power supply was disconnected and the electrode was allowed to float. An anode power supply capable of operation at 60 V and 30 A was used to apply the anode potential, $V_{CD}$, required to sustain a prescribed discharge current, $J_{CD}$.

The electrostatic energy analyzer (ESA)[19] used to measure energy distributions of ions produced in hollow-cathode discharges for these and previous tests[20] is shown schematically in Fig. 11. The unit (Comstock Inc., Model AC-901) operates by establishing a radial, electrostatic field between two copper surfaces which form segments of spheres having a common center and different radii. The ESA was

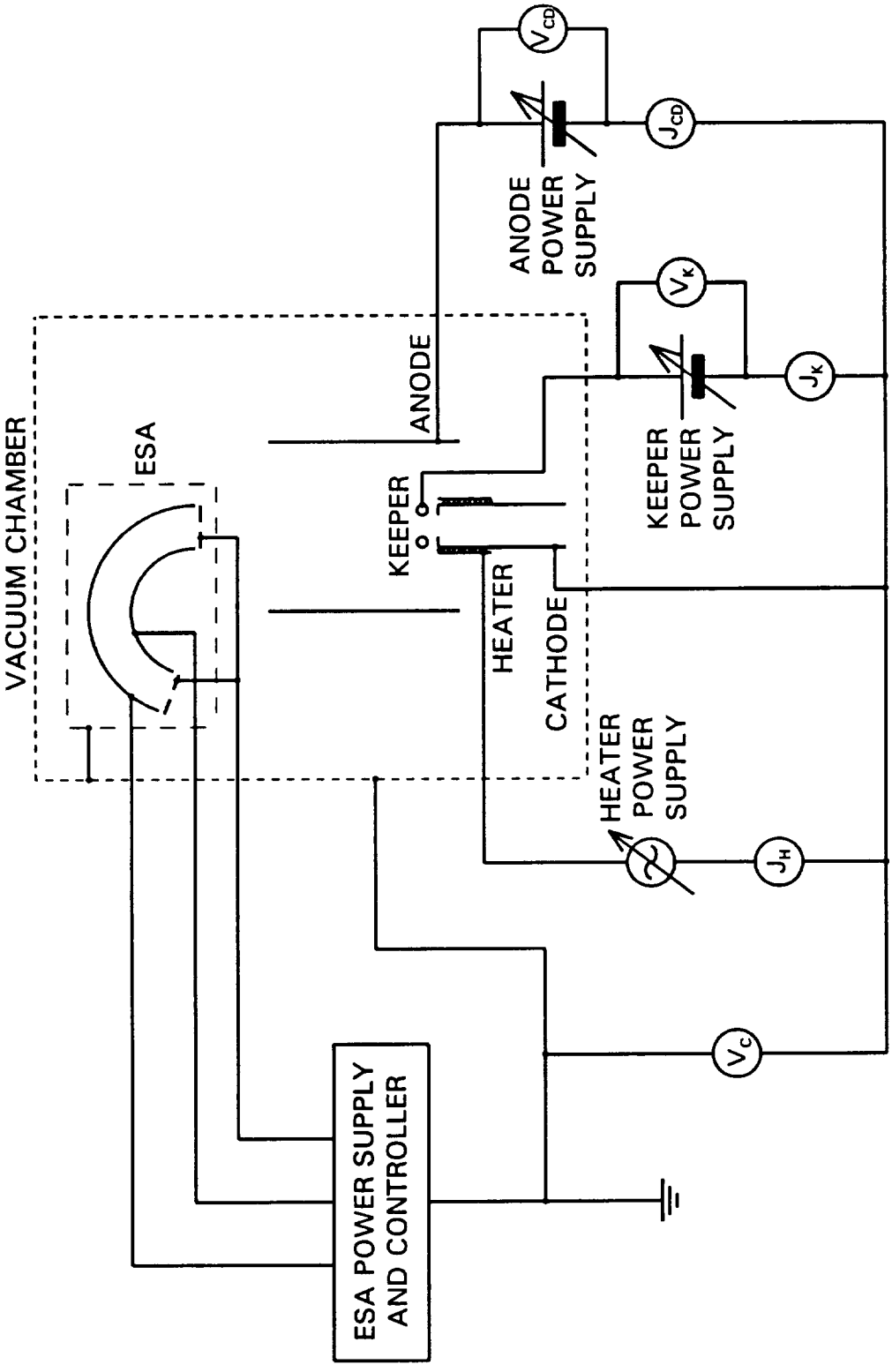


Fig. 10 Schematic Diagram of Power Supplies

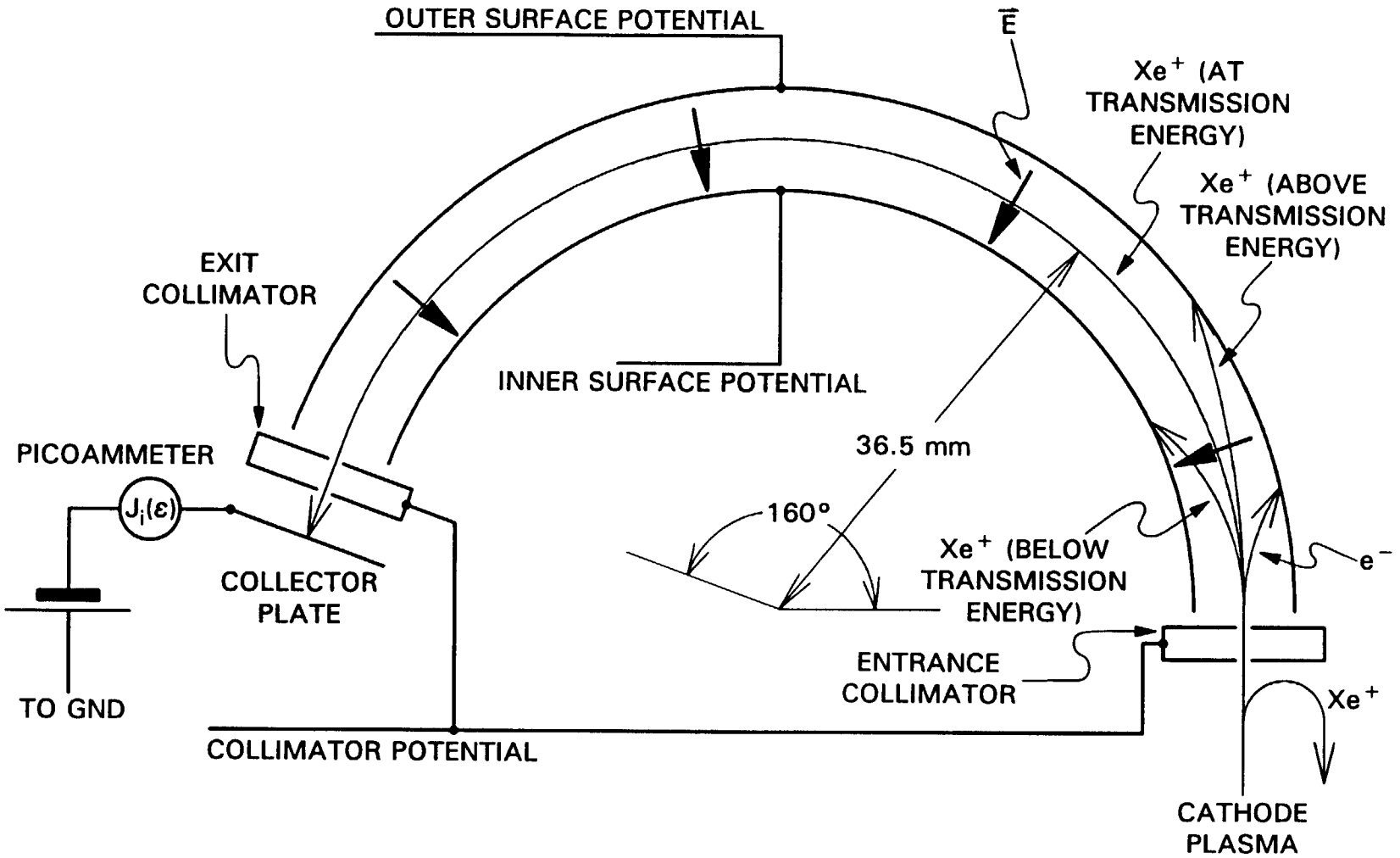


Fig. 11 Schematic Diagram of Electrostatic Energy Analyzer (ESA)

equipped with entrance- and exit-collimator sets that had 2.0-mm-diameter apertures spaced 7.8 mm apart. Charged particles that pass through the entrance collimator are focused along different paths depending upon their kinetic energy, charge and mass. A plain stainless-steel plate was placed just beyond the exit collimator to detect ion current without amplification. A power supply and control unit provided by Comstock Inc. were used to control ESA-surface potentials. The electrostatic fields within the unit were held fixed during use by maintaining constant potential differences between the inner and outer surfaces and the collimator sets. Under this condition, only those ions with a prescribed kinetic energy (the transmission energy) at the entrance collimator were able to pass through the unit to the collector plate and be detected. As suggested in Fig. 11, ions with greater and lesser energies would strike the outer and inner surfaces, respectively. In order to sense the ion-current energy distribution, potentials on the inner, outer, and collimator surfaces were swept together with respect to facility ground potential thereby changing the amount of acceleration or deceleration experienced by ions as they approached the entrance collimator from the cathode-plasma plume.

All interior surfaces that could see ions and/or electrons were coated with graphite to prevent secondary-electron emission, sputtering damage, and/or oxidation during atmospheric exposure. The influence of this coating on the measurements associated with these experiments is described in Appendix B. The entrance collimator was covered by a mask to limit possible contamination of the graphite coating when measurements were not being made. An electromesh nickel screen with an 85%-optical-transparency open area and square openings (0.24 mm on a side) was

placed on the upstream side of a 6.4-mm-diameter entrance aperture on a grounded aluminum box that enclosed the entire ESA. It provided a potential barrier, which limited electron flow into the device and, therefore, the resultant collection of stray currents on electrical connection points and active surfaces. A ferromagnetic material with a 1.8-mm thickness, which provided shielding against geomagnetic-field effects, also enclosed the ESA.

The ESA was positioned 180 mm downstream of the cathode orifice with its entrance-collimator axis aligned with the cathode axis (i.e. looking at the cathode orifice) for all of the experiments described herein. This configuration was used because it was anticipated that the energetic ions would be created near the orifice.

In order to prevent transient discharges between the cathode plasma and facility ground, the hollow-cathode/anode assembly was floated as shown in Fig. 10. The cathode-to-ground potential difference, $V_C$, was found to be almost constant during each test and was typically $0 \sim 5$ V. The stainless steel detector plate placed downstream of the exit collimator was biased about 30 V negative with respect to ground potential using batteries to eliminate any ion dispersion that could have been induced by space-charge effects. Ion currents were sensed by a picoammeter that retransmitted this signal along with the collimator potential measured with respect to cathode potential to an X-Y recorder.

All the experiments were initiated by evacuating the vacuum chamber below $1.5 \times 10^{-6}$ Torr ($2.0 \times 10^{-4}$ Pa) using the cryopump. When the neutral density profiles were obtained, the xenon flow rates through orifice and capillary tubes ($\dot{m}_c$ and $\dot{m}_{ext}$, respectively) were set and the gate valve was adjusted to establish the

desired ambient pressure. The flow was stabilized for 30 minutes before any data were recorded.

Before ion-energy distributions were measured, the cathode was heated using a heater current, $J_H$, of 5 A for 15 minutes while xenon was being bled through the cathode at about 0.3−0.5 sccm [standard cubic centimeters per minute (at 25°C)] Xe (20−35 mA eq. Xe) to flush out possible contaminants. After an additional 15 minutes of heating at a heater current of 8 A with zero xenon flow, the keeper was biased to 160 V with respect to the cathode and the xenon flow rate was increased slowly until a discharge was initiated between the cathode and keeper. This generally occurred at 1−2 sccm Xe (70−130 mA eq. Xe). After the keeper discharge had stabilized at 0.5 A and ~20 V, anode power was applied. In the experiments where a starter electrode was used instead of the keeper, the cathode was heated using the same procedure. Then, the xenon flow through cathode was set at 1.1 sccm Xe (75 mA eq. Xe), the anode was biased 40 V positive of the cathode, and the high-voltage pulse required to initiate a discharge current of 1 A (typically 500~1000 V) was applied to the starter. In this case the discharge was stabilized using the anode power supply only.

Once the discharge was established, operating parameters such as the cathode and external flow rates, keeper current, and discharge current were set. The discharge conditions were allowed to stabilize for at least 30 minutes while the plenum interior pressure was being monitored continuously before ion-current data sensed by the ESA were collected.

The ion currents were measured using a 10-eV ESA transmission energy

established by internal bias conditions and the absolute bias on the instrument was varied over the range that yielded ion energies from a few to 100 eV. Due to the high input impedance of the picoammeter, even a small capacitance connected between the system components could cause remarkably long time-constants in the data-acquisition system. In fact, the data obtained by the system were affected by the speed at which the ESA bias potentials were swept. In order to mitigate this problem, the data were collected at a low rate where the sweeping-speed effect was minimal. In addition, the power supply unit used to set potentials on the ESA surfaces was computer-controlled to assure a steady voltage-sweep speed. The slow sweep speed also promoted noise reduction on lines which usually transmitted noises with high-frequency components.

# V. Experimental Results

## 1. Neutral Density Profiles

In order to examine the effects of various ambient pressures and external flow rates and to incorporate the predictions derived from the models, the neutral density profiles were measured first using the movable, nude ionization gauge described in the previous chapter. Density outputs from the nude gauge, $n_0$, were obtained at three different ambient pressures, the highest of which were held constant as the external flow was varied from zero in two steps by throttling the flow to the cryopump. The measurements were repeated several times both with and without a keeper to obtain mean, axial density profiles. Errors observed in the repeated measurements and the precision associated with the mean profiles are discussed in Appendix B.

Figure 12 shows the effects of ambient pressure and external flow rate on the mean neutral density profiles measured when the cathode was equipped with a keeper. These data show that increasing the ambient pressure with no external flow yields a uniform increase in the density profile (Fig. 12a). On the other hand, introducing external flow while holding ambient pressure fixed causes a less obvious increase in the density (Fig. 12b).

When the keeper was removed, the mean density profiles shown in Fig. 13

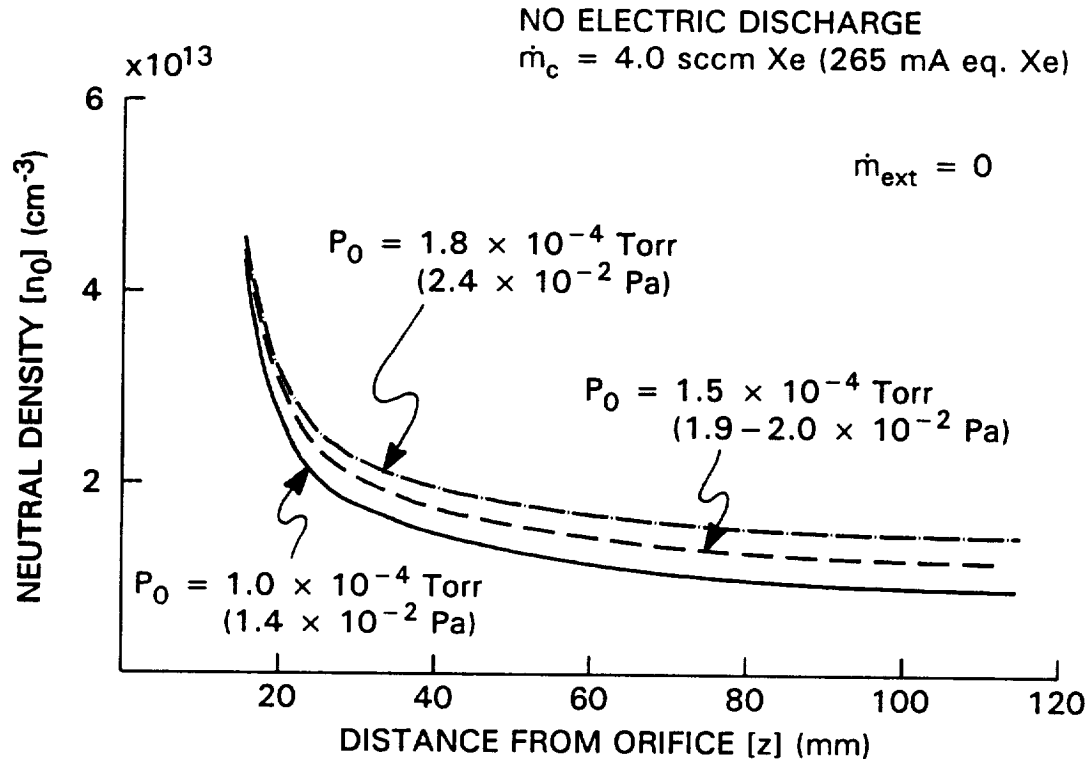


a. Effect of Ambient Pressure

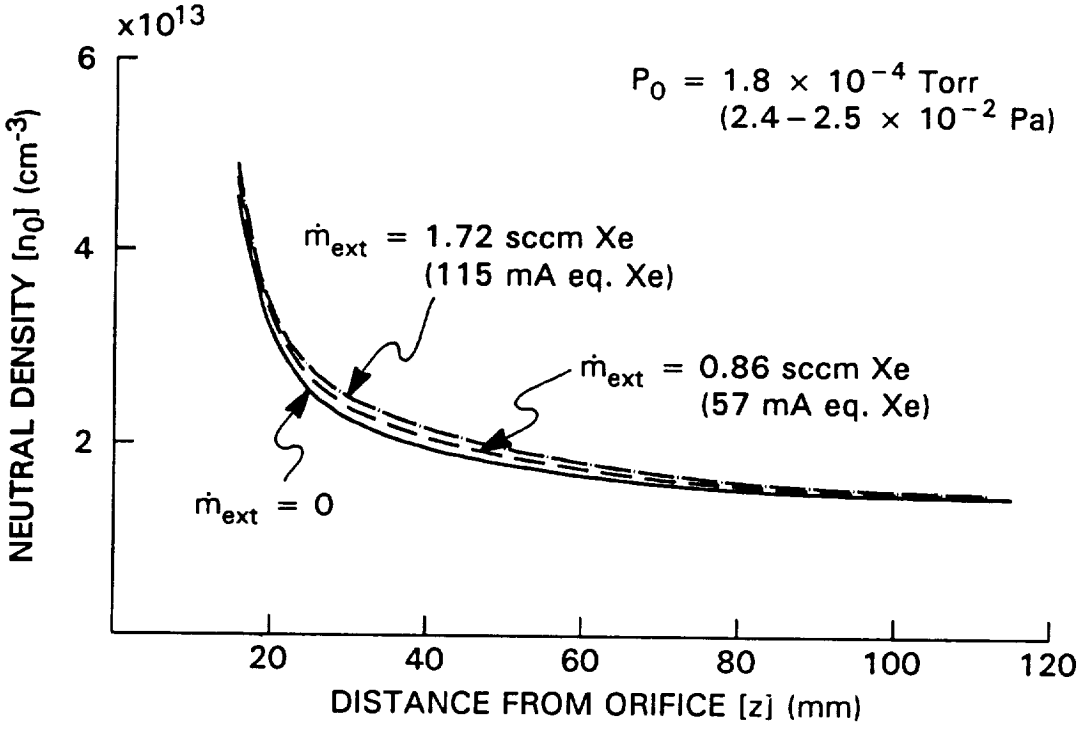


b. Effect of External Flow Rate

Fig. 12 Neutral Density Profiles Measured on the Centerline of the Cathode with Keeper

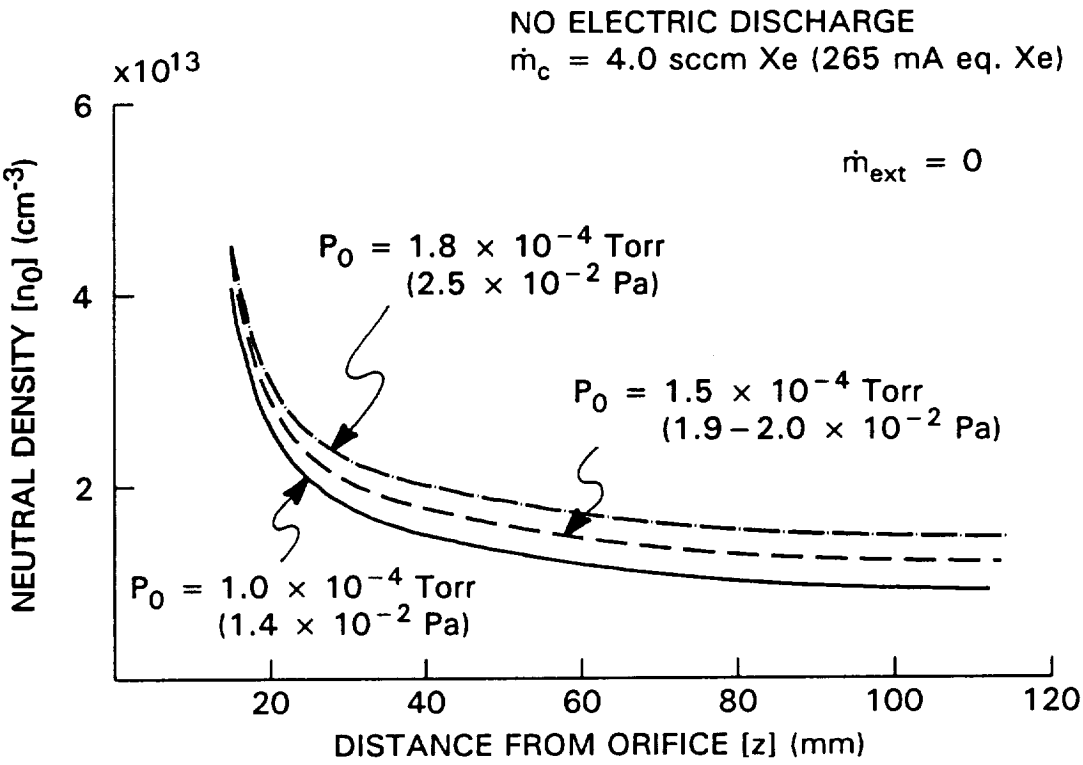


a. Effect of Ambient Pressure

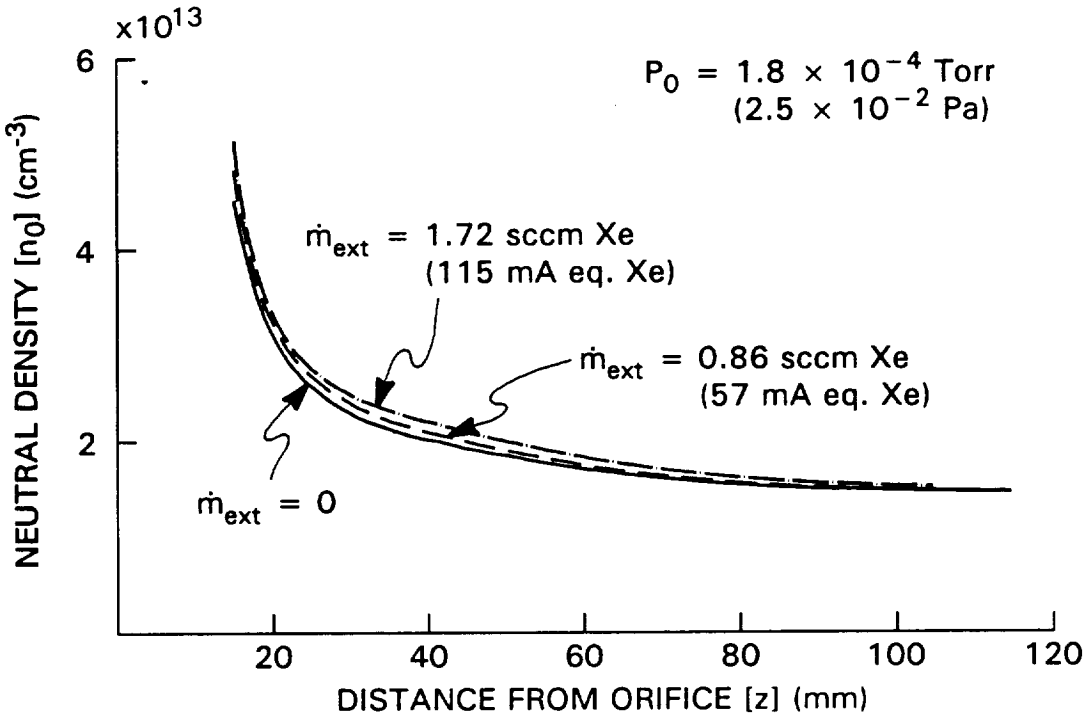


b. Effect of External Flow Rate

Fig. 13 Neutral Density Profiles Measured on the Centerline of the Cathode without Keeper

were obtained and found to be similar to those measured with a keeper (Fig. 12). Although it is not obvious from the figures, careful comparison indicates that the neutral density near the orifice is slightly higher with a keeper. The effect of this difference on the ion-current energy distribution, as predicted by the scattering model of Chapter III, would be, however, trivial when the accumulated effect of neutral density over typical ion paths is considered (Eq. (2)).

In order to examine accuracy of measurements, magnitudes of density profiles obtained from measured and extrapolated densities were compared with those predicted from orifice geometry and cathode flow rate using a continuum/free-molecular model at a zero external flow condition. In the model, it is assumed that the neutral density consists of additive main-cathode-flow-dependent and ambient-pressure-dependent components. The first component is computed from the cathode flow rate through the orifice assuming 1-D, isentropic, continuum flow from a stagnation temperature of 300 K through the cathode tube and through the orifice to the point where the Mach number reaches unity. The continuum velocity of xenon would be 199 m/sec at this point while the corresponding free-molecular thermal velocity would be essentially the same (190 m/sec). It is assumed that the flow turns abruptly free molecular and expands conically downstream of the unity-Mach-number transition point, which is still inside the orifice. The expansion cone matches the orifice shape (extreme diameters and thickness) and is characterized by an apex (source point) that is 3.7 mm upstream from the downstream face of the orifice and an 11° half angle. The second (ambient) component of density is computed using the ideal gas law, a measured ambient pressure, and the assumed gas temperature

(300 K).

Figure 14 compares the estimate obtained using this flow model (solid line) with measured/extrapolated neutral density profiles measured with and without a keeper over the range $z = 15-120$ mm and extrapolated for $0 < z < 15$ mm and $z > 120$ mm for the orifice flow rate of 4.0 sccm Xe. The extrapolations of the experimental data were accomplished by fitting the same continuum/free-molecular model to the measured profiles using parameters which reflected conical expansion from an origin offset from the orifice and the linear dependence on measured ambient pressure. The extrapolations were executed separately using data measured with and without a keeper to obtain the data shown in the two curves of Fig. 14. The figure shows that near the cathode theoretical neutral densities are an order of magnitude greater than the measured/extrapolated ones. It could be argued that the theoretical calculation shown here is a crude estimate. It is noted that the theoretical curve would agree more closely with the others, if the flow from the orifice were allowed to expand through a solid angle greater than that of the orifice, which is 0.11 sr and only $\sim 2\%$ of $2\pi$ sr (the solid angle associated with a half sphere). It is also noted that the measurements were obtained using a nude gauge with large active component sizes ($\sim 1$ cm in the direction normal to the cathode centerline) and this is expected to result in poor spatial resolution near the 0.81-to-1.47-mm-diameter cathode orifice.

When extrapolations of neutral density profiles with various external flow rates were needed to investigate the effects in the high-energy-ion-production models, a component associated with the external flow was added to the measured/extrapolated profiles just discussed. This external-flow-dependent component was observed to

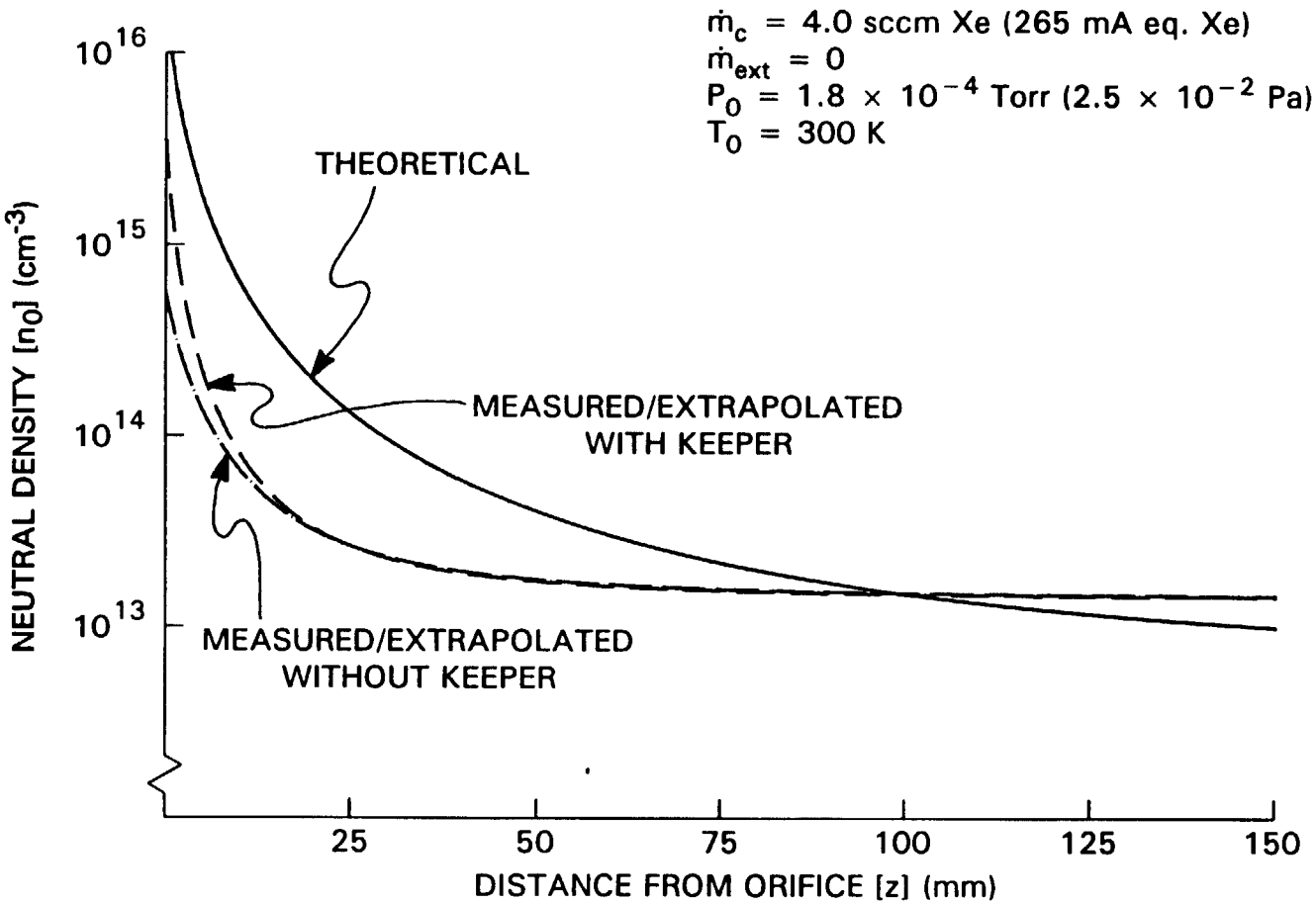


Fig. 14 Comparison of Theoretical and Measured/Extrapolated Neutral Density Profiles with Zero External Flow

drop exponentially as a function of distance from the orifice in the experiments and its origin was assumed to be 5 mm downstream of the orifice. The required parameters for the external-flow-dependent component are a flow-rate proportionality constant and a decay rate. They were determined using the approach associated with Fig. 14 for cases with and without a keeper.

2. Anode and Keeper Potentials

Figure 15 shows typical anode potentials along with keeper potentials if a keeper was installed. Potentials were measured with respect to cathode potential as functions of ambient pressure and external flow rate. As seen from the figure, the potentials were almost constant when the ambient pressure was changed and they decreased slightly when the external flow rate was increased. In all cases, however, the anode potential which was the highest electrode potential in the system, was less than 20 V with respect to cathode potential (the lowest potential surface in the system). Since the ion energies were measured with respect to cathode potential, one might at first glance expect them to be not significantly greater than those corresponding to the anode potential.

3. Ion-Current Energy Distributions

a. Typical Data and Analysis Scheme

Typical ion-current energy distribution data obtained with the keeper installed, which indicate the effect of changes in ambient pressure, are shown in Fig. 16a. These data, which are ion currents sensed directly by the ESA divided by its energy

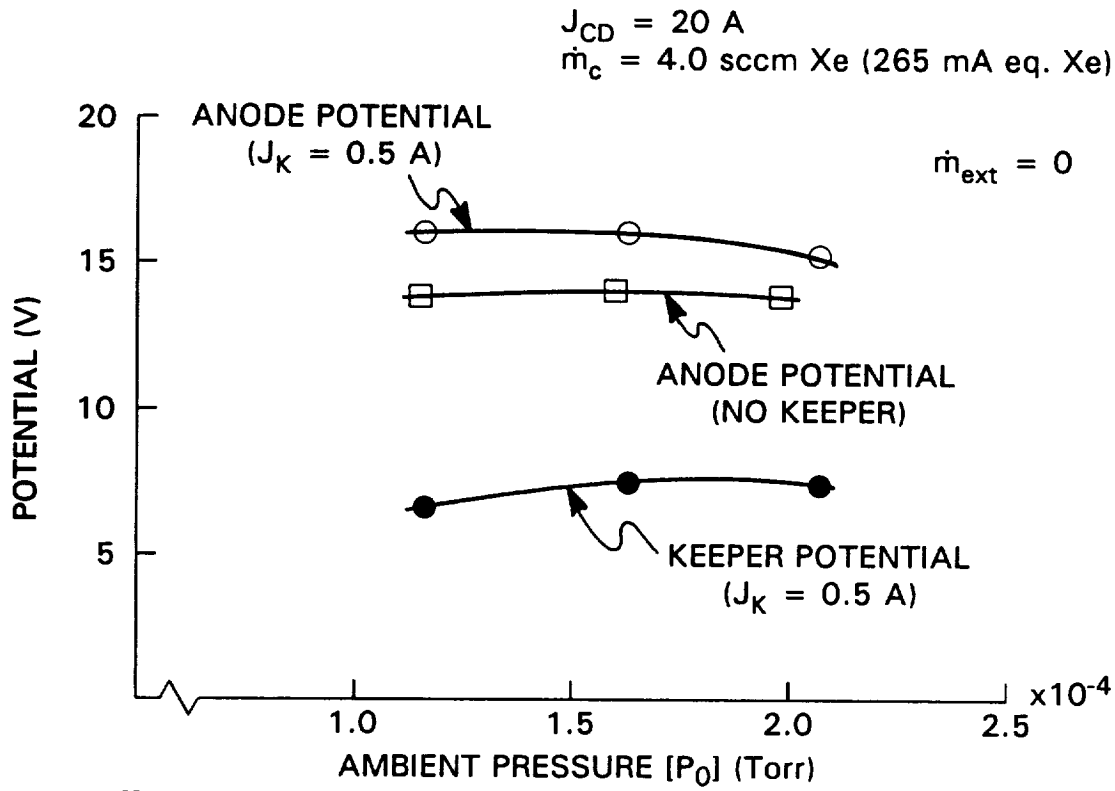


a. Effects of Ambient Pressure

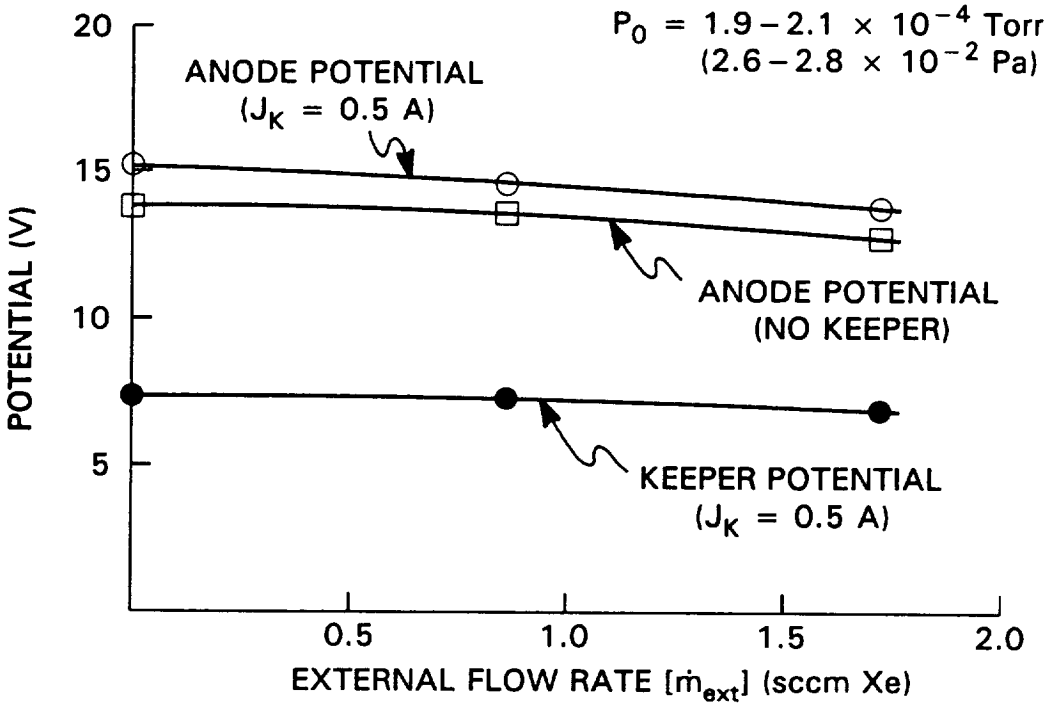


b. Effects of External Flow Rate

Fig. 15 Typical Anode and Keeper Potentials

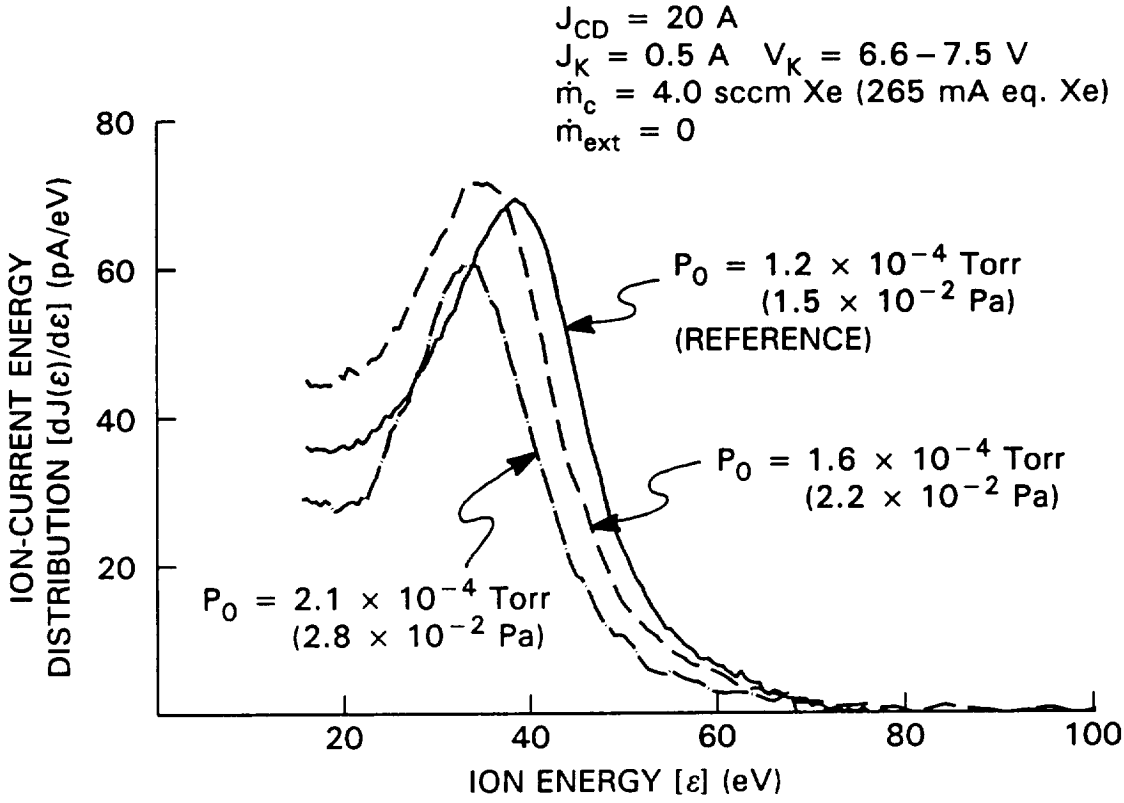


a. Measured Ion-Current Energy Distributions

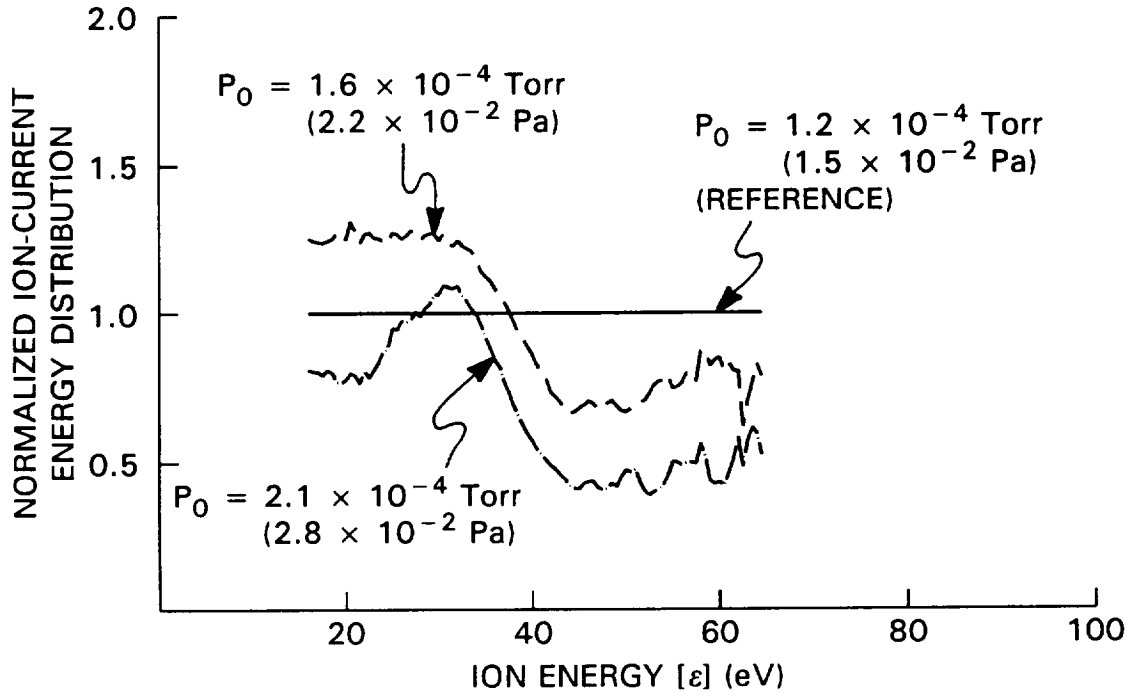


b. Normalized Ion-Current Energy Distributions

Fig. 16 Typical Ion-Current Energy Distribution Data

resolution,[20] were analyzed using Eq. (4) in Chapter III to obtain data suitable for comparison with scattering model predictions as shown in Fig. 16b. The analysis was accomplished by first selecting a reference distribution, $[dJ_i(\varepsilon)/d\varepsilon]_{ref}$ from among the measured ones. For the data of Fig. 16a, the one measured at the lowest ambient pressure (solid line) was picked. Then, normalized ion-current energy values were computed as the ratios of corresponding distribution values at each ion energy $[dJ_i(\varepsilon)/d\varepsilon]/[dJ_i(\varepsilon)/d\varepsilon]_{ref}$. The resulting curves plotted in Fig. 16b indicate the effect of the pressure change on the ion-current distribution. For example, the normalized distribution at $1.6 \times 10^{-4}$ Torr (dashed line) is greater than unity for energies less than $\sim 40$ eV and less than unity for energies greater than $\sim 40$ eV. This means that increasing the pressure above the reference state has induced an increase in the ion currents at energies below $\sim 40$ eV and a decrease in these currents at energies above $\sim 40$ eV. Of course, the normalized plot associated with the reference distribution in Fig. 16b is a horizontal line with a magnitude of unity.

Uncertainty and accuracy considerations limit the energy range over which normalized data can be presented. On the low side the energy limit corresponds to anode potential, which is considered to be close to ambient plasma potential, and on the high side it is defined as the energy at which the measured reference ion current has dropped to 5% of its maximum value.

b. Ambient Pressure Effects

Figure 17 shows the effect of ambient pressure on the normalized ion-current energy distribution for cases where the cathode was operated with and without a keeper. The reference profile for each figure is the lowest pressure one. It should be

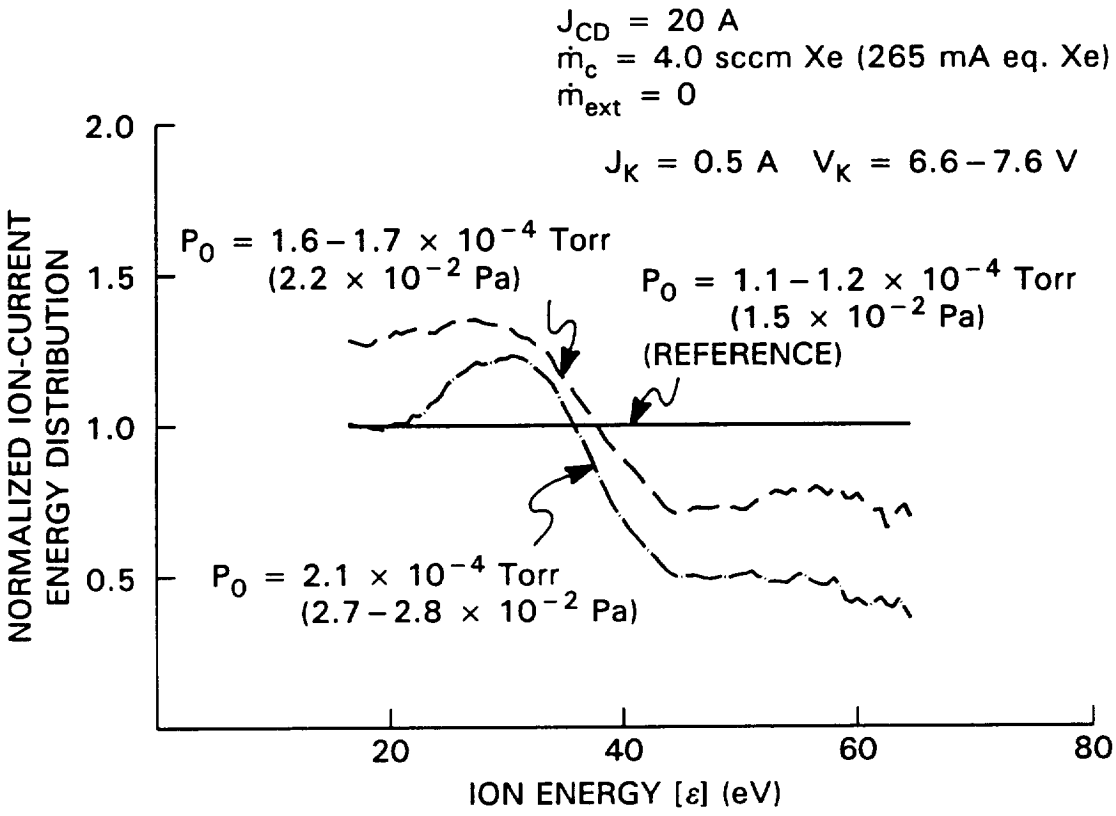


a. With Keeper

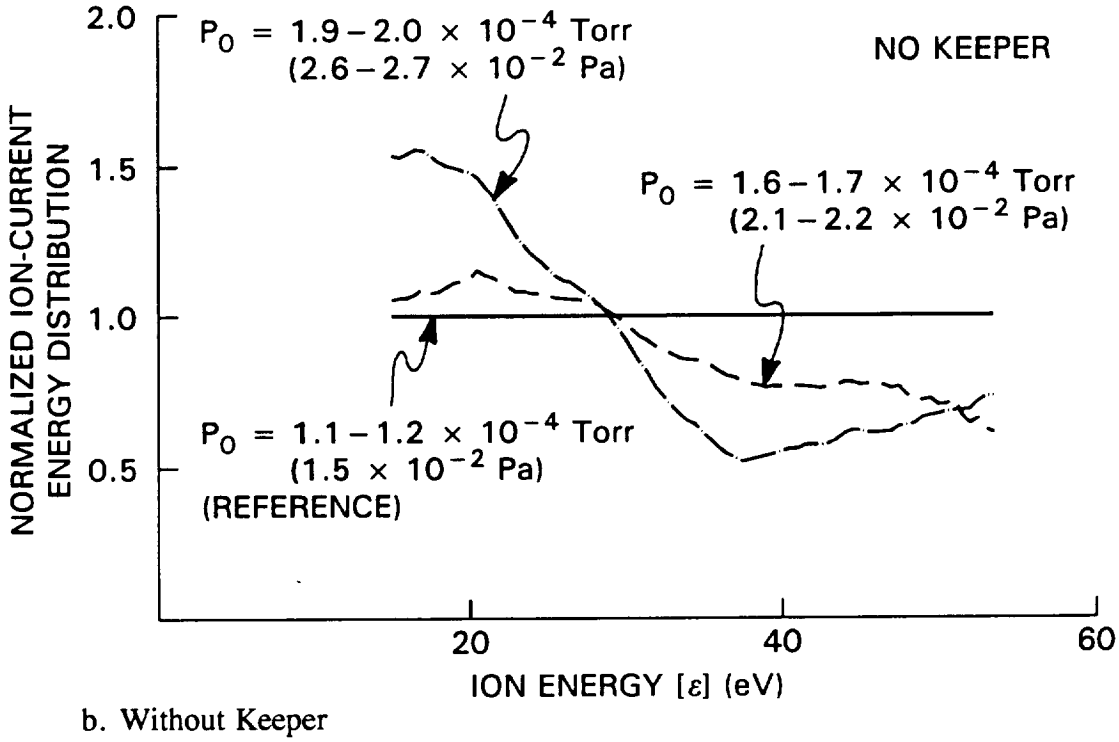


b. Without Keeper

Fig. 17 Effect of Ambient Pressure on Measured Ion-Current Energy Distributions

noted that the normalized distributions shown in Fig. 17a are slightly different from the ones shown in Fig. 16b since the distributions shown in Fig. 17 are the mean profiles from several different tests (see Appendix B) while Fig. 16 shows typical data obtained in a particular test series. In both cases with and without a keeper, increasing the ambient pressure causes smaller ion currents to flow at energies greater than 30−35 eV and greater ones at energies below this range.

The corresponding effect of ambient pressure predicted using the scattering model (i.e. the right-hand side of Eq. (4) in Chapter III with $z_1 = \sim 0$ mm and $z_2 =$ 180 mm, the distance between the cathode orifice and the ESA) are plotted in Fig. 18. It should be noted that the predictions are dependent only on the difference in the ambient pressure because only the difference in the neutral density profiles appears in Eq. (4). The scattering model reflects only the effects of collisional losses on the ions and it includes no mechanism for ion production. The ion current distribution of Fig. 18, therefore, shows a decrease over the entire energy range as neutral density is increased. Here, elastic collisions are represented by a hard-sphere model in which cross sections are determined directly from the atomic radius of xenon and are independent of relative ion kinetic energy while the charge-exchange cross section is only a weak function of this energy in this range.[21] The data in this figure, therefore, show a weak dependence on ion energy.

When the experimental results shown in Fig. 17 are compared with the predictions of Fig. 18, one sees reasonable agreement for energies above 35−40 eV except for energies above ~50 eV in Fig. 17b where crossover of curves occurs possibly because of the effect of noise. In all cases, agreement is poor at energies

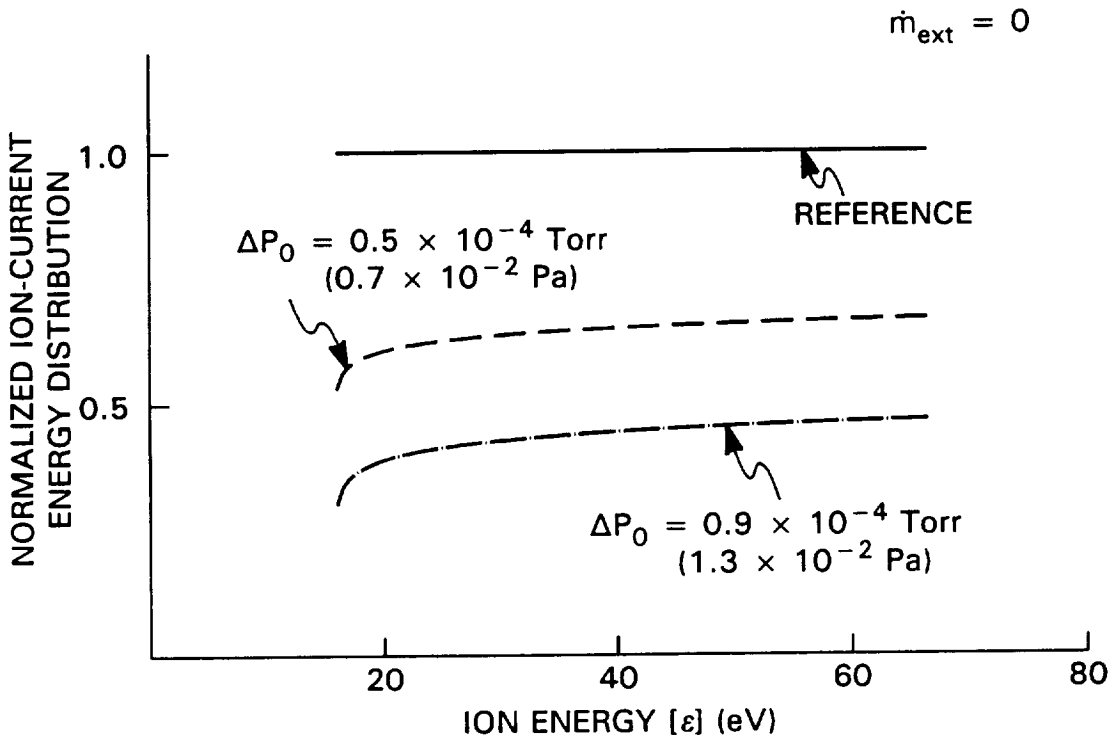


a. With Keeper

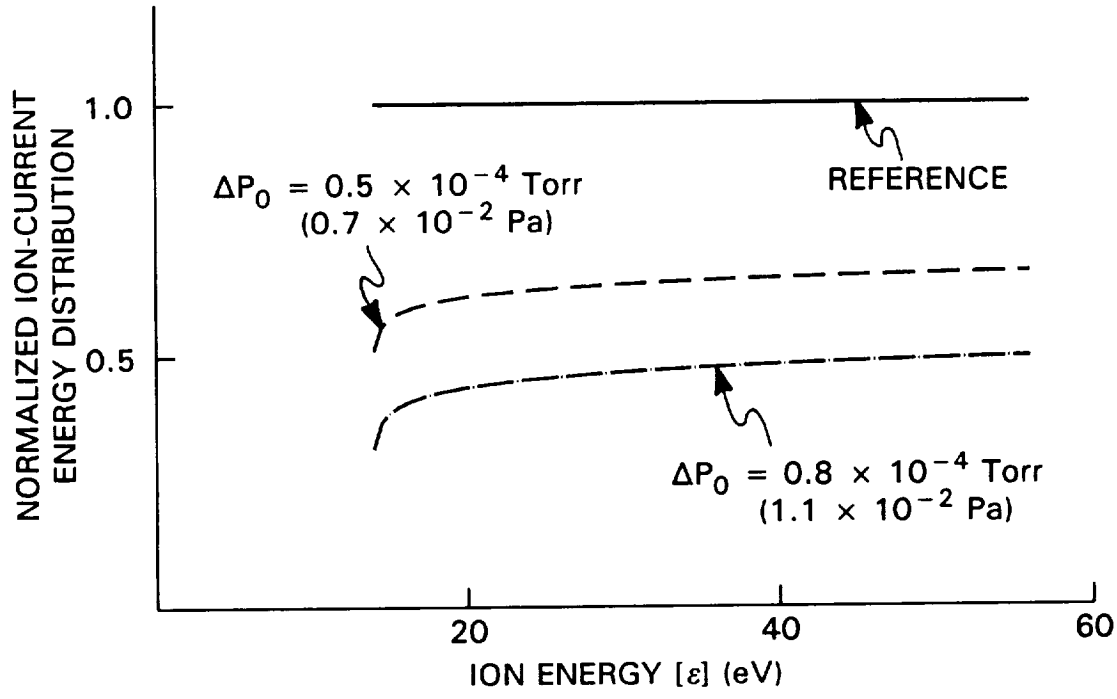


b. Without Keeper

Fig. 18 Effect of Ambient Pressure on Ion-Current Energy Distributions Computed using the Scattering Model

below 35−40 eV. There are, however, collisional mechanisms not reflected in the scattering model, which might explain this poor agreement at low energies. First, there could be collisions with neutrals which would cause ions to be scattered into the acceptance angle of the ESA or change their energy with almost no change in direction. Another mechanism, which could cause increases in ion currents at lower energies, would involve successive charge-exchange collisions with a small energy loss; the first collision would occur between high-energy ions and low-energy neutrals and the second between the resulting high-energy neutral and a low-energy ion would regenerate a high-energy ion. However, analysis shows these effects should be insignificant under the experimental conditions of Fig. 17. The first mechanism has a small effect because the small ESA acceptance angle (8°)[20] should prevent most of the collection of lower-energy ions created via scattering. The effect due to the second mechanism is small because the ion density is too low in the ambient plasma far from the cathode orifice to regenerate a significant high-energy ion current via charge-exchange collisions.

c. External Flow Rate Effects

The experimentally measured effects of external flow rate on normalized ion-current energy distributions are shown in Fig. 19 for cases where the cathode was operated with and without a keeper. Again these are mean curves and their precision is discussed in Appendix B. These data are similar to those associated with ambient pressure changes in that the normalized distributions drop at the higher energies and increase at lower ones as the external flow rate and, hence, the neutral density is increased. However, the flow rate changes induce both more consistent trends and

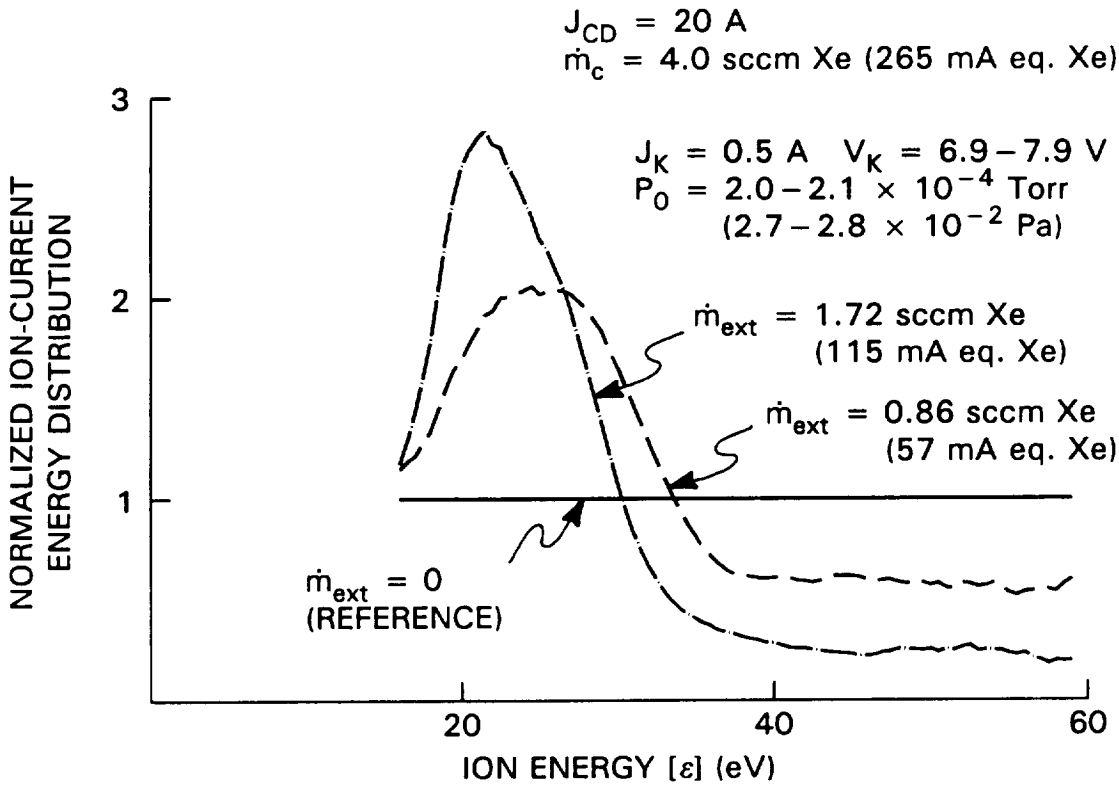


a. With Keeper

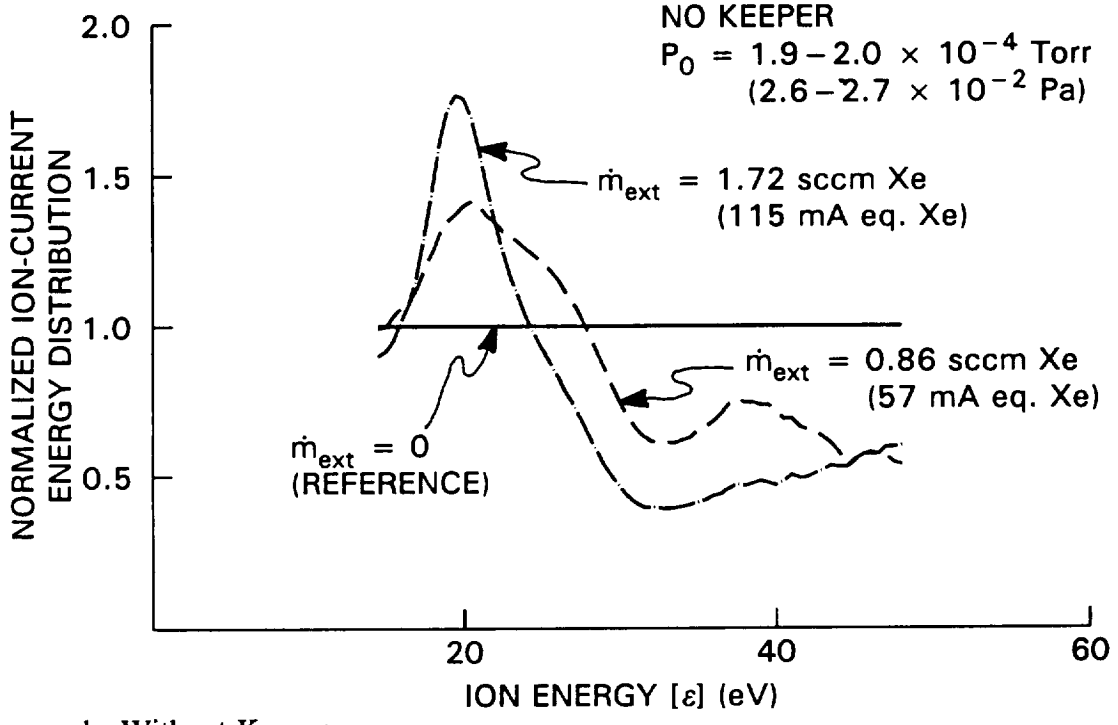


b. Without Keeper

Fig. 19 Effect of External Flow Rate on Measured Ion-Current Energy Distributions

greater changes in the magnitudes of the normalized ion currents than the changes in ambient pressure.

Figure 20 shows the predicted effect of external flow obtained from the scattering model described in Chapter III with $z_1 = \sim 0$ mm and $z_2 = 180$ mm. Again, ambient pressure is taken as arbitrary since only the difference in neutral density appears in the model. The plots of Fig. 20 all show that scattering alone should cause the normalized energy distribution of ion currents to decrease over the entire range of energies and depend only slightly on the ion energy as the flow is increased. It should also be noted that the drops in the normalized distributions are smaller than those predicted for the changes introduced in ambient pressure because the changes in neutral density profiles introduced by the external flows were smaller.

Recall that increases in ambient pressure resulted in increases in neutral density globally that caused reductions in the normalized ion-current energy distribution at energies above $\sim 35$ eV, which were in fairly good agreement with the predictions of the scattering model. Comparison of the data of Figs. 19 and 20 shows, however, that increasing the neutral density near the cathode by increasing the external flow rate does not yield such good agreement between predicted and measured normalized ion-current energy distributions in this energy range. This adds to the evidence that the scattering model, which is representative of the MHD mechanism, is not descriptive of the ion acceleration that takes place near a hollow cathode orifice.

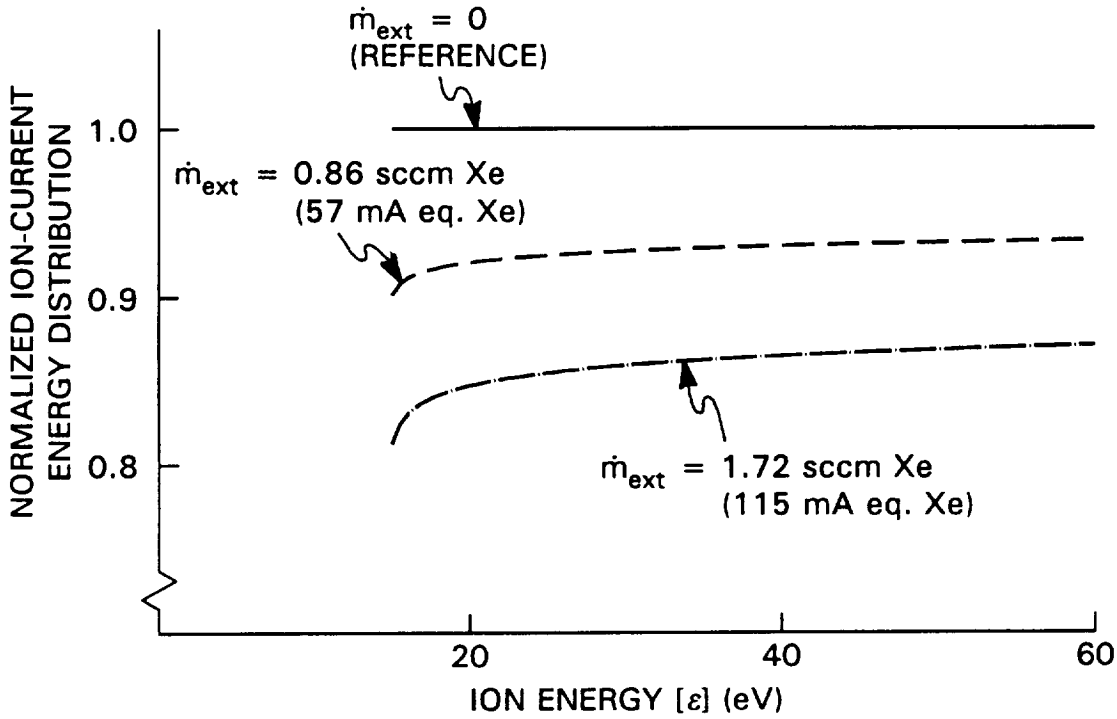


a. With Keeper

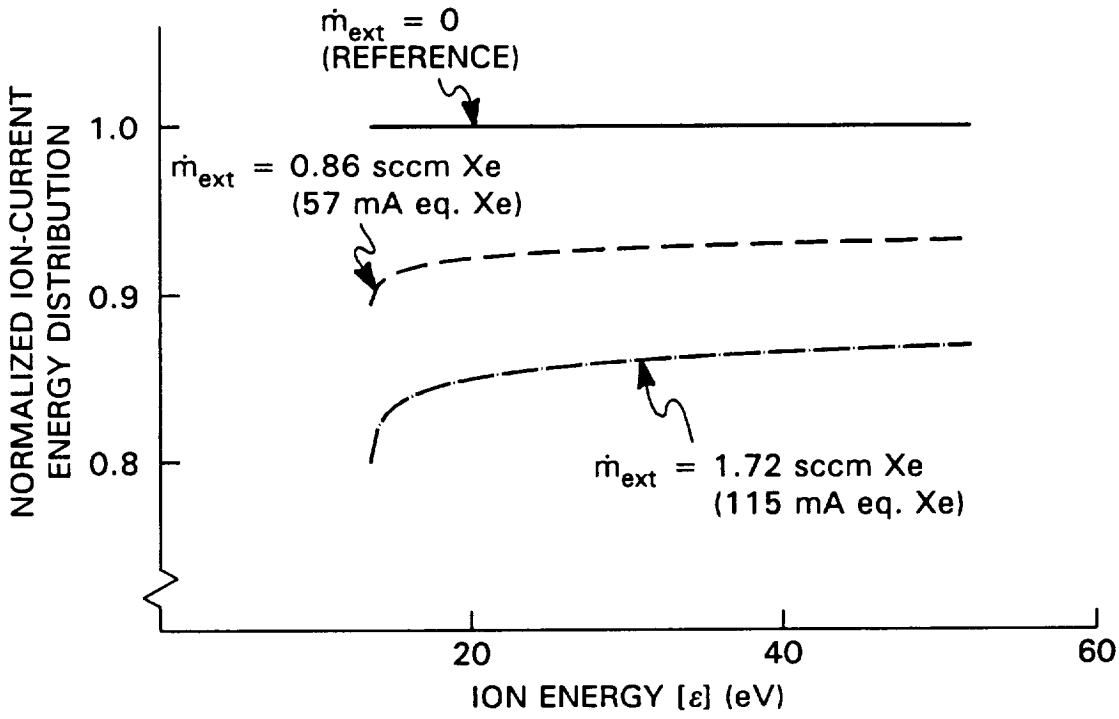


b. Without Keeper

Fig. 20 Effect of External Flow Rate on Ion-Current Energy Distributions Computed using the Scattering Model

## VI. Neutral Density Effects in the Potential-Hill Model

As seen in the previous chapter, the scattering model does not appear to offer an adequate explanation of experimentally observed ambient-pressure and external-flow-rate effects. For the MHD mechanism or any mechanism similar to it in the sense that energetic ions are assumed to be created inside the cathode or the orifice, no effect other than scattering is expected to change the ion-current energy distributions. In the potential-hill mechanism, which involves energetic ion production in a region of elevated potential downstream of the orifice, on the other hand, both ambient pressure and external flow could induce increases in ion currents at some energies.

### 1. Effect on the Height of the Potential Hill

In developing a model of the potential-hill mechanism to estimate the effect of neutral density profiles on the height of a potential hill, it is assumed that mono-energetic, primary electrons ejected through the hollow cathode orifice expand through a solid angle $\Omega$ into a downstream plasma as shown in Fig. 21a. In so doing they gain energies corresponding to the potential difference between the cathode and the potential-hill peak. These high-energy electrons then collide with neutral xenon atoms and create ions and low-energy electrons in the hill region ($z_u < z < z_d$). Any

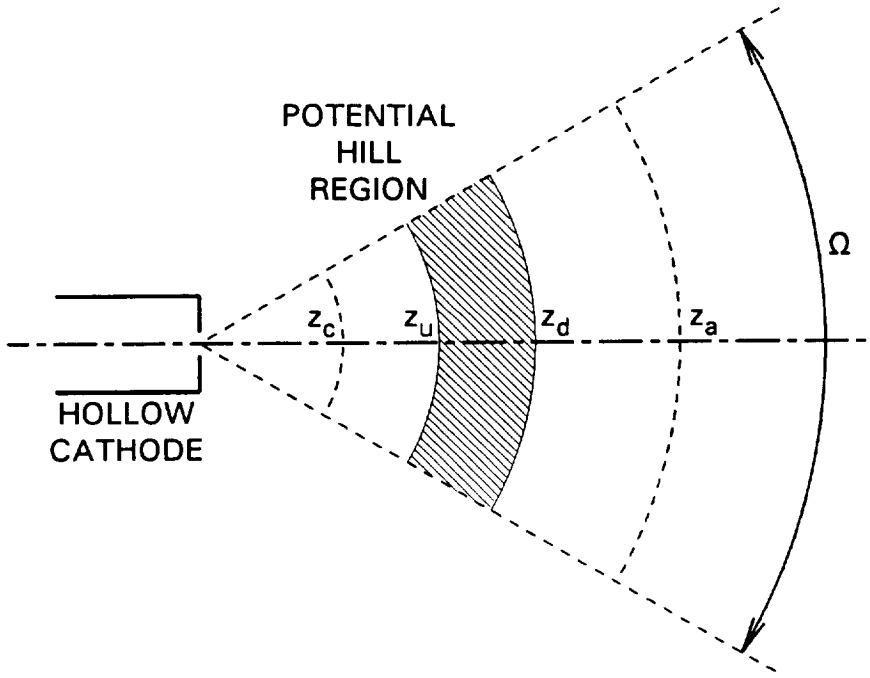


a. Geometry

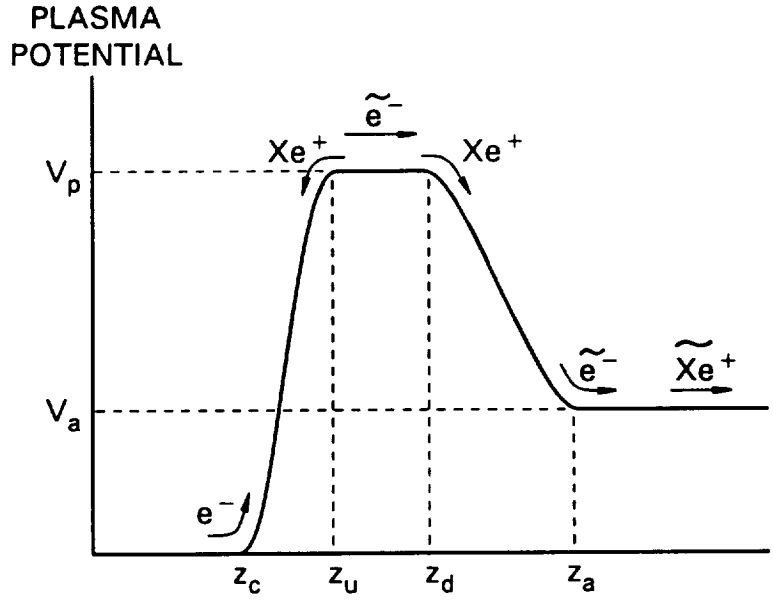


b. Plasma Potential Profile

Fig. 21 Potential-Hill Model

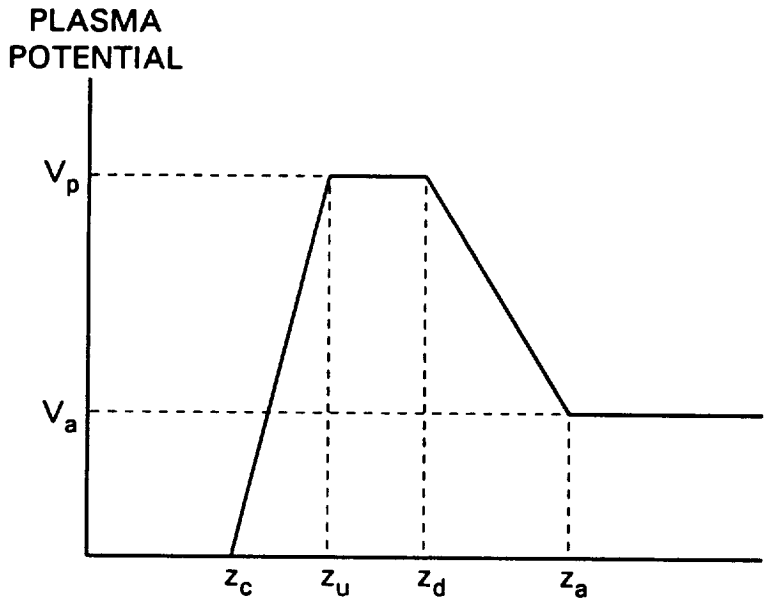


c. Simplified Plasma Potential Profile

Fig. 21 Potential-Hill Model (Continued)

excess, high-energy electrons which do not ionize neutrals pass through the hill region and flow directly into the ambient plasma ($z > z_a$). In the steady state, ions are removed from the potential-hill region by the electric fields that develop at its upstream and downstream boundaries while electrons resulting from impact ionization collide with each other and thermalize quickly into a group characterized by a Maxwellian distribution. These low-energy, Maxwellian electrons are trapped and they initially accumulate in the potential hill until their partial pressure becomes sufficient to enable them to overcome electric field forces at the edges of the hill and escape (the steady state). Figure 21b shows the plasma-potential profile that is postulated. The potential in the potential-hill region is assumed to be uniform at $V_p$ and upstream of the hill there is a boundary layer ($z_c < z < z_u$), within which ions and primary electrons counter-flow and across which the potential drops to the cathode potential. Downstream of the hill there is another boundary layer ($z_d < z < z_a$), within which ions and primary electrons flow downstream together and across which the potential decreases from the peak value of $V_p$ to $V_a$ in the ambient plasma.

In order to compute the continuous potential profile through a hill like that shown in Fig. 4b, the Poisson equation could be solved to determine the effects of the net electric charge distributed along the path. This approach is, however, complicated by the fact that singularities in ion speeds exist at the crest of the hill. This complication can be overcome by applying Gauss's law so the potential hill and point of singularity will be enclosed in the associated Gaussian surface. This approach was used and the potential profile was simplified further and represented by linear segments with discontinuous slopes as shown in Fig. 21c. Applying Gauss's law, the

following equation is obtained to relate the electric fields at the boundaries of and net charge within the potential-hill region:

$$\frac{V_p}{z_u - z_c}\,\Omega z_u^2 + \frac{V_p - V_a}{z_a - z_d}\,\Omega z_d^2 = \frac{e}{\varepsilon}\int_{z_u}^{z_d} (n_+ - n_e)\,\Omega z^2\,dz \tag{5}$$

where $n_+$ and $n_e$ are the densities of xenon ions and electrons, respectively.

The electron density in the hill region is assumed to be composed of both high-energy, primary (mono-energetic) and low-energy, Maxwellian groups. If losses from the primary group associated with ionization collisions are neglected, the primary electron density, $n_{ep}$, is determined by electron emission current from the cathode, $J_e$, through the equation

$$n_{ep} = \frac{J_e}{e\,v_{ep}\,\Omega z^2} \tag{6}$$

where $v_{ep}$ is the electron speed. This speed is, in turn, expressed using the peak potential and the mass of electron, $m_e$, by the equation

$$v_{ep} = \sqrt{\frac{2eV_p}{m_e}}\,. \tag{7}$$

The density of the low-energy, Maxwellian electrons trapped inside the hill must be greater than that of the electrons in the ambient plasma so the electron momentum balance can be maintained in the presence of the potential difference between the hill and the ambient plasma. This difference in densities is reflected in the Boltzmann (barometric) equation which incorporates the assumption that the electron temperature is uniform throughout the potential-hill and ambient plasma

regions. Specifically, the Maxwellian electron density, $n_{em}$, is related to the ambient electron density, $n_{ea}$, and the temperature, $T_{ea}$, by the equation

$$n_{em} = n_{ea} \frac{z_a^2}{z^2} exp\left[\frac{e(V_p - V_a)}{k_B T_{ea}}\right] \tag{8}$$

where $k_B$ is the Boltzmann constant. The second factor in the right-hand side of Eq. (8) accounts for spherical expansion effects in the model. It should be noted that the assumption of a uniform electron temperature is relatively crude and, therefore, open to eventual improvement. The total electron density on the hill is then expressed as a sum of the two components to obtain

$$n_e = n_{ep} + n_{em} = \frac{J_e}{e\,\Omega z^2 \sqrt{\frac{2eV_p}{m_e}}} + n_{ea} \frac{z_a^2}{z^2} exp\left[\frac{e(V_p - V_a)}{k_B T_{ea}}\right]. \tag{9}$$

If it is assumed that ions are created only on the top of hill, their production rate is given by

$$\int_{z_u}^{z_d} n_{ep}\, n_0\, \sigma_i\, v_{ep}\, \Omega z^2\, dz = \int_{z_u}^{z_d} \frac{J_e}{e\,\Omega z^2} n_0\, \sigma_i\, \Omega z^2\, dz = \int_{z_u}^{z_d} \frac{J_e}{e} n_0\, \sigma_i\, dz$$

where $n_0$ is the neutral density, which varies as a function of position, $z$, and $\sigma_i$ is the ionization cross-section, which depends on the energy of the ionizing (primary) electrons, $e\,V_p$. Once produced, these ions are assumed to escape randomly into the regions upstream and downstream of the potential hill with velocities $v_{iu}$ and $v_{id}$ and at rates $n_+\, v_{iu}\, \Omega\, z_u^2$ and $n_+\, v_{id}\, \Omega\, z_d^2$, respectively. In obtaining these expressions it is assumed that the ion density on the hill, $n_+$, is uniform. Equating the production

and loss rates of ions, one obtains

$$n_+ \, \Omega \left( v_{iu} z_u^{\,2} + v_{id} z_d^{\,2} \right) = \int_{z_u}^{z_d} \frac{J_e}{e} \, n_0 \, \sigma_i \, dz \; . \tag{10}$$

The velocities, $v_{iu}$ and $v_{id}$, at which the ions escape from the hill are determined by the Bohm condition for a stable sheath. When both low-energy, Maxwellian electrons with temperature $T_e$ and mono-energetic, primary electrons with energy $\varepsilon_p$ are present, the Bohm velocity, $v_B$, is given by

$$v_B = \sqrt{\frac{k_B T_e}{m_i} \, \frac{n_m + n_p}{n_m + \dfrac{k_B T_e}{2 \varepsilon_p} \, n_p}} \tag{11}$$

where $m_i$ is the ion mass and $n_m$ and $n_p$ are the densities of Maxwellian and primary electrons, respectively.[22] In the specific case discussed here, Eq. (11) is applied using the densities $n_{em}$ and $n_{ep}$ evaluated at $z_u$ to compute $v_{iu}$ and evaluated at $z_d$ to compute $v_{id}$ for $n_m$ and $n_p$, respectively. The electron temperature, $T_{ea}$, and the primary electron energy, $e \, V_p$, are assumed to be constant over the crest of the hill and used for the Maxwellian temperature and primary electron energy in Eq. (11). The ion density in the hill region can then be obtained using Eq. (10) in the form

$$n_+ = \frac{\displaystyle\int_{z_u}^{z_d} \frac{J_e}{e} \, n_0 \, \sigma_i \, dz}{\Omega \left( v_{iu} z_u^{\,2} + v_{id} z_d^{\,2} \right)} \; . \tag{12}$$

There is a backflow of positive xenon ions to the cathode as suggested in Fig. 21b. The electron emission current, $J_e$, which appears in Eqs. (9) and (12), will

be slightly different from the cathode discharge current, $J_{CD}$, because of this. In all the cases investigated here, however, the ion current flowing upstream from the hill region, $e\, n_+\, v_{iu}\, \Omega\, z_u^2$, is found to be so small compared to the electron emission current, $J_e$, that $J_e$ can be replaced with the gross, cathode discharge current, $J_{CD}$. It should be noted that the total current flowing through the cathode orifice is the sum of the discharge and keeper currents, $J_{CD}$ and $J_K$. However, only the discharge current flows to the ambient plasma through the potential-hill region and, therefore, only this component will appear in subsequent equations.

Finally, by substituting Eqs. (9) and (12) into Eq. (5), the peak potential, $V_p$, can be related to the parameters of the problem that describe cathode operation ($J_{CD}$ and $n_0$, which would in turn be determined by $\dot{m}_c$, $\dot{m}_{ext}$, and $P_0$), the potential-hill geometry ($z_c$, $z_u$, $z_d$, $z_a$, and $\Omega$), and the ambient plasma properties ($V_a$, $n_{ea}$, and $T_{ea}$). Before the effects of these parameters are investigated to determine which are most significant, it is instructive to examine the effect of peak potential on the two sides of Eq. (5). The results of doing this are shown in Fig. 22 for the typical values of the parameters given in Table 2. The values associated with the size of potential-hill region, $z_c$, $z_u$, $z_d$, and $z_a$, were selected from the size of luminous region observed in the experiments while the others were either controlled parameters ($J_{CD}$), based on the measurements ($V_a$ and $n_0$) in the experiments, or considered reasonable ($\Omega$, $n_{ea}$, and $T_{ea}$). The figure shows that the right-hand side of Eq. (5), which reflects the effects of the net charge in the hill region, is much greater in magnitude than the left-hand side. In fact, the left-hand side, which is computed from the electric fields, is indistinguishable from the axis of abscissa in the figure. This indistinguishability

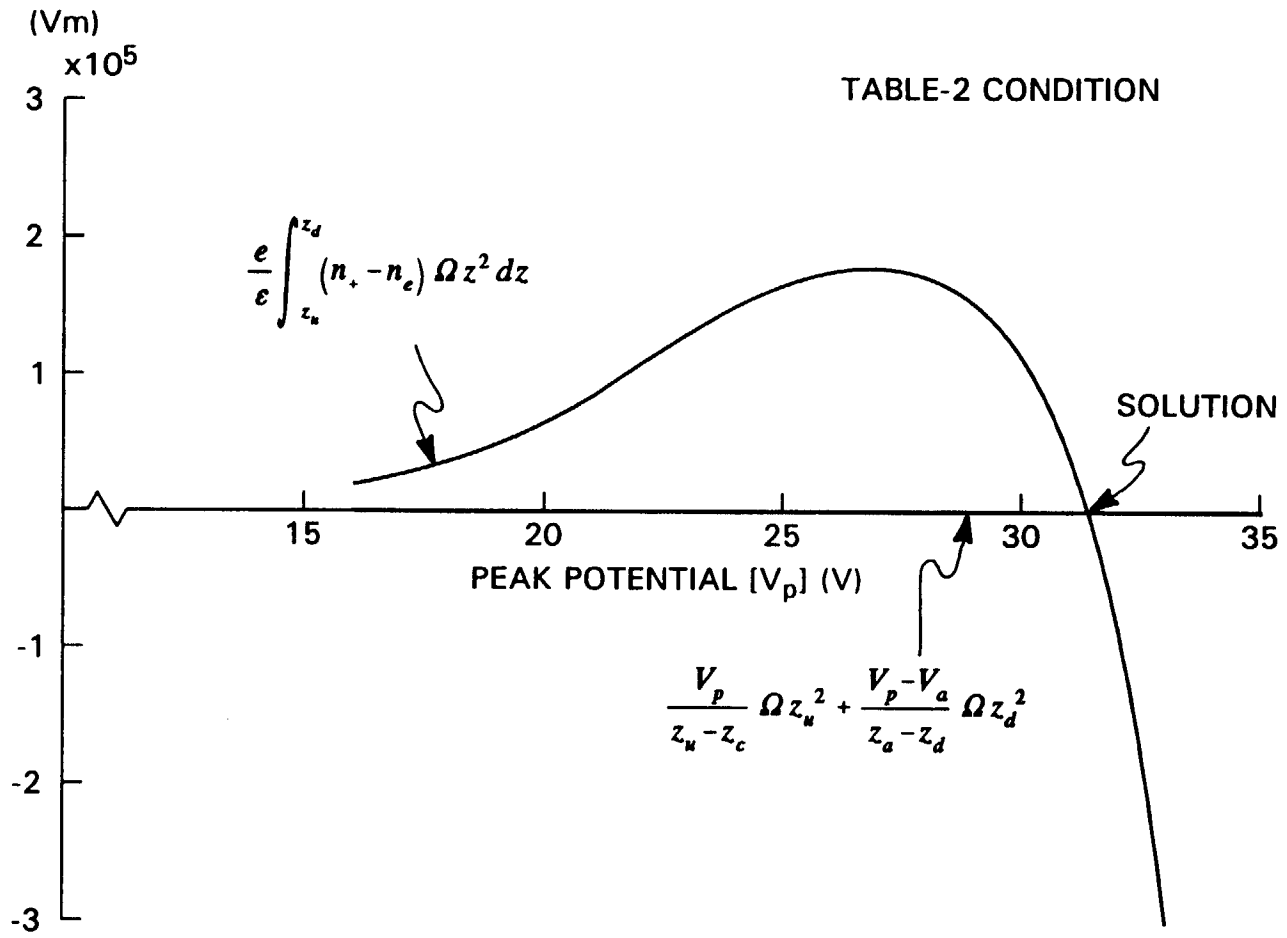


Fig. 22 Left- and Right-Hand Sides of Eq. (5)

Table 2 Nominal Values of Parameters Used in the Potential-Hill Model Calculations

| Geometrical Parameters | |
|---|---|
| Cathode Plasma Boundary [$z_c$] | 0.5 mm |
| Upstream Edge [$z_u$] | 1 mm |
| Downstream Edge [$z_d$] | 5 mm |
| Ambient Plasma Boundary [$z_a$] | 7 mm |
| **Cathode Discharge Condition** | |
| Discharge Current [$J_{CD}$] | 20 A |
| Solid Angle [$\Omega$] | $\pi$ sr |
| **Ambient Plasma Properties** | |
| Ambient Plasma Potential [$V_a$] | 16 V |
| Ambient Electron Temperature [$T_{ea}$] | 2 eV |
| Ambient Electron Density [$n_{ea}$] | $1 \times 10^{10}$ cm$^{-3}$ |
| **Neutral Density Parameters** | |
| Cathode Flow Rate [$\dot{m}_c$] | 4.0 sccm Xe (265 mA eq. Xe) |
| External Flow Rate [$\dot{m}_{ext}$] | 0 |
| Ambient Pressure [$P_0$] | $2.1 \times 10^{-4}$ Torr ($2.8 \times 10^{-2}$ Pa) |

The neutral density profiles used in analysis were those based on measurements made with a keeper installed.

remains even when sheath thicknesses, which appear in the denominators of the left-hand-side terms, are at their minimum (Debye length) values determined from the Maxwellian electron densities at $z_u$ and $z_d$. As the figure indicates, the solution corresponds to the peak potential where the two curves intersect and the fact that the left-hand side lies along the axis of abscissa indicates that the charges in the potential-hill region neutralize each other essentially completely. This enables one to neglect the left-hand side and rewrite Eq. (5) as follows:

$$\int_{z_u}^{z_d} n_+ z^2\, dz = \int_{z_u}^{z_d} n_e z^2\, dz$$

or

$$\frac{J_{CD}}{e\Omega}\frac{\sigma_i\int_{z_u}^{z_d} n_0\, dz}{\nu_{iu} z_u^{\,2} + \nu_{id} z_d^{\,2}}\frac{z_d^{\,3} - z_u^{\,3}}{3} = \left\{\frac{J_{CD}}{e\Omega\sqrt{\dfrac{2eV_p}{m_e}}} + n_{ea} z_a^{\,2} \exp\left[\frac{e(V_p - V_a)}{k_B T_{ea}}\right]\right\}(z_d - z_u)\,. \tag{13}$$

Again, it should be noted that the electron emission current, $J_e$, has been replaced by the cathode discharge current, $J_{CD}$.

The problem is now reduced to solving Eq. (13) for the peak potential, $V_p$, at prescribed operating and plasma conditions. It should be noted that the first term on the right-hand side of the equation, which is associated with the density of primary electrons from the cathode, is generally negligible compared with the second term, which is associated with the Maxwellian electron density. Thus, it will generally also be possible to neglect the primary electron term unless the electron temperature is

small. For this analysis, however, Eq. (13) was not simplified further because low electron temperatures were considered.

Peak potentials were computed as functions of the parameters of the problem using Eq. (13). Results obtained by varying the parameters around the nominal values given in Table 2 except the cathode plasma boundary, $z_c$, which was eliminated with the left hand side of Eq. (5), and the ambient plasma potential, $V_a$, which was considered to be constant, are shown in Figs. 23 to 26. Figure 23 shows the sensitivity of peak potential to variations in the geometrical parameters $z_u$, $z_d$, and $z_a$. The data of Fig. 23 indicate that the peak potential is relatively insensitive to variations in these parameters over the ranges and at the nominal values indicated in the figure.

The effects of discharge current and solid angle appear as the ratio $J_{CD}/\Omega$ in Eq. (13) and the sensitivity of peak potential to this ratio is shown in Fig. 24. The figure shows that peak potential undergoes a nominal increase as discharge current per unit solid angle is increased.

Peak potential is more sensitive to changes in the properties of the ambient plasma, which is assumed in the model to be coupled to the low-energy electrons in the hill region. This sensitivity is shown in Fig. 25. The fact that a greater electron temperature or lower electron density induce greater peak potentials is consistent with the idea that greater potentials are required to draw in the electrons needed to neutralize ion space charge when electron temperatures are greater and densities are lower. Results obtained to this point indicate that the peak potential is most sensitive to these parameters.

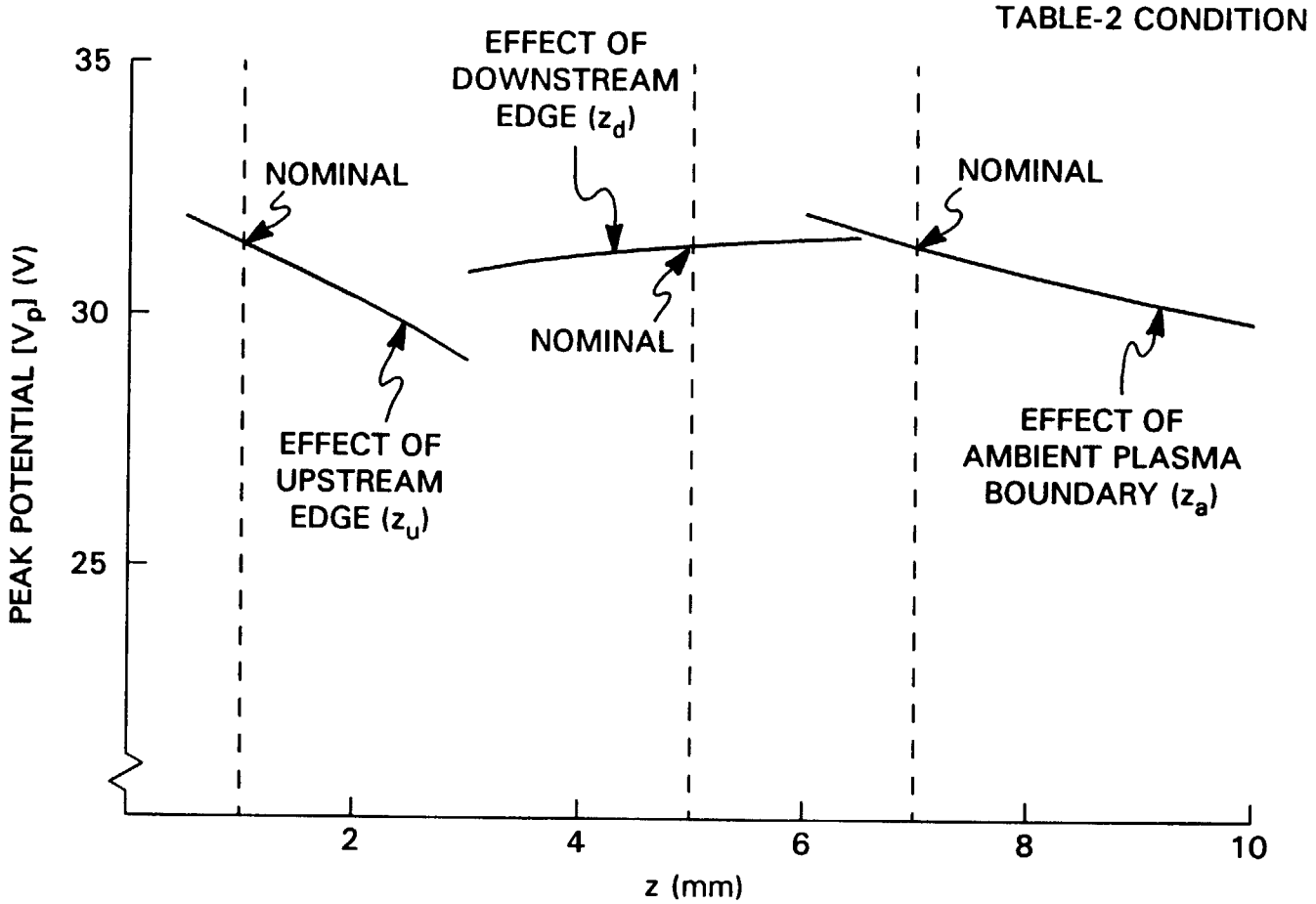


Fig. 23 Effects of Geometrical Parameters on Peak Plasma Potentials Computed using the Potential-Hill Model

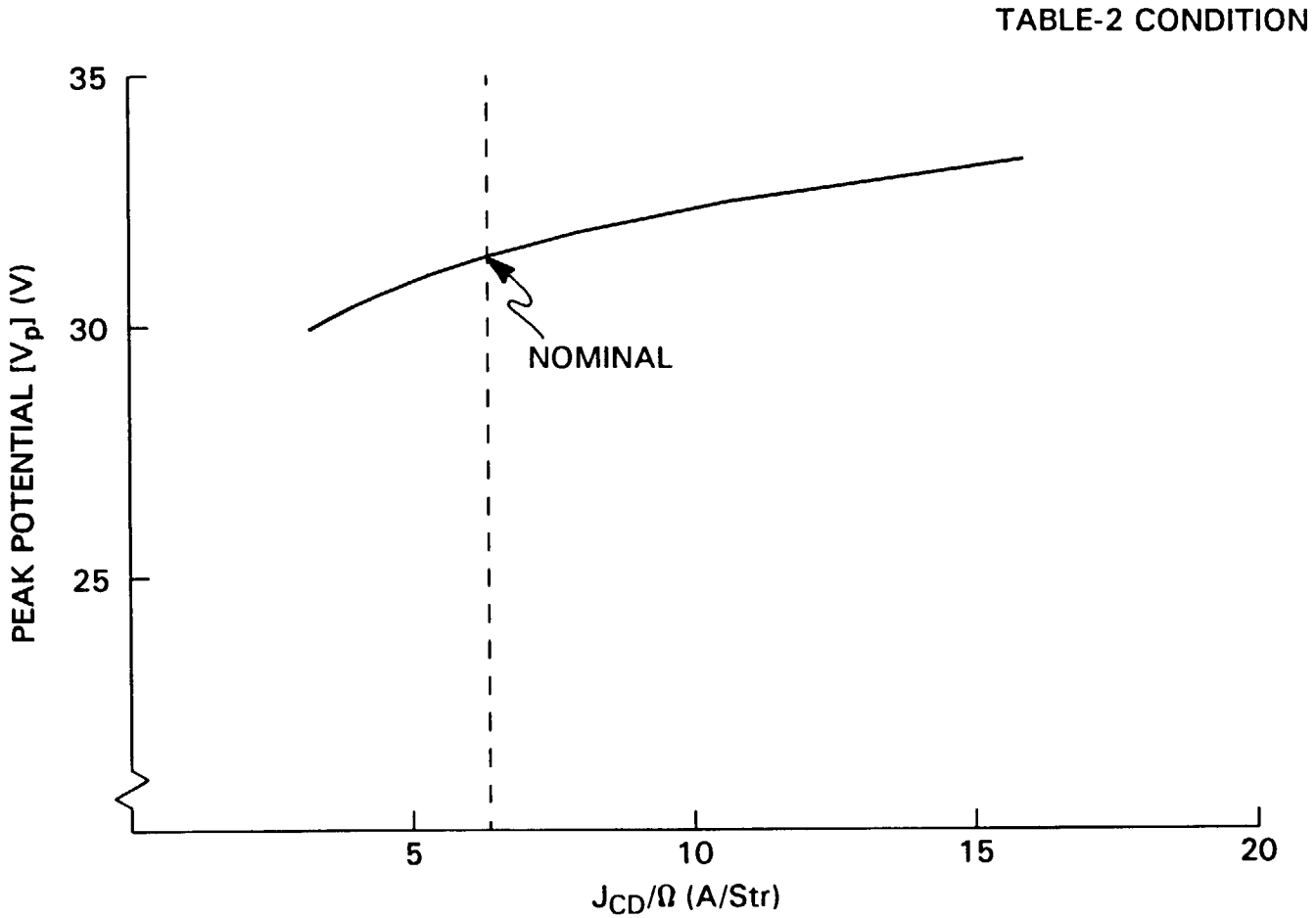


Fig. 24 Effect of Discharge Current per Unit Solid Angle on Peak Plasma Potentials Computed using the Potential-Hill Model

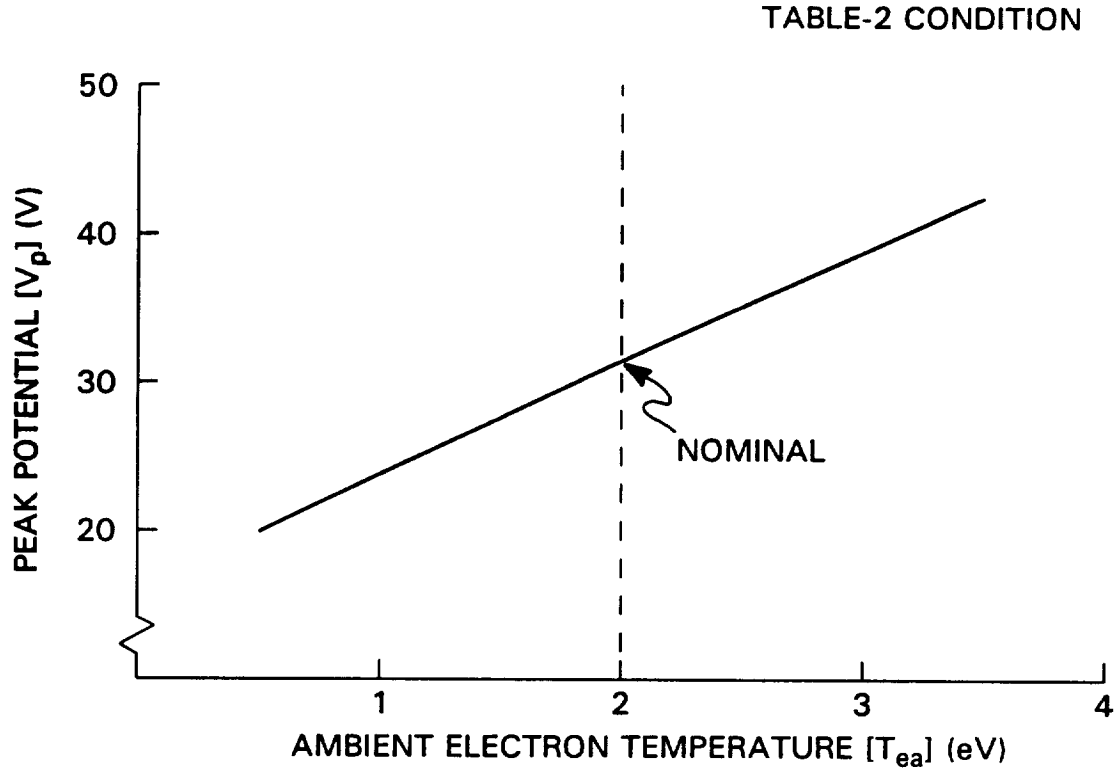


a. Effect of Ambient Electron Temperature

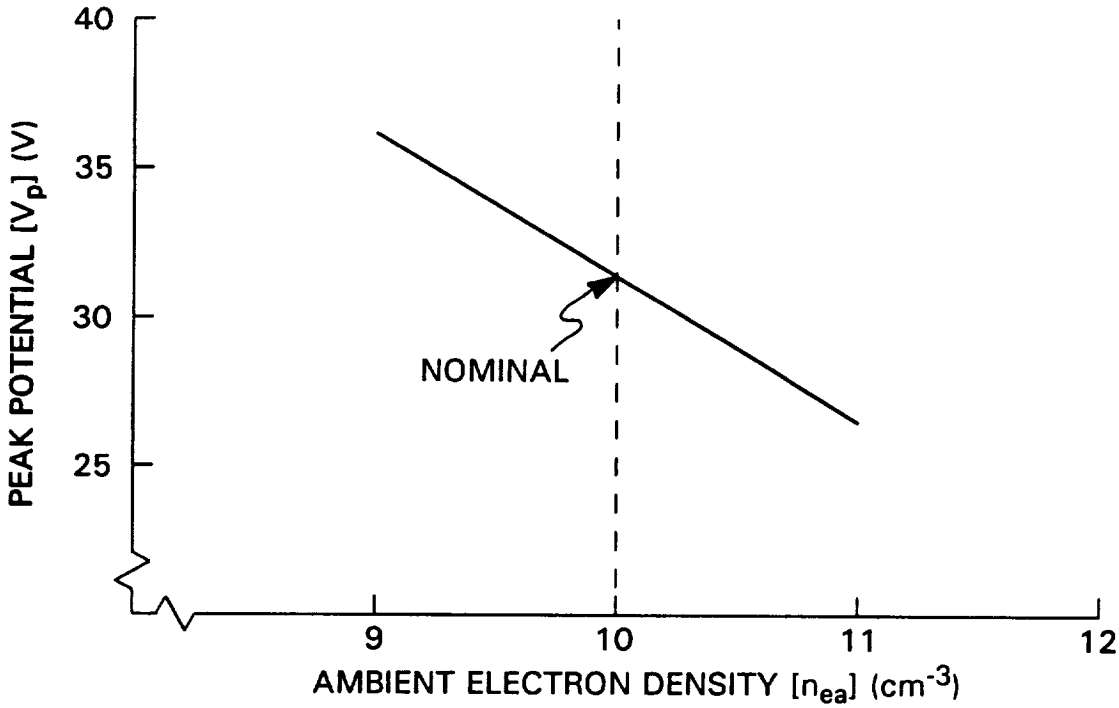


b. Effect of Ambient Electron Density

Fig. 25 Effects of Ambient Plasma Properties on Peak Plasma Potentials Computed using the Potential-Hill Model

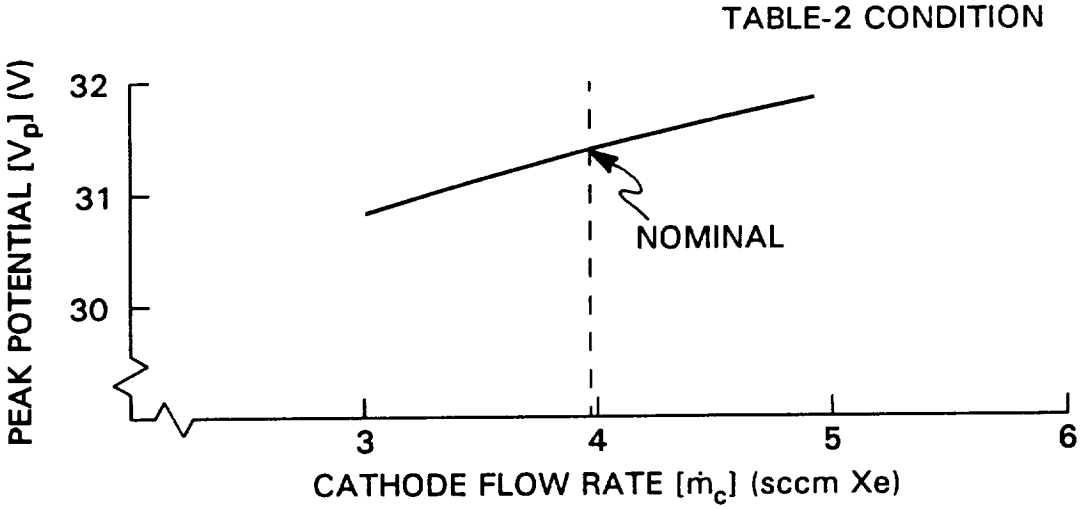


a. Effect of Cathode Flow Rate

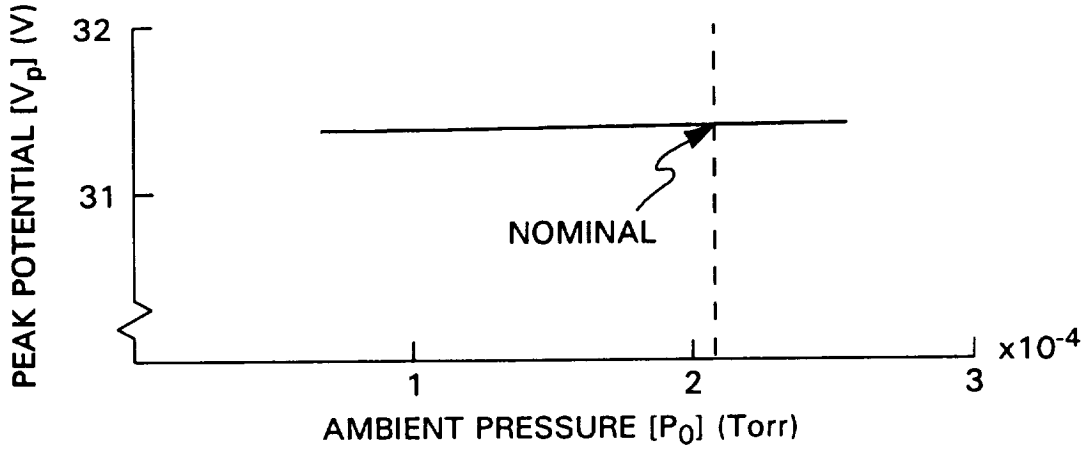


b. Effect of Ambient Pressure

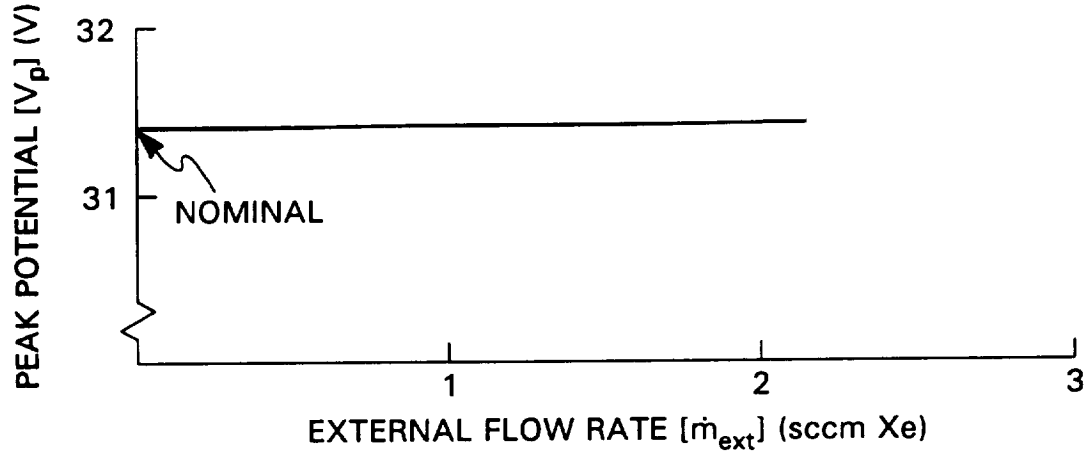


c. Effect of External Flow Rate

Fig. 26 Effects of Neutral Density Parameters on Peak Plasma Potentials Computed using the Potential-Hill Model

Figure 26 shows the sensitivity of peak potential to changes in the neutral density environment downstream of the orifice. Results shown in Fig. 26 suggest that changes in external flow rate and ambient pressure over the ranges used in the experiments should have a negligible effect on peak potential. At first glance, this appears inconsistent with the experimental results of Figs. 17 and 19, which reveal shifts in the ion-current energy distributions to lower energies as the ambient pressure or external flow rate was increased. It should be noted, however, that the electron temperature could vary with neutral density in the potential-hill region and this could affect the peak potential.

2. Effect of Charge-Exchange Collisions on Moderate-Energy Ion Production

The potential-hill model of high-energy ion production discussed in the preceding section is deficient 1) because it predicts ions are created only on the crest of the hill and will, therefore, all have the same energy (equal to the peak-to-cathode potential difference) and 2) because changes in neutral density parameters have just been shown to have a negligible effect on peak potential. These deficiencies can be addressed, however, by introducing the effect of charge-exchange collisions between the high-energy ions created on the hill and neutrals near the cathode. The effects should be significant because charge-exchange mean free paths are in the order of millimeters near the orifice at the neutral densities given in Fig. 14. These mean free paths are extremely small compared with 10-cm-order values in the ambient plasma.

The mechanisms involved can be understood by recognizing that ions created at the crest of potential hill undergo both acceleration and charge exchange as they

fall through the potential gradient on the downstream side of the hill. The low-energy ions that result from this process gain kinetic energies only as they fall down the rest of the potential hill so they are detected with moderate energies. Increases in neutral density induce increases in charge-exchange rates and, therefore, in the currents of these lower-energy ions even though the data of Fig. 26 showed neutral density changes had a negligible effect on the peak potential. It is noted that this effect will not be observed in any MHD-like model which does not involve the existence of a potential hill because all low-energy ions created by the charge-exchange collisions in the vicinity of orifice would be drawn upstream into the cathode by the adverse electric field shown schematically in Fig. 3b.

The ion-current energy distribution at position $z$ (and potential $V$) expressed as $dJ_i(\varepsilon)/d\varepsilon$ can be used to determine the charge-exchange-modified distribution at location $z + \Delta z$ (and potential $V - \Delta V$). The resulting distribution, which is the sum of a collisionless component of the original distribution at $z$ and a low-energy component generated by charge-exchange collisions, is given by

$$\left.\frac{dJ_i}{d\varepsilon}(\varepsilon)\right|_{z=z+\Delta z} = \left.\frac{dJ_i}{d\varepsilon}(\varepsilon)\right|_{z=z} exp\left[-n_0(z)\,\sigma_{ce}(\varepsilon - eV)\,\Delta z\right] + \delta(\varepsilon = eV)\int_{eV}^{\infty}\left.\frac{dJ_i}{d\varepsilon}(\varepsilon)\right|_{z=z}\left(1 - exp\left[-n_0(z)\,\sigma_{ce}(\varepsilon - eV)\,\Delta z\right]\right)d\varepsilon \tag{14}$$

where $\delta$ is a function which takes a magnitude of $1 / (e\,\Delta V)$ in the range of $e(V - \Delta V / 2) < \varepsilon < e(V + \Delta V / 2)$ and is zero otherwise and $\sigma_{ce}$ is the charge-exchange collision cross-section. By applying Eq. (14) repeatedly from position $z_d$, the downstream edge of potential hill where all ions have an energy corresponding to the

escape velocity, $v_{id}$, and a current, $e\, n_+\, v_{id}\, \Omega\, z_d^2$, the ion-current density distribution at position $z_a$, the upstream boundary of ambient plasma, can be determined. The downstream distribution at $z_a$ is dependent upon the neutral density and potential profiles downstream of the crest.

Assuming a linear potential variation from the peak potential at $z_d$ to ambient potential at $z_a$ as shown in Fig. 21c and using neutral densities extrapolated from data in Fig. 12, the results plotted in Fig. 27 were obtained. These results show that increasing the neutral density by either increasing the ambient pressure or the external flow rate induces increases in the ion-current distribution with energies in the range associated with the peak and ambient plasma potentials at the base of the potential hill, $z_a$. If the effects of scattering and charge-exchange collisions between this location and the point of ion-current detection are applied to the data of Fig. 27 to obtain a prediction of what an ESA would sense, the data of Fig. 28 are obtained. The comparison of data in Figs. 27 and 28 shows that the effect of the collisions that occur in the ambient plasma dominates over the charge-exchange effects that occur on the downstream side of the potential hill, $z_d < z < z_a$. Further, the computed effect of ambient pressure is greater than that of external flow rate and this is opposite to the measured observation. It should be recalled, however, that the pressure data used to estimate the neutral density profiles are based on an extrapolation into the potential-hill region and these densities may be underestimated at that location.

The measured and computed results would be brought into closer agreement if greater neutral density changes near the cathode and lesser ones downstream of it were used in the numerical model. It should be remembered that the neutral density

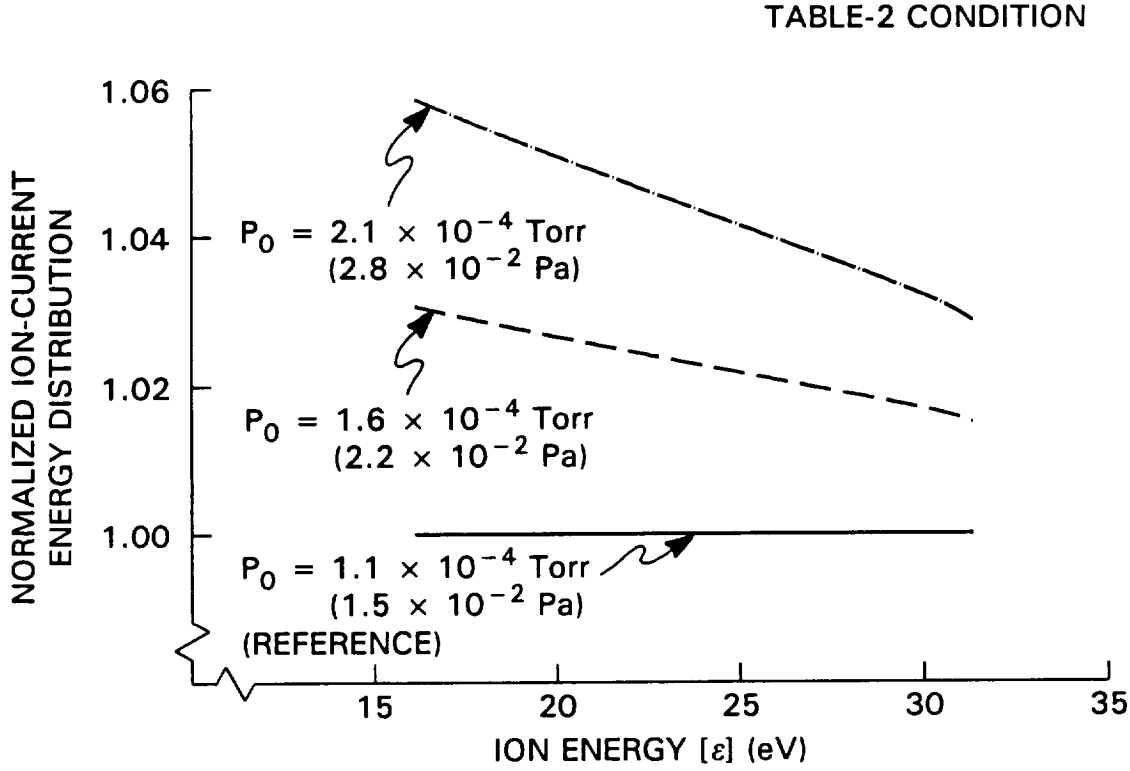


a. Effect of Ambient Pressure

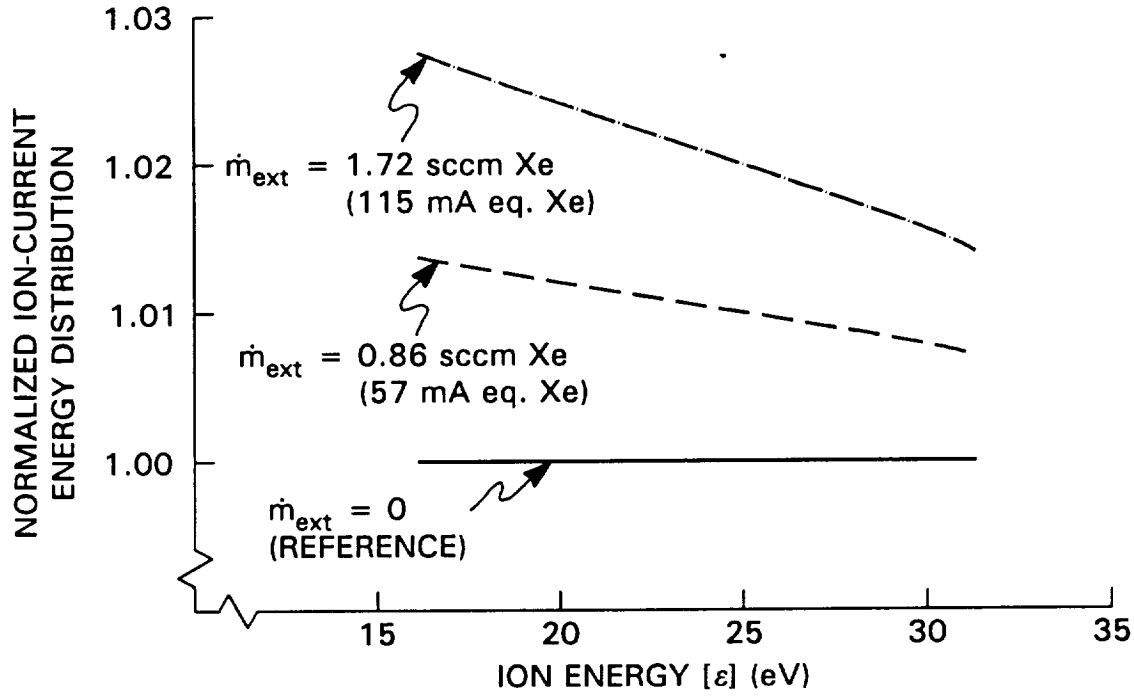


b. Effect of External Flow Rate

Fig. 27 Effects of Neutral Density Parameters on Ion-Current Energy Distributions at the Ambient Plasma Boundary Computed using the Potential-Hill Model

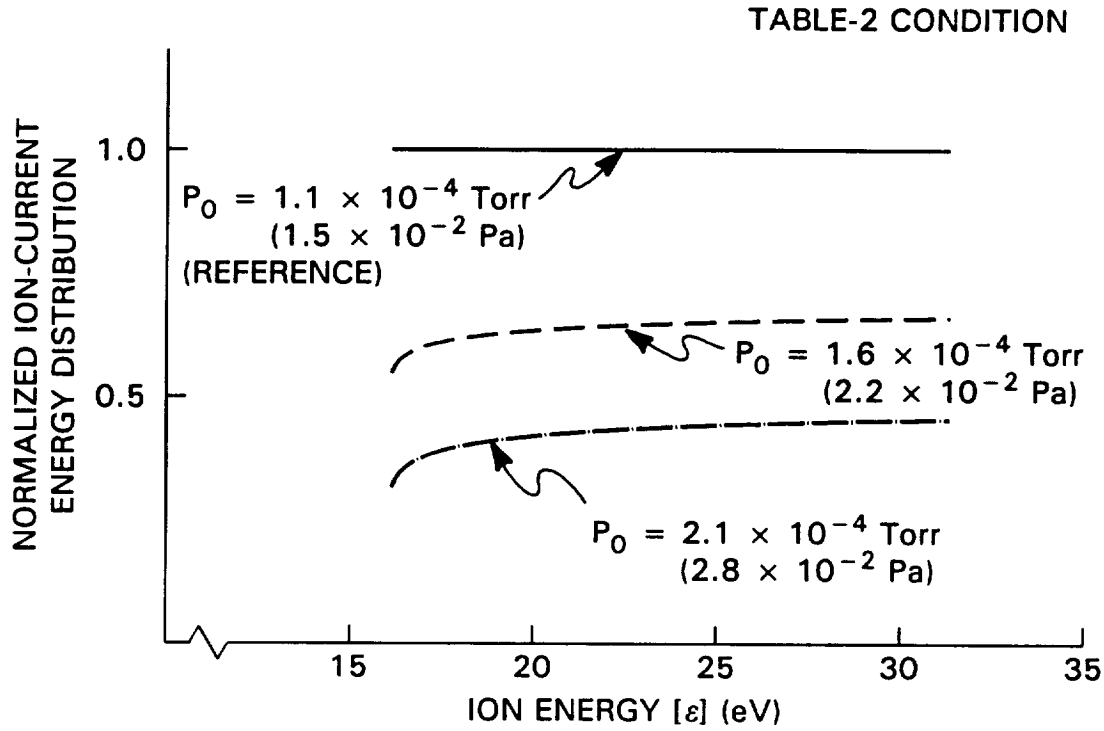


a. Effect of Ambient Pressure

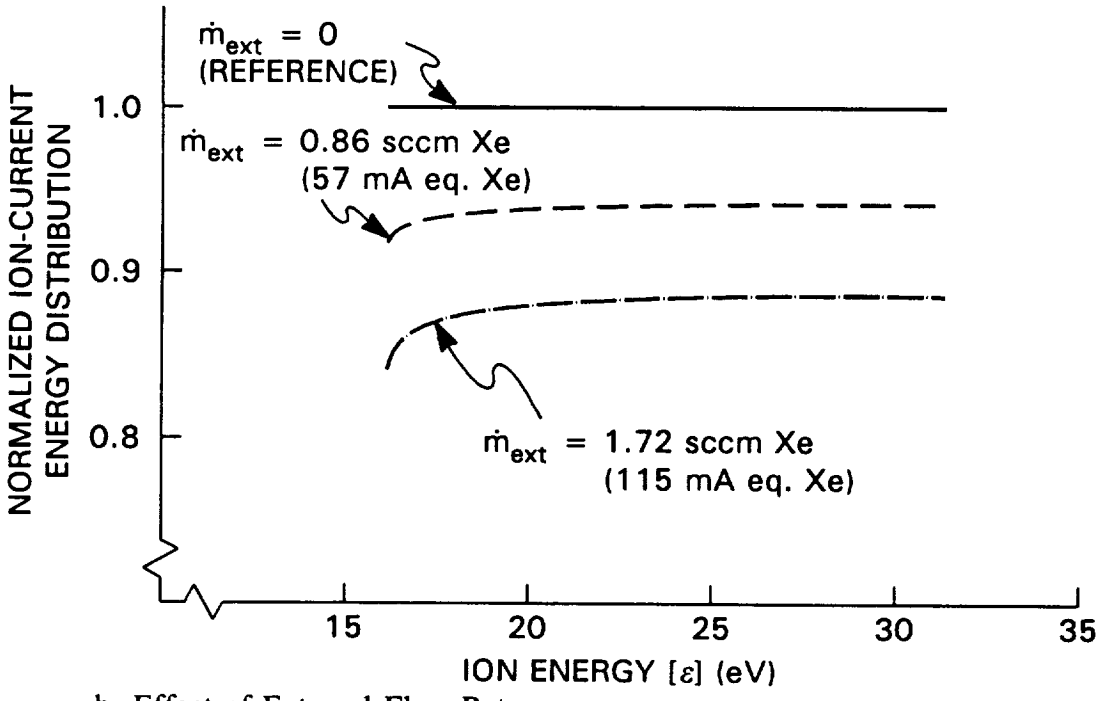


b. Effect of External Flow Rate

Fig. 28 Effects of Neutral Density Parameters on Ion-Current Energy Distributions 180 mm downstream from the Orifice Computed using the Potential-Hill Model

profiles are approximated using three components with different dependencies on the distance from the cathode: uniform, proportional to the reciprocal to the square of the distance with an offset, and exponential. The second component causes the density to increase most near the orifice and least for downstream. In order to show a possible closer agreement of the results obtained in the potential-hill model with the measurements including the scattering collision effects in $z_d < z < z_a$, this component was increased artificially. A 100% increase yields the ion-current energy distribution plotted in Fig. 29. It shows about a 40% increase in ion current in the energy range from 16 to 31 eV. It should be noted that increases shown in this figure would not be expected when the other two neutral-density components are increased since the increase of neutral density near the cathode would not dominate over the increase downstream.

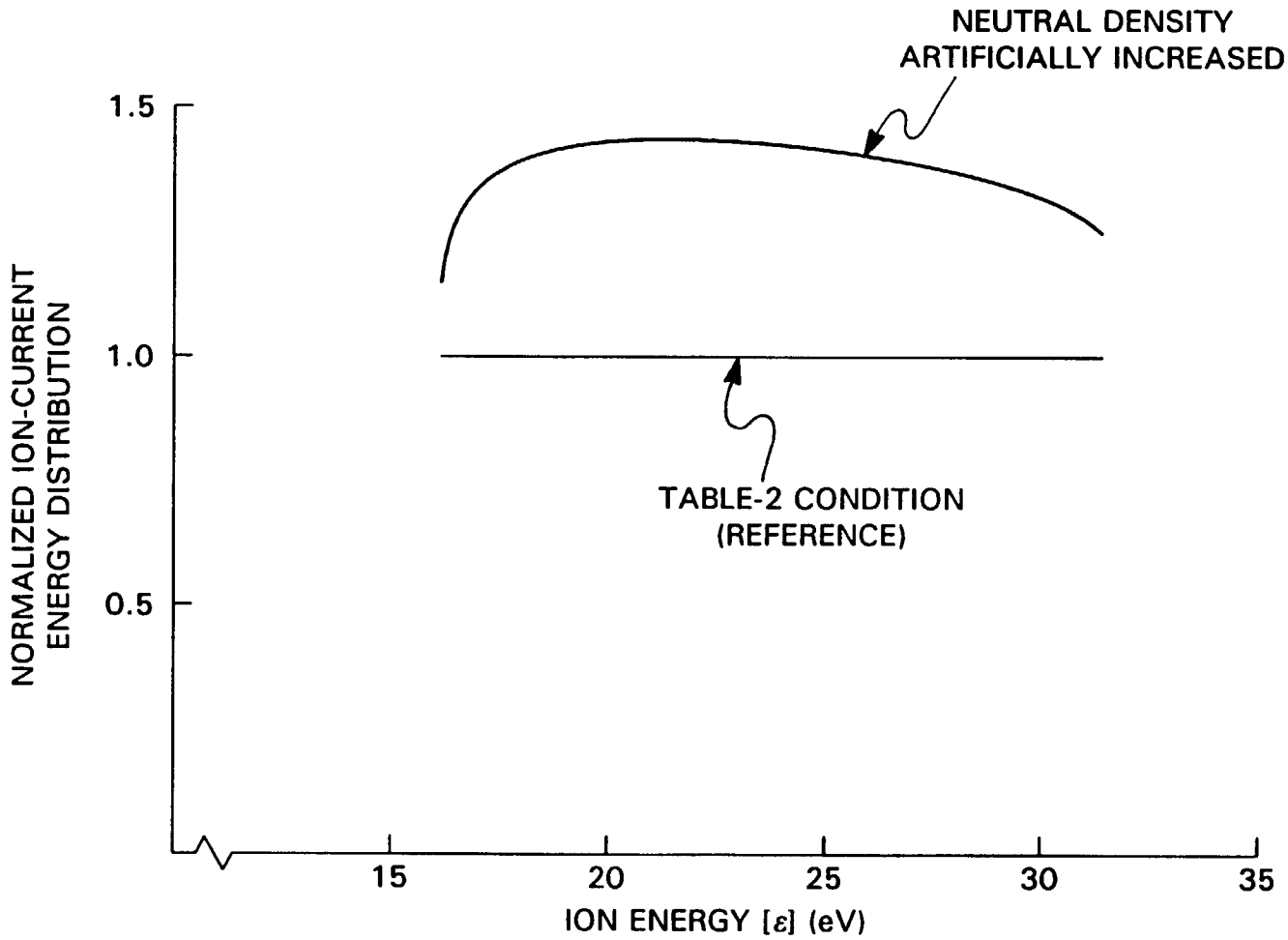


Fig. 29 Change of Ion-Current Energy Distribution 180 mm downstream from the Orifice Computed using the Potential-Hill Model with Artificially Increased Neutral Density

# VII. Conclusions

Energy distributions of ion currents measured downstream of high-current hollow cathodes using an electrostatic energy analyzer confirm the existence of substantial currents of ions with energies greater than that associated with the cathode-to-anode potential difference ($\sim 16$ V). Either increasing the ambient pressure or adding external flow introduced immediately downstream of a hollow cathode operating under nominal, high-current conditions induces an increase in the distribution of ion currents with moderate energies ($\varepsilon < \sim 25$ to $\sim 35$ eV) and a decrease in the distribution for high energies ($\varepsilon > \sim 25$ to $\sim 35$ eV). The magnitude of the current distribution increase in the moderate energy range is greater for a cathode equipped with a toroidal keeper than for one without a keeper, but the distribution in the high energy range does not seem to be affected by a keeper.

There is no mechanism by which the ion current at any energy can be increased significantly by increasing the downstream neutral density in the MHD model of energetic-ion production in high-current hollow cathodes. Hence, the measured effects of increased neutral atom density cannot be explained using this model. The potential-hill model of energetic-ion production does include a charge-exchange mechanism through which changes in neutral atom density could induce combined increases in the currents of ions with moderate energies and decreases in

high energy ions. The existing, simplified version of the potential-hill model does not yield ion-current-energy-distribution changes induced by neutral density changes that agree with measured distribution changes.

# VIII. Future Work

The present potential-hill model can be improved by 1) allowing ion production and charge-exchange processes to occur over the entire hill (i.e. at all potentials) and 2) by using neutral density data that are both more accurate and measured closer to the cathode. Methods such as those involving laser-induced fluorescence (LIF) should be considered 1) to achieve better spatial resolution especially near the cathode orifice and 2) to enable measurement during actual cathode operation. This potential-hill model could also be improved by modification of the Boltzmann (barometric) equation to reflect such effects as a non-uniform electron temperature.

## IX. References


1. Fearn, D.G., Singfield, A., Wallace, N.C., Gair, S.A., and Harris, P.T., "The Operation of Ion Thruster Hollow Cathodes using Rare Gas Propellants," AIAA Paper 90-2584, 21st International Electric Propulsion Conference, Orlando, Florida, July 18–20, 1990

2. Aston, G., "Ion Propulsion Technology Requirements for Planetary Mission Applications," AIAA Paper 85-2000, 18th International Electric Propulsion Conference, Alexandria, Virginia, September 30–October 2, 1985

3. Aston, G., "Ferry to the Moon," Aerospace America, June, 1987, pp. 30–32

4. Fearn, D.G., "The Ulysses Mission: The Ion Propulsion Alternative," IEPC Paper 91-036, 22nd International Electric Propulsion Conference, Viareggio, Italy, October 14–17, 1991

5. Fearn, D.G., "A Mission to Pluto using Nuclear Electric Propulsion," IEPC Paper 93-200, 23rd International Electric Propulsion Conference, Seattle, Washington, September 13–16, 1993

6. Patterson, M.J., and Verhey, T.R., "5kW Xenon Ion Thruster Lifetest," AIAA Paper 90-2543, 21st International Electric Propulsion Conference, Orlando, Florida, July 18–20, 1990

7. Brophy, J.R., and Garner, C.E., "A 5,000 Hour Xenon Hollow Cathode Life Test," AIAA Paper 91-2122, 27th Joint Propulsion Conference, Sacramento, California, June 24–26, 1991

8. Friedly, V.J., and Wilbur, P.J., "High Current Hollow Cathode Phenomena," Journal of Propulsion and Power, Vol. 8, No. 3, May–June, 1992, pp. 635–643

9. Plyutto, A.A., Ryzhkov, V.N., and Kapin, A.T., "High Speed Plasma Beams in Vacuum Arcs," Journal of Experimental and Theoretical Physics (JETP), Vol. 20, pp. 328–337, 1965

10. Williams, J.D., and Wilbur, P.J., "An Experimental Investigation of Hollow Cathode-Based Plasma Contactors," NASA CR-187120, May 1991

11. Latham, P.M., Pearce, A.J., and Bond, R.A., "Erosion Processes in the UK-25 Ion Thruster," IEPC Paper 91-096, 22nd International Electric Propulsion Conference, Viareggio, Italy, October 14−17, 1991

12. Kameyama, I., and Wilbur, P.J., "Characteristics of Ions Emitted from High-Current Hollow Cathodes," IEPC Paper 93-023, 23rd International Electric Propulsion Conference, Seattle, Washington, September 13−16, 1993

13. Kameyama, I., and Wilbur, P.J., "Zenith-Angle Distributions of Erosion Rates near High-Current Hollow Cathodes," AIAA Paper 96-3208, 32nd Joint Propulsion Conference and Exhibit, Lake Buena Vista, Florida, July 1−3, 1996

14. Ashley, S., "Electric rockets get a boost," Mechanical Engineering, Dec. 1995, pp. 61−65

15. Patterson, M.J., Rawlin, V.K., Sovey, J.S., Kussmaul, M.J., and Parkes, J., "2.3 kW Ion Thruster Wear Test," AIAA Paper 95-2516, 31st Joint Propulsion Conference and Exhibit, San Diego, California, July 10−12, 1995

16. Polk, J.E., Patterson, M.J., Brophy, J.R., Rawlin, V.K., Sovey, J.S., Myers, R.M., Blandino, J.J., Goodfellow, K.D., and Garner, C.E., "A 1000 Hour Wear Test of the NASA NSTAR Ion Thruster," AIAA Paper 96-2784, 32nd, Joint Propulsion Conference and Exhibit, Lake Buena Vista, Florida, July 1−3, 1996

17. Ecker, G., "Electrode Components of the Arc Discharge," Ergebnisse der Exakten Naturwissenschaften, Vol. 33, 1961, pp. 1−104

18. Friedly, V.J., "Hollow Cathode Operation at High Discharge Currents," NASA CR-185238, April, 1990

19. Sevier, K.D., "Instrumental Methods of Electron Spectrometry and Methods of Electron Detection," *Low Energy Electron Spectrometry*, Wiley-Interscience, John Wiley & Sons, 1972, pp. 18−32

20. Kameyama, I., and Wilbur, P.J., "Characteristics of Ions Emitted from High-Current Hollow Cathodes," NASA CR-195372, August, 1994

21. Rapp, D., and Francis, W.E., "Charge-Exchange between Gaseous Ions and Atoms," Journal of Chemical Physics, Vol. 37, No. 11, December 1962, pp. 2631−2645

22. Brophy, J.R., "Modified Bohm Velocity for Plasma Containing Primary Electrons and Doubly Charged Ions," appears in NASA CR-165253, "Ion and Advanced Electric Thruster Research," by Wilbur, P.J., December 1980

23. Stuart, R.V., and Wehner, G.K., "Sputtering Yields at Very Low Bombarding Ion Energies," Journal of Applied Physics, Vol. 33, No. 7, July 1962, pp. 2345−2352

24. Box, G.E.P., Cousins, W.R., Davies, O.L., Himsworth, F.R., Kenney, H., Milbourn, M., Spendley, W., and Stevens, W.L., "Analysis of Variance," *Statistical Methods in Research and Production*, 3rd edition, Hafner Publishing Company, 1961, pp. 96−149

25. Afifi, A.A., and Azen, S.P., "The Analysis of Variance," *Statistical Analysis, A Computer Oriented Approach*, Academic Press, 1972, pp. 143−226

# X. Appendix A: Zenith-Angle Distribution Measurements of Copper Erosion Rates near High-Current Hollow Cathodes

Although the measurement of ion-energy distributions associated with high-current hollow cathodes are essential to an understanding of the erosion they cause in practical ion-thruster applications, it is the erosion itself that is of primary interest. Further, energy distribution experiments are both time-consuming and expensive. Here, quick, straightforward erosion measurements are obtained using copper erosion targets. Similar tests conducted by Friedly and Wilbur using high-current xenon hollow cathodes were made with the targets placed on the cathode centerline only.[8] The tests reported here, on the other hand, used copper strips which extended from the cathode centerline to a direction parallel to the plane of orifice plate. Hence, erosion rates were obtained as a function of zenith angle measured from the cathode centerline toward a direction parallel to the plane of the orifice plate. The tests are also appealing because they involve exposure of the copper erosion strips to a hollow-cathode discharge for times (2−20 hours) that are significantly shorter than thruster lifetests (1,000−10,000 hours).

## 1. Apparatus and Procedures

The anode-cathode assembly used for the test and shown in Fig. A1 is identical to the one described in Chapter IV except it has a slightly different orifice.

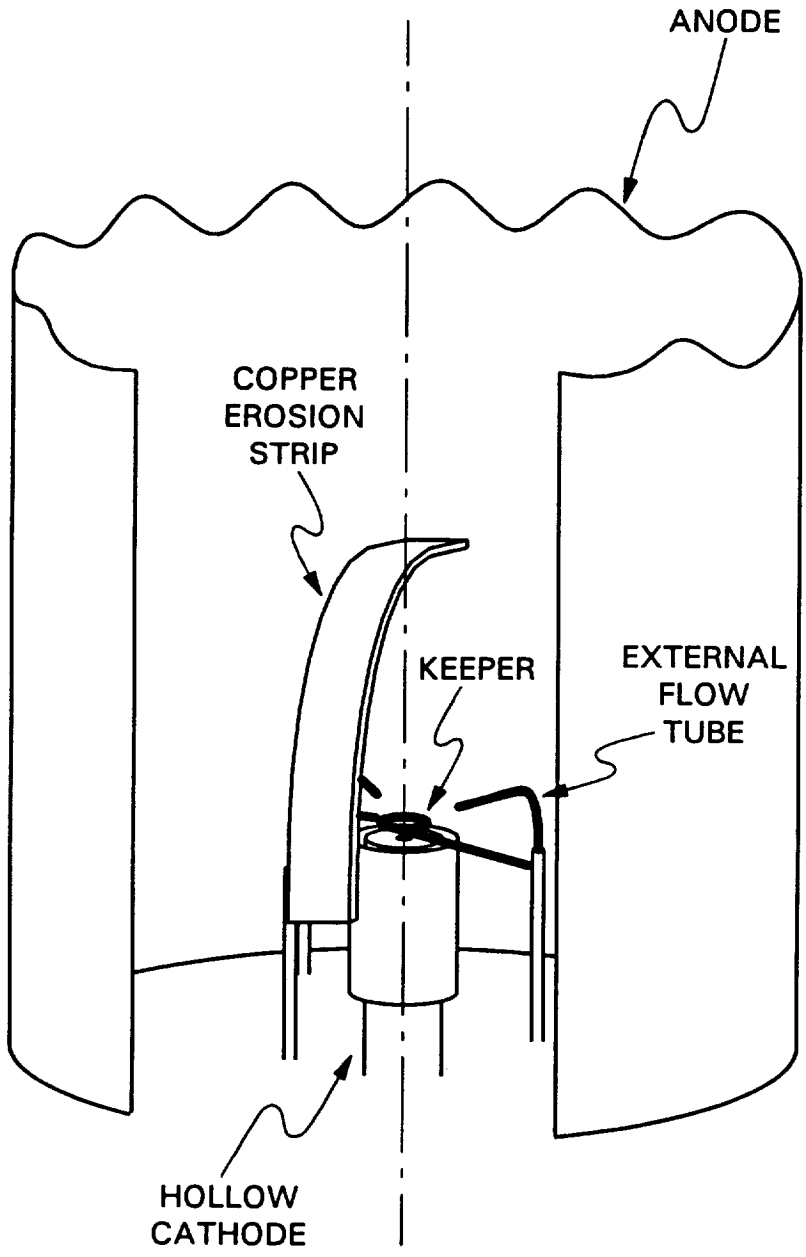


Fig. A1 Setup for Erosion Tests

The orifice bore, which was originally a 0.71-mm-diameter, right-circular cylinder, was chamfered as a result of operation at high current levels to yield an orifice with measured, upstream and downstream diameters of 0.71 mm ($^{+10\%}_{-0\%}$) and 1.65 mm ($^{+10\%}_{-0\%}$), respectively. Post-test measurements of orifice bore confirmed that enlargement was negligible during the tests. In some tests, the starter electrode was also used instead of a keeper after the manner described in Chapter IV.

Figure A1 also shows a copper erosion strip positioned on a semi-circular arc which is equi-distant (25 mm) from the orifice. Figure A2 is a detailed diagram in which zenith angle is defined and the strips, which were made of 5-mm-wide-by-50-mm-long copper plate, are shown. Each segment of the plate was polished to an average roughness (average magnitude of height/depth from the mean surface) of 0.05 $\mu$m or less. The notches shown in Fig. A2 were machined after the polishing to facilitate bending into the desired arc without distorting the individual flat segments in the strip significantly. Spray-on graphite was applied to all but a narrow band on the face of the strip which would be exposed to the discharge plasma. The graphite, which was removed using a solvent after the test, served to provide an erosion-free reference surface for post-test measurements of the erosion depths along the exposed band.

Figure A3 shows the neutral-density profiles measured on the cathode centerline at different external flow rates, $\dot{m}_{ext}$, by the movable, nude (glass-casing-removed), Shultz-Phelps ionization gauge that is described in Chapter IV. These measurements were made when there was no hollow-cathode discharge.

Erosion tests were initiated by first establishing a steady discharge between the

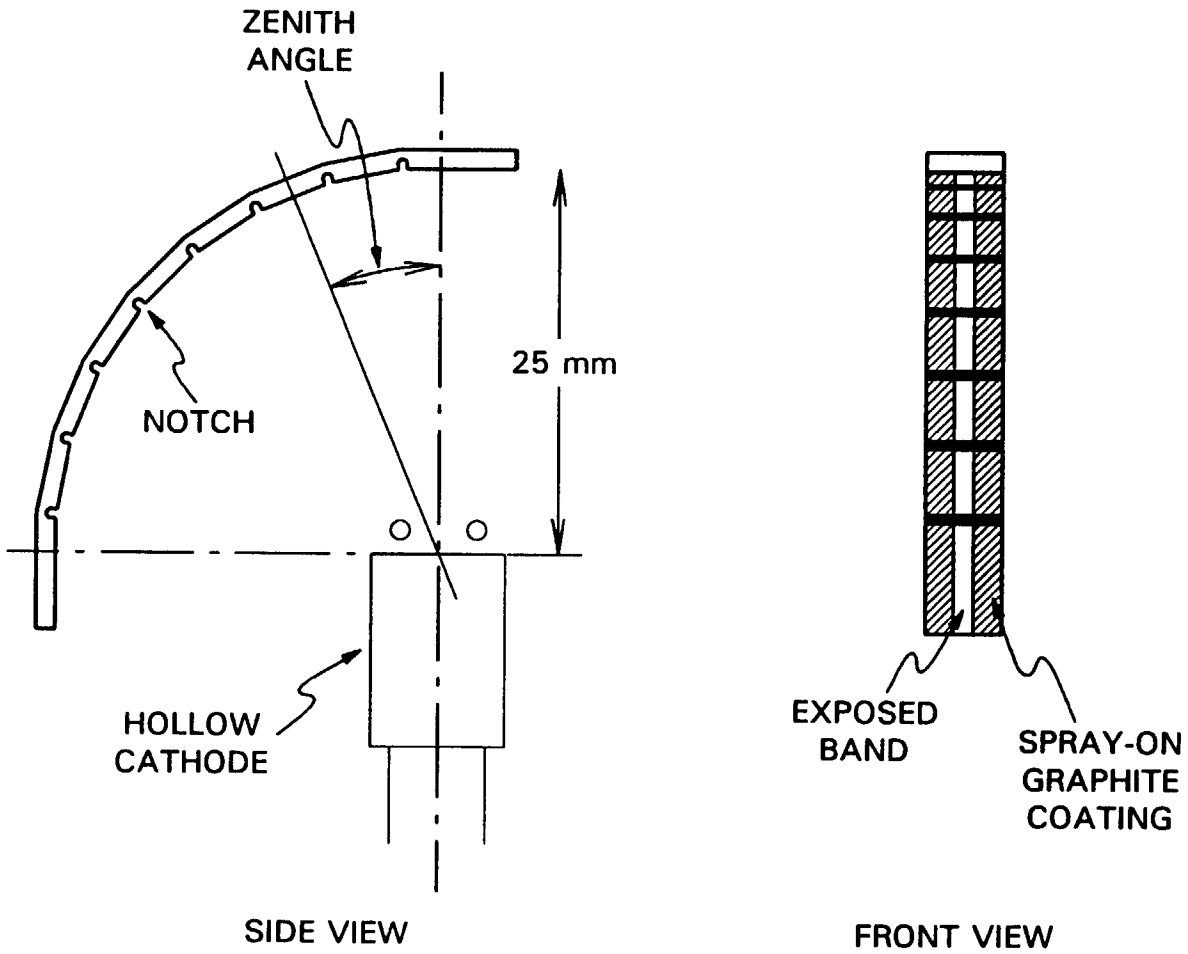


Fig. A2 Detailed Diagram of Copper Erosion Strips

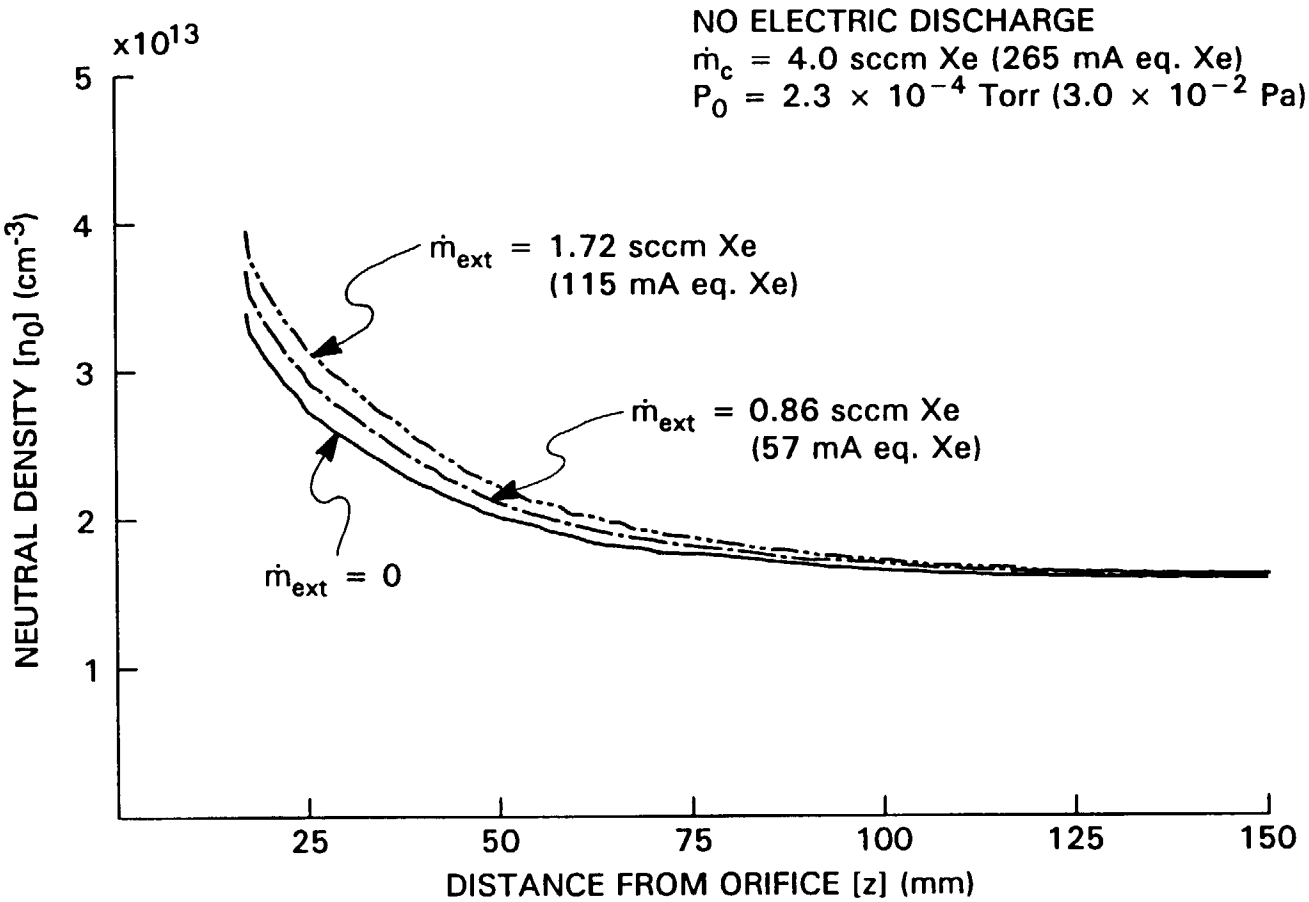


Fig. A3 Neutral-Density Profiles Measured on the Cathode Centerline at Different External Flow Rates

cathode and anode with the erosion strip positioned more than 150 mm downstream of the cathode. The procedure to start cathode discharge was exactly the same as that described in Chapter IV.

Once a discharge was established, the desired test conditions were set and the discharge was allowed to stabilize for 30 minutes before the actual erosion tests were initiated by positioning an erosion strip on an arc 25 mm from the orifice and holding it at cathode potential. During the test, discharge current, $J_{CD}$, and voltage, $V_{CD}$, keeper current, $J_K$, and voltage, $V_K$, ambient pressure, $P_0$, cathode flow rate, $\dot{m}_c$, and external flow rate, $\dot{m}_{ext}$, were recorded at 20-minute intervals and the strip surface was observed through the viewing slit in the anode to assure the graphite coating on the reference surface remained intact. Typically, tests were conducted for times that ranged from 2 to 10 hours of cathode operation depending on the expected erosion-rate magnitude; longer tests (up to 20 hours) were conducted in two separate segments (up to 10 hours each) with $\sim$ 10-hour intermission between the segments during which high vacuum was maintained.

After a test, the strip was retrieved and the graphite coating was removed using acetone to first wipe it and then clean it ultrasonically. Sputter-erosion profiles were next measured across sections of the strip at locations corresponding to different zenith angles using a surface profilometer. Figure A4 shows profiles across a strip obtained before (Figs. A4a and A4b) and after sputter erosion (Fig. A4c) at zero zenith angle. Before a test, the mean roughness $R_a$ of a reference surface like that shown in Figs. A4a (as recorded) and A4b (digitized and re-plotted for better appearance) was measured and found to be 0.01 $\mu$m. Figure A4c shows a profile

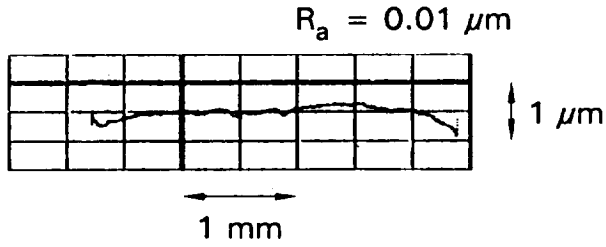


a. Pre-Test Profile

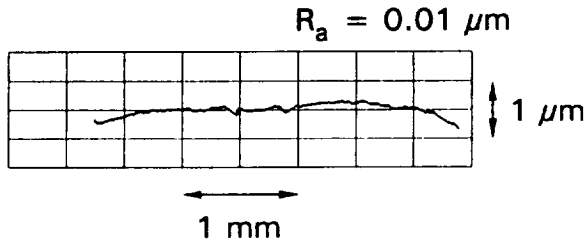


b. Pre-Test Profile (Digitized and Re-Plotted)

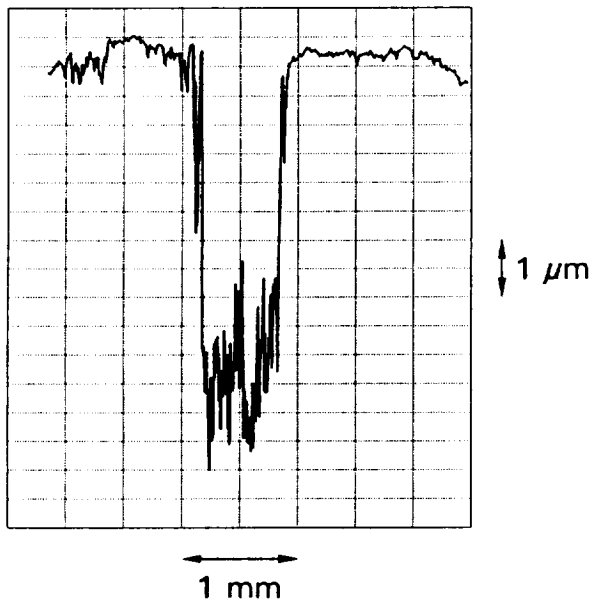


c. Post-Test Profile (Digitized and Re-Plotted)

Fig. A4 Typical Surface Profiles on an Erosion Strip at Zero Zenith Angle

across the same erosion strip after the test. The original profilometeric trace was digitized and re-plotted just as Fig. A4b was. The profile includes both the erosion trench, which is at the center of the figure, and the reference surface protected by the graphite coating, which is shown both to the left and right of the eroded region. The reference surface shown in the figure appears rougher than that in Figs. A4a and A4b. This occurred because a higher profilometer magnification was used to obtain the detail shown in Fig. A4c. This roughness in the reference surface is still, however, seen to be small compared to the mean depth of the erosion trench shown in Fig. A4c. Mean depths measured from trench edges were divided by test durations to obtain erosion rates; for the case of Fig. A4c, specifically, this yields a mean depth of 5.75 $\mu$m and a mean copper erosion rate of 0.383 $\mu$m/hour over the 15-hour test time.

The erosion rates obtained in these tests are subject to two major uncertainties; errors associated with erosion depth measurement and test repeatability factors that could be related to variations in conditions pertaining to sputtering and cathode operation. Initial surface roughness and/or curvature of pre-test profiles could preclude determination of the precise surface from which the erosion started. Except for very shallow trenches, however, pre-test surface roughness and curvature effects were made negligible compared to trench depth by adequate pre-test polishing and by exposing only a thin band of copper so that the trench would be narrow. The roughness at the bottom of the trench after a test, which can be seen in Fig. A4c, can, however, be more significant. For this specific case, the standard deviation of the trench depth, determined from a profile with a greater magnification, was

0.75 $\mu$m, which is $< 15\%$ of the mean erosion depth. Analysis of trenches with various depths showed that the roughness developed most prominently on the bottom of trenches having the highest erosion rates and inaccuracies in trench depth measurements were no more than $\pm 20\%$ for most trenches. It could be argued that the increased roughness in the bottom of the trenches may be a texturing effect caused by re-deposition of material sputtered from near the edges of trenches.

The other major uncertainty associated with test-to-test repeatability of erosion rates that could be affected by variations in experimental conditions and/or sputtering characteristics was determined by comparing results from several tests conducted under essentially identical conditions. Generally, two or three tests were conducted at each operating condition and error bars on erosion-rate-distribution profiles will be given to indicate the scatter in these results.

2. Experimental Results

Angular distributions of erosion rates measured at three discharge currents with and without a keeper are shown in Fig. A5. Also indicated in the figure are the cathode (orifice) flow rate, potential differences and pressure ranges measured during the tests. The ambient pressures shown are about the same as those expected in ion-thruster discharge chambers during typical lifetests but the discharge voltage shown is lower. The threshold energy for xenon-ion sputtering of the copper, target material used in this work, is 14 eV.[23] For all of the cases shown, the maximum erosion rates occurred at the centerline and the erosion rates dropped smoothly to immeasurable levels at the location on the plane of the orifice plate (90°). At the lowest discharge

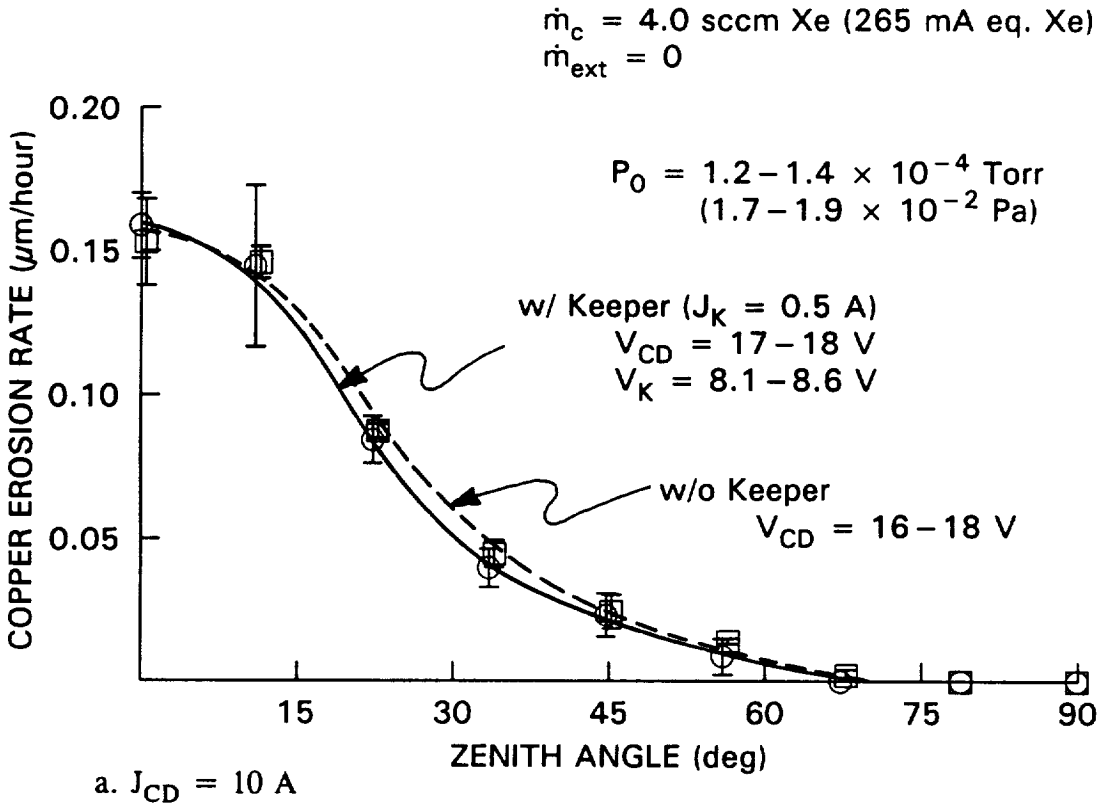


a. $J_{CD}$ = 10 A

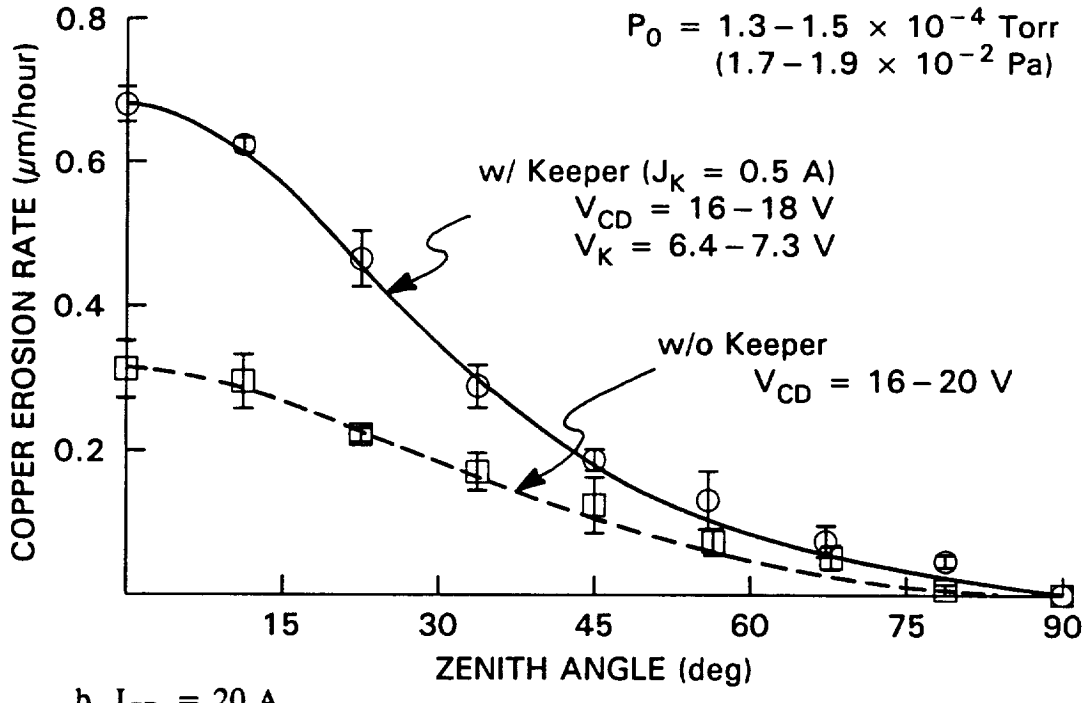


b. $J_{CD}$ = 20 A

Fig. A5 Zenith-Angle Distributions of Copper Erosion Rates 25 mm from Hollow-Cathode Orifice with Different Discharge Currents and Keeper Configurations

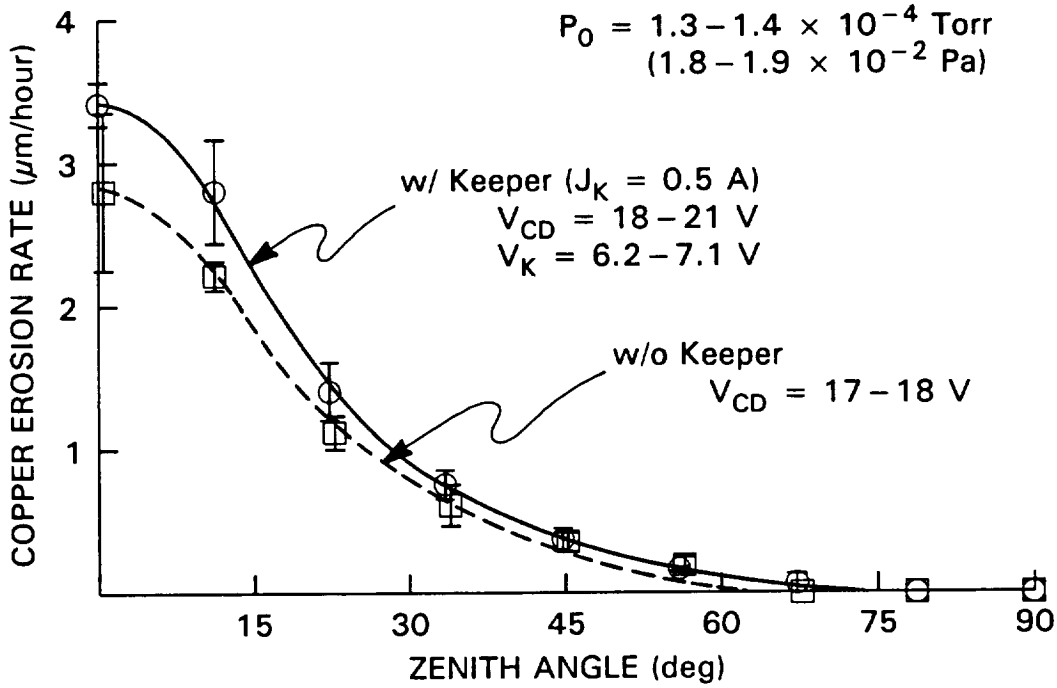


c. $J_{CD}$ = 30 A

Fig. A5 Zenith-Angle Distributions of Copper Erosion Rates 25 mm from Hollow-Cathode Orifice with Different Discharge Currents and Keeper Configurations (Continued)

current (10 A), the effect of a keeper is shown to be insignificant but it is obvious at the higher discharge currents that a keeper induces increased erosion rates, especially near the centerline. At the 30-A discharge current, it appears the distributions are slightly more peaked near the centerline than those measured at lower discharge currents.

The data in Fig. A5 that were obtained with the keeper in place are noteworthy because the erosion distributions contain no clear indication that the keeper intercepts high-energy ions that have been postulated to come on straight-line trajectories from a point source at the cathode orifice. Straight trajectories from the point source immediately adjacent to the cathode orifice would be expected to cause a depression in the erosion rates at angles between 60° and 80° for example in Fig. A5(b).

When external xenon-gas flows were introduced near the orifice, the erosion rates were reduced dramatically as the data of Fig. A6 show. For these tests, the ambient pressure was held higher than those measured for the discharge-current and keeper-configuration tests because the total flow of xenon into the facility was greater. This higher ambient pressure ($\sim 2.2 \times 10^{-4}$ Torr) yielded no-external-flow erosion rates that were $\sim 70\%$ of those obtained at the lower pressure ($\sim 1.4 \times 10^{-4}$ Torr). As the external flow rate was increased, Fig. A6 shows that erosion rates at all angles decreased until at a external flow rate of 1.72 sccm Xe (115 mA eq. Xe) the erosion rate reached the limit of what could be sensed in a 10-hour test.

Only single tests were conducted at each operating condition cited in Fig. A6 because the cathode tube failed mechanically before the tests could be repeated. If

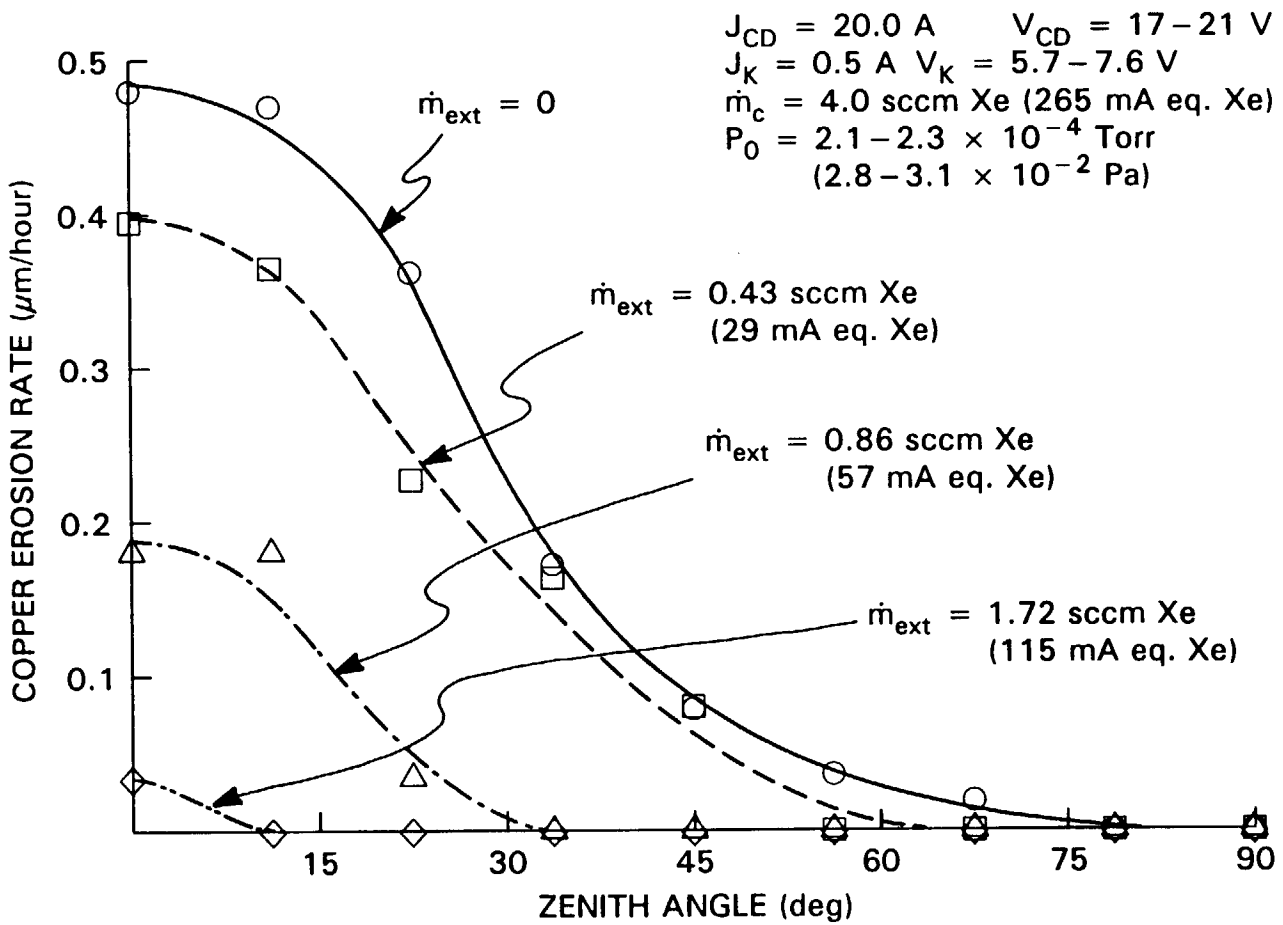


Fig. A6 Zenith-Angle Distributions of Copper Erosion Rates 25 mm from Hollow-Cathode Orifice at Different External Flow Rates

tests had been repeated, it is expected that errors would have been similar to those indicated by the error bars in Fig. A5 because external flow rate was controlled with a much greater accuracy than the cathode (orifice) flow rate.

3. Comparison with Ion-Energy-Distribution Measurements

The sputter-erosion technique used in these tests is simple and it indicates erosion damage directly. It does not, however, differentiate the effects of the ions and neutrals that can sputter a surface or yield information on the energy distributions of the ions and neutrals produced in high-current, hollow-cathode discharges. On the other hand, ion energy distributions have been measured on centerline previously using RPAs and an ESA and these data can be used to estimate sputter-erosion rates that would be expected on the cathode centerline due to the ions alone. The model that will be used in this analysis is identical to the one used in the development of the scattering model of Chapter III. It includes the assumption that the high-energy ions that come from hollow-cathode discharges expand in a spherical segment which has its center located at the cathode orifice. A second assumption used in the analysis is that high-energy ions pass through a downstream plasma, which is at a potential near anode potential, and then strike a cathode potential surface. If it is also assumed that all of the ions scattered in the collisions are lost then one obtains the following equation, identical to Eq. (2) in Chapter III:

$$\left.\frac{dJ_i}{d\varepsilon}(\varepsilon)\right|_{z=z_2} = \left.\frac{dJ_i}{d\varepsilon}(\varepsilon)\right|_{z=z_1} \frac{z_1^{\,2}}{z_2^{\,2}}\, exp\left[-\sigma(\varepsilon - V_a)\int_{z_1}^{z_2} n_0(z)\,dz\right]. \qquad \text{(A1)}$$

This last assumption introduces an error because sputtering due to the flux of low-

energy ions is neglected in the analysis. Sputtering yields associated with small ion energies (corresponding to anode-to-cathode potential difference or slightly higher) are, however, sufficiently small that erosion rates obtained using only primary-ion current densities should still be good estimates. An exception to this would involve a target biased so negative that low-energy ions could acquire sufficiently high kinetic energies to induce significant erosion.

The model, which is described in Chapter III and here, does not reflect the effects of high-energy neutrals created by charge-exchange collisions between high-energy ions and ambient low-energy neutral atoms. In fact, the production of high-energy neutrals, which was neglected in the scattering model, could contribute in two different ways to the ion-energy distribution measurements and erosion rate tests: 1) high-energy neutrals could regenerate high-energy ions as a result of successive charge-exchange collisions with low-energy ions in the ambient plasma and 2) high-energy neutrals could themselves cause erosion. If one assumes that the plasma ion density is small compared to the neutral density, the increase in high-energy ions that could result from charge-exchange collisions between ambient-plasma ions and fast neutrals can be neglected. The second effect, sputtering by high-energy neutrals, may also be neglected compared to that by ions because the neutrals are not accelerated from ambient plasma potential to the cathode potential through the sheath at a target surface.

Once ion-current-density distributions are determined at the location of the erosion strips, the erosion rate, $\dot{h}_t$, on a surface at a potential, $V_t$, (zero in this specific case) is computed using the atomic mass, $m_t$, density, $\rho_t$, and sputtering

yield, $\eta_t$, of the target material. The expression used for this purpose is

$$\dot{h}_t = \frac{m_t}{e\rho_t}\int_{V_t}^{\infty} \frac{dj_i}{d\varepsilon}(\varepsilon)\,\eta_t(\varepsilon - V_t)\,d\varepsilon \ . \qquad \text{(A2)}$$

Incorporation of the collisional losses just mentioned into the erosion rate model requires a knowledge of the neutral xenon-atom density downstream of the cathode. Since this neutral density profile depends on geometrical factors, only the ion-energy distributions for known geometries (i.e. the ESA data of this work and the RPA data of Ref. 8) have been used to compute copper erosion rates. These data sets both pertain to erosion at 25 mm downstream of a hollow cathode operating with a keeper at a 20-A discharge current and a cathode flow rate of $\sim$4 sccm Xe ($\sim$265$-$280 mA eq. Xe). The analysis involved computation of ion-current energy distributions at the source using measured ion-current energy distributions, a neutral density profile, and an ambient plasma potential in Eq. (A1). Using these energy distributions at the source as input data, the ion-current energy distribution was next determined at the location where the estimate of erosion rate was sought using the neutral density profile and potential data associated with erosion tests. This neutral density profile was determined by fitting exponential, cathode-flow-dependent and constant, ambient components to appropriate neutral-density-profile data (Fig. A3). Ambient plasma potentials were assumed to be equal to corresponding anode potentials.

When the ion-current energy distributions obtained from ESA measurements at a low ambient pressure (solid curve in Fig. 16a) were used in Eq. (A1), ion current densities at ion-source locations of z = $\sim$0 and 5 mm yielded erosion rates of

0.00075 and 0.00016 $\mu$m/hour, respectively. The neutral density profile data from the solid curve in Fig. 13a and an ambient plasma potential of 16V were used in these calculations. The computed erosion rate values are a few orders of magnitude less than the measured erosion rate of 0.68 $\mu$m/hour given in Fig. A5b. On the other hand, using the RPA data corresponding to an ambient pressure of $3.0 \times 10^{-3}$ Torr (0.40 Pa) from Ref. 8, yields erosion rates of 1.7 $\mu$m/hour and 2.0 $\mu$m/hour at discharge voltages of 12 V and 14 V, respectively, assuming the source was at $z = \sim 0$ mm. These results agree with the measured erosion rate within about an order of magnitude. The computed rates decreased to 0.051 and 0.056 $\mu$m/hour at discharge voltages of 12 V and 14 V, respectively, when the source location was moved to $z =$ 5 mm. All computed erosion rates are tabulated in Table A1 along with assumed source locations and ambient plasma potentials.

The reason the RPA data yield erosion rate results that are closer to measured values than those associated with the ESA data is considered to be related to the much greater acceptance angle of the RPA. This large ion acceptance angle should enable the RPA to sense high-energy-ion current densities that are much closer to those actually seen by the copper erosion strip. The collimator set and the relatively long transmission region of the ESA, on the other hand, assure that only a small fraction of the ions that pass through the entrance aperture reach the detector.[20] It is also likely that neutral atoms in the transmission region of the ESA scatter ions and reduce the signal even further.

Table A1 Copper Erosion Rates Computed from Ion-Current-Density Energy-Distribution Measurements

| | Ambient Plasma (Anode) Potential* | Erosion Rate Computed with the Ion Source Assumed at z = ~0 mm | Erosion Rate Computed with the Ion Source Assumed at z = 5 mm |
|---|---|---|---|
| RPA Measurements | 12 V | 1.7 μm/hour | 0.051 μm/hour |
| | 14 V | 2.0 μm/hour | 0.056 μm/hour |
| ESA Measurements | 16 V | 0.00075 μm/hour | 0.00016 μm/hour |

* These plasma/anode potentials measured during the RPA and ESA experiments were used to determine ion fluxes at the source. The anode potential measured during the erosion-rate tests (16 V) was used to determine the kinetic energies of ions on the targets.

## XI. Appendix B: Analyses of Errors in Experimental Measurements

1. Neutral Density Measurements

Each neutral density profile shown in Figs. 12 and 13 is a mean profile obtained by plotting mean values of density at each axial location from data measured at essentially identical conditions. Since there was data scatter in the measurements, the profiles contain associated errors and it could be argued that separation of profiles at different conditions is uncertain to some extent. A difficulty associated with analysis arises since the measurements are made continuously as functions of position and errors in measured values can not be characterized by normal distributions. For simplicity, however, a standard deviation was computed for each profile at 0.5 mm intervals and compared with the associated differences between mean values. It was found that the error ranges would be of the order of the line thicknesses if they were drawn in the figures and that the differences of mean values evaluated for any two profiles were at least twice as great as the combined standard deviations associated with the mean values. Another approach called the F-test[24,25] was also applied. In this case, F-ratios associated with different ambient pressures and external flows were computed at 0.5 mm intervals and then averaged over the ranges of axial position. The analysis showed that the data measured through variation of these parameters were meaningfully separated with more than 99.9% confidence with and without a

keeper. It should be noted that results obtained from F-tests are still approximately correct even for data not characterized by normal distributions as long as the numbers of data sets used to compute variances are not too different. In this specific case, this condition was met.

2. Ion-Current-Energy-Distribution Measurements

When the ion-current energy distributions were measured using the ESA at essentially identical conditions and compared with each other, the measurements were found to involve two dominant errors: errors observed in the same day of experiments and day-to-day errors. When experimental data collection was repeated on the same day of testing, the ion-current distribution data were found to agree within 20−30%. However, after a few hours of ESA usage, distribution profiles measured by sweeping the energy in opposite directions would begin to change. Typically, these changes due to sweep direction were accompanied by a spot of discoloration on the graphite-coated, ESA outer surface around the point where the axis of the entrance collimator intersected it. The reason for the changes in the measured profiles is not understood but it is considered likely that it occurred when the ESA outer surface became contaminated with material from the hollow cathode insert. It is postulated that local charging disturbed a prescribed electric field inside the ESA when this contamination reached a certain level. In order to assure that results obtained were not subject to this anomaly, 1) at least two profiles were collected each day at each cathode operating condition and 2) the ESA was cleaned after each test series and a new graphite-coating was applied on all surfaces that could be exposed to ions and

electrons.

Measurements made on different days exhibited greater scatter than the 20 to 30% observed on a given day. It was postulated that graphite coatings applied to the ESA surfaces could have had different thicknesses on different days and that this affected day-to-day reproducibility. The principal focus of this work is on the effects of ambient pressure and external flow rate on changes in energy distribution. These changes were consistent from day to day even though absolute magnitudes of ESA signals were different. ESA measurements obtained on a given day (two at each condition) were, therefore, first normalized using a mean energy-distribution reference profile. The measurement and normalization processes were repeated on three different days and the resulting six normalized distributions at essentially identical, cathode operating conditions were averaged to yield mean profiles of the normalized distributions which are shown in Figs. 17 and 19.

Errors associated with the averaging process just discussed in the previous paragraph were quantified conducting F-tests on skewness, which is defined as the third-order moment around the average energy of a distribution profile. When the analysis was performed on the distributions, it was found that the confidence that the data are separated meaningfully at each ambient pressure is $>99.9\%$ and that at each external flow rate is $>99.5\%$.